Single molecule studies in a temperature-jump optical trap

Sara de Lorenzo Ros

ADVERTIMENT. La consulta d'aquesta tesi queda condicionada a l'acceptació de les següents condicions d'ús: La difusió d'aquesta tesi per mitjà del servei TDX (**www.tdx.cat**) i a través del Dipòsit Digital de la UB (**diposit.ub.edu**) ha estat autoritzada pels titulars dels drets de propietat intel·lectual únicament per a usos privats emmarcats en activitats d'investigació i docència. No s'autoritza la seva reproducció amb finalitats de lucre ni la seva difusió i posada a disposició des d'un lloc aliè al servei TDX ni al Dipòsit Digital de la UB. No s'autoritza la presentació del seu contingut en una finestra o marc aliè a TDX o al Dipòsit Digital de la UB (framing). Aquesta reserva de drets afecta tant al resum de presentació de la tesi com als seus continguts. En la utilització o cita de parts de la tesi és obligat indicar el nom de la persona autora.

ADVERTENCIA. La consulta de esta tesis queda condicionada a la aceptación de las siguientes condiciones de uso: La difusión de esta tesis por medio del servicio TDR (**www.tdx.cat**) y a través del Repositorio Digital de la UB (**diposit.ub.edu**) ha sido autorizada por los titulares de los derechos de propiedad intelectual únicamente para usos privados enmarcados en actividades de investigación y docencia. No se autoriza su reproducción con finalidades de lucro ni su difusión y puesta a disposición desde un sitio ajeno al servicio TDR o al Repositorio Digital de la UB. No se autoriza la presentación de su contenido en una ventana o marco ajeno a TDR o al Repositorio Digital de la UB (framing). Esta reserva de derechos afecta tanto al resumen de presentación de la tesis como a sus contenidos. En la utilización o cita de partes de la tesis es obligado indicar el nombre de la persona autora.

WARNING. On having consulted this thesis you're accepting the following use conditions: Spreading this thesis by the TDX (**www.tdx.cat**) service and by the UB Digital Repository (**diposit.ub.edu**) has been authorized by the titular of the intellectual property rights only for private uses placed in investigation and teaching activities. Reproduction with lucrative aims is not authorized nor its spreading and availability from a site foreign to the TDX service or to the UB Digital Repository. Introducing its content in a window or frame foreign to the TDX service or to the UB Digital Repository is not authorized (framing). Those rights affect to the presentation summary of the thesis as well as to its contents. In the using or citation of parts of the thesis it's obliged to indicate the name of the author.

UNIVERSITAT DE BARCELONA

FACULTAT DE FISICA

Departament de Fisica Fonamental

Programa de Doctorat de Fisica de la Materia Condensada

Tesis Doctoral - PhD Thesis

SINGLE MOLECULE STUDIES IN A TEMPERATURE-JUMP OPTICAL TRAP

Sara de Lorenzo Ros

Memoria presentada para optar al título de Doctor en Física bajo
la supervisión del Dr.Félix Ritort

Agradecimientos

El día 24 de Septiembre del año 2005 llegué a Barcelona, se celebraba la fiesta de la Mercé y coincidía con mi primera aventura fuera de casa y fuera de mi ciudad. Los primeros meses fueron difíciles pero enseguida comencé a formar y a crear mi nueva vida en Barcelona. Ese viaje me cambió la vida, pero sobre todo me cambió la forma de vivirla. En mis primeros años en la Universidad de Barcelona, comencé como técnico de laboratorio. Mi ”jefe”, en aquel momento y posterior director de Tesis, Dr. Félix Ritort, me eligió para comenzar a montar su laboratorio, en concreto dos laboratorios, uno donde sintetizarámos ADN y otro donde colocaríamos un instrumento de pinzas ópticas. Yo, recién licenciada en Física, no había tocado una pipeta y menos una pinza óptica. Gracias Félix por estos años, gracias por tu confianza en mí, personal y profesional, y el esfuerzo que has dedicado en mi formación durante todo este tiempo. Gracias por haberme dado la oportunidad de haber conocido tanta gente estupenda y haber vivido tan maravillosas experiencias por todo el mundo. Gracias por transmitirnos tu amor por la ciencia de números, de ecuaciones y de notas musicales.

Comencé a dar mis primeros pasos dentro del grupo, Maria Mañosas terminando la escritura de su tesis, siempre trabajando, con su té cerquita y siempre con un ratito para darte buenos consejos Un placer haberte conocido Maria! Josep Maria Huguet comenzaba sus primeros pasos en la tesis doctoral. Una excelente persona y compañero, siempre dispuesto a ayudarte, escucharte y formarte. Con Josep Maria aprendí a conocer el instrumento de pinzas ópticas desde su interior y a arreglar nuestros propios desaguisados. Gracias por tu paciencia, tu sabiduría y tu amistad! Y Núria Forns, mi primera gran amiga catalana. Con ella comencé a descubrir tanto la maravilla de poder creer que hay ADN en una minúscula gota dentro de un tubo de ensayo como descubrir las tierras catalanas, desde lo más alto, casi rozando el cielo. Más tarde, llegaron al laboratorio Carol Larroy, una doctora en bioquímica, dulce, trabajadora y amante del deporte, con la que tuve el placer de disfrutar de un congreso en Menorca, que al finalizar se convirtieron en unas vacaciones llenas de preciosas playas y de música de habaneras. A continuación llegó al laboratorio Joan Camuñas, recién licenciado en Física y sin embargo con una enorme y profunda curiosidad por toda lo ”bio” y con un gran futuro por delante. Gracias Joan por tus bromas futboleras, tus preguntas sin respuesta fácil, tu cariño y amistad durante todos estos años. Nunca olvidaré tus charlas y discusiones con Cristiano, que grandes! Recuerdo perfectamente cuando Anna Alemany llegó al laboratorio una tarde, una persona llena de energía y de alegría, cosa que después pude comprobar durante los 5 años que hemos compartido despacho, aventuras, historias y experiencias. Conservo grandes recuerdos de todas aquellas aventuras. Por aquel entonces llegaba al laboratorio Marco Ribezzi, el chico italiano que llegó para realizar una estancia dentro de su tesis doctoral y que como en mi caso, Barcelona le enganchó. Gracias Marco por tu constante apoyo y ayuda en estos análisis de datos tediosos. Gracias por tu saber hacer científico, crítico y objetivo. Todo un placer haberte conocido y todo un lujo por haber compartido contigo mi primer artículo científico. Durante estos años tuve la gran suerte de conocer a Kumiko Hayashi, una persona encantadora, llena de alegría y de buenos sentimientos. Gracias Kumiko por tus divertidísimas historias y por todo lo que nos has transmitido y enseñado de una cultura como la tuya. No recuerdo exactamente cuando apareció Cristiano Valim Bizarro, el postdoc brasileño que revolucionó la forma de trabajar del laboratorio con su constancia, interés, trabajo y sobre todo buen corazón que plasma en todo lo que hace y dice. Tengo la suerte de haber conocido a un gran científico pero sobre todo a una gran persona. Hablando de lo cual, no puedo dejar de dedicarle unas palabras a una de las personas con más personalidad y amor por el arte que he conocido, Alessandro Mossa. Un físico teórico con magnificas dotes para la escritura y el teatro, que convierte en elegante cualquier problema teórico. Siempre quedará en nuestra memoria el tornillo Di'Lorenzo! Por estos días, Blanca Rey llegaba al laboratorio después de haber realizado su máster en biofísica. Gracias Blanca por todo lo que has aportado al laboratorio, tu presencia, tu constante colaboración y ayuda ha formado parte en los éxitos de este laboratorio. Y como no mencionar a Maria Martí. Una chica guapa por dentro y por fuera que tras terminar el máster de biofísica, trajo al laboratorio un montón de ilusión y personalidad. Sus ganas por aprender de todo, su organización y su manera de transmitir sus conocimientos de una forma sencilla, nos permitió conocer su valía y sus grandes cualidades para trabajar en equipo. Y por aquellos días y recién llegada de su estancia postdoctoral americana, llegaba al laboratorio Silvia Frutos. Su inteligencia, intelectual y emocional, hizo mella en todos y cada uno de las personas que tenemos el placer de conocerla. Gracias Silvia por esos maravillosos cafés, por tu simpatía, sinceridad, por tus valores y valentía que nos has transmitido en todos estos años. Durante la realización del máster en biofísica, conocí a Marta Dies. Una amiga "de las buenas" con la que he compartido muchos secretos, experiencias, sesiones de Skype y batidos de té verde. Te echo de menos!

Cuando comencé mi andadura en la construcción de mi primer equipo de minipinzas, la parte de electrónica me llevó a conocer a Miguel Angel y a Puy (mis compis del Hospital Clínic). Durante ese mes de Febrero tuve la suerte de aprender de ellos un montón de conocimientos, experiencias técnicas y entrenamiento para lo que vendría después. Gracias por todos aquellos inolvidables momentos que compartimos! Gracias a Olga, Bea, Elena, Mercedes y Cristina, las estupendas secretarias del departamento de Fisica Fonamental. Gracias por vuestras sonrisas mañaneras, vuestra constante ayuda y siempre productivo trabajo. Os echaré de menos! En esta sección de agradecimientos no puedo olvidarme del personal del taller mecánico de la Universitat de Barcelona, Sunyol, Javi y Manel, quienes hicieron toda la parte mecánica del instrumento de las minipinzas. He tenido mucha suerte en coincidir con personas de una calidad humana como la vuestra. Hacéis un trabajo excelente y muy constructivo. Gracias por todo!

Al terminar la construcción del equipo, en Julio del 2009, Félix me sugirió el hacer una estancia para profundizar en el alineamiento óptico del instrumento. El sueño de cualquier joven, California, y de cualquier estudiante de doctorado, University of Berkeley. During this stay and during my stay in Los Lunas (New Mexico), I had the opportunity to work with the inventor of the minitweezers instrument , Dr.Steven.B.Smith. During these times I learned how to do science and more importantly for me, how to enjoy science. I learned an easy way to think and to think for myself. Thanks to Steven for his patience, wisdom, and simple and elegant way to make real science. I would like to say thank you to Christian Wilson. He is a young scientist whose love of science made him cross the Andes. Thank you Christian for your conversation and friendship during my stay in Berkeley.

Gracias a mis compis de piso Susi, Esther, Gorka y David, los mejores del mundo mundial. Gracias por tantas noches compartidas entre debates futboleros, series policiacas, cenas a deshoras y aventuras en caballo o tirolina. Gracias por esta maravillosa experiencia que siempre recordaré, gracias por vuestra amistad y cariño. Gracias a mis amigos los teclones, las Elena's, Marcos, Pilar, Armando, Eva, Harold, Ana, Nuria, Bea, Teresa y Emma. Cada uno de vosotros habéis sido una alegría en diferentes momentos de mis años en Barcelona. Gracias por Comercio Justo, las cenas hasta las tantas, las cervecitas con limón y los viajes juntos. Experiencias y personas inolvidables que siempre guardaré en mi corazón.

Ya de vuelta a mi "Madrid", quiero agradecer a IMDEA Nanociencia quien me ha dado la oportunidad de seguir creciendo profesionalmente. Me gustaría agradecer al Dr. Ricardo Arias-Gonzalez y Dr. Borja Ibarra la confianza puesta en mí para emprender este nuevo proyecto juntos. A Irene, Rebeca, Fernando, Jose, Elisa y Fran por vuestra cariñosa y amable acogida en IMDEA. Gracias a todos por vuestra profesionalidad, vuestra paciencia y vuestro sentido del humor. Gracias a Ana, mi nueva compañera de despacho, por los buenos momentos que he pasado durante la escritura de esta tesis y porque siempre consigue sacarme una sonrisa. Gracias por tu constante apoyo y por aguantarme!

Gracias a mis siempre amigos Paloma, Oscar, Angel y Dani. Vuestra amistad durante estos años siempre ha sido crucial para mi y de los que siempre he recibido palabras de aliento. Gracias por la fidelidad y por la amistad que habéis demostrado. Ahora más cerquita y mejor!

Y, por supuesto, el agradecimiento más profundo y sentido va para mi familia. Sin su apoyo, colaboración e inspiración habría sido imposible realizar esta tesis doctoral. A mis padres, Maria y Jaime, por ser mi ejemplo diario de lucha y trabajo. Gracias por todos los valores que me habéis transmitido ahora y siempre. Por vuestro cariño y confianza que me demostráis en cada gesto. Lo que soy, es gracias a vosotros. A mi hermana Ruti, gracias por tu honestidad y tu gran corazón, nunca cambies y nunca dejas de enseñarnos como usarlo. A mi hermano Jaime, gracias por ser un ejemplo de valentía, inteligencia y fuerza de voluntad, pero sobre todo por enseñarme como ser una excelente persona. Tú puedes con todo Diu! A mi cuñado Miguel, por su tenacidad y gran capacidad de superación, gracias por todos estos años de experiencias y viajes estupendos. Todo un placer cuñao! A mi cuñi Ines por ser una compañera de baile excepcional! Gracias por tu amistad y por tu complicidad todo este tiempo! A mis sobrinitas, Dani y Adriana, gracias por vuestras sonrisas y aventuras, sois la alegría de la casa. A mis yayos y al Padre Ocaña, gracias por cuidarme siempre. To my family in USA Steve, Sandy and Ryan, thank you very much for taking care of me as a daughter and as a syster. Thank you for your support, caring and personal values that you teach me every day. Thank you for the unforgettable barbacues and our wonderful time together. A ti, Warren, gracias por estar siempre a mi lado, dándome fortaleza y seguridad. Thank you to be the reason of my present and my future! Thank you, por todo lo vivido y lo que nos queda por vivir! Go team Smith-Lorenzo!

Contents

Abstract

In the field of biophysics, the study of the thermodynamic characteristics of biomolecules, such as DNA, RNA or proteins, allows us to understand more about the building blocks of life. The thermodynamic characterization of the biomolecule gives us clues as to their functions and capabilities inside every living organism.

The thermodynamic characterization of nucleic acids describes how temperature affects the stability and the structure of double stranded DNA. The melting temperature of DNA (T_M) is defined as the temperature at which half of the DNA strands in a bulk solution experiment are in the double stranded DNA (dsDNA) or random coil configuration and half of the DNA are in the single-stranded DNA (ssDNA) configuration. Using (T_M), it has been possible to experimentally determine the thermodynamic parameters of ΔG, ΔH and ΔS. Viceversa, when the thermodynamic parameters of a given nucleic acid sequence are known, the (T_M) can be predicted. This effect has important applications for biomolecule techniques such as PCR (*Polymerase chain reaction*) or sequencing.

Traditionally thermodynamic properties of DNA have been determined using bulk techniques such as calorimetry or UV absorbance. In both cases the melting temperature has been determined by changing the temperature or pH of the entire sample.

Over the past two decades single molecule force spectroscopy has been established as a powerful, accurate and bulk-complementary method of characterizing the thermodynamics of nucleic acids. Optical trapping is an experimental technique which allows force to be exerted on a micrometric particle by using the radiation pressure of light. The miniTweezers (mT) is the newest generation of optical tweezers instruments. This instrument can be used to exert and measure forces in a range between 1-200 pN and has unprecedented resolution (0.1 pN in force an around 1 nm in distance) with very high thermal and noise stability. Optical trapping is very useful in the field of molecular biology because it allows forces to be exerted on single biomolecules bonded to the micrometric particle.

This technique is used to carry out pulling experiments on single molecules allowing us to study the mechanical, thermodynamic and kinetic properties of the molecule. Mechanical melting or unzipping is a process that consists of pulling apart the two strands of the dsDNA until the base pairs are disrupted and the molecule converts into ssDNA. In this case, and in contrast to other techniques, force, rather than temperature or pH, is used to open the molecule.

Past experiments have shown that better resolution can be obtained using single molecule techniques than can be obtained using bulk experiments. Although force unzipping provides a direct estimation of ΔG at room temperature, extracting the value of T_M always requires the determination of the ΔH and ΔS contributions and until now has not been reliable accomplished.

To carry out a full thermodynamic characterization of nucleic acids is important to know both magnitudes (Force and Temperature). The best way to accomplished this is to perform pulling experiments on a single DNA molecule at different temperatures.

To this end we have developed a novel temperature-jump optical tweezers setup that changes the temperature locally and rapidly. It uses a heating laser with a wavelength that is highly absorbed by water so it can cover a broad range of temperatures. This instrument can record several force/distance curves for one individual molecule at various temperatures with good thermal and mechanical stability. Our design has features to reduce convection and baseline shifts which have troubled previous heating-laser instruments. The instrument was used to carry out DNA unzipping experiments where we derived the average basepair ΔG, ΔS and ΔH of formation of dsDNA in a range of temperatures between 5°C and 50°C .

Resumen

En el campo de la biofísica, el estudio de las características termodinámicas de las biomoleculas, como ADN, ARN o proteínas, permite conocer más sobre los componentes básicos de la vida. La caracterización termodinámica de las biomoleculas nos proporciona pistas sobre sus funciones y capacidades dentro de un organismo vivo.

La caracterización termodinámica de los ácidos nucleicos describe como la temperatura afecta la estabilidad y la estructura de la doble cadena de ADN. La temperatura de melting del ADN (T_M) se define como la temperatura a la cual la mitad de las moléculas de ADN disueltas en una solución se encuentran en configuración de doble cadena (dsDNA) y la otra mitad se encuentra en la configuración de cadena individual (ssDNA). Conociendo el valor de la (T_M) es posible determinar experimentalmente los parámetros termodinámicos : ΔG, ΔH y ΔS. Viceversa, cuando los parámetros termodinámicos de la secuencia de un ácido nucleico es conocido, la (T_M) puede ser predecida. Este efecto tiene importantes aplicaciones en técnicas de biología molecular como PCR (en inglés *Polymerase chain reaction*) o secuenciación.

Tradicionalmente las propiedades termodinámicas del ADN han sido medidas utilizando técnicas de volumen como calorimetría o absorbancia de UV. En ambos casos la temperatura de melting ha sido calculada modificando la temperatura o el pH de toda la muestra.

En las pasadas dos decadas, las técnicas de espectroscopía de fuerzas sobre moléculas individuales, han sido reconocidas como técnicas de un gran valor y precisión cuyos resultados en el estudio de la caracterización termodinámica pueden ser considerados perfectamente complementarios a los medidos en técnicas de volumen. La técnica de atrapamiento óptico es una técnica experimental la cual permite ejercer fuerza sobre una partícula micrométrica utilizando la presión de radiación de la luz. Las minipinzas (en inglés minitweezers) es una nueva generación a los instrumentos de pinzas ópticas. Este instrumento puede ser usado para ejercer y medir fuerzas en un rango de entre 1-200pN y con una resolución en fuerza y distancia sin precedentes. El atrapamiento óptico es muy útil en el campo de la biología molecular permitiendo ejercer fuerzas sobre biomoléculas individuales enganchadas.

Esta técnica es usada para llevar acabo experimentos de estiramiento sobre moléculas individuales permitiendo el estudio de las propiedades mecánicas, termodinámicas y cinéticas de la molécula bajo estudio. El experimento de unzipping o melting mecánico es un proceso que consiste en separar las dos hebras de la dsDNA hasta que los enlaces entre los pares de bases complementarios son deshechos y la molécula se convierte en ssDNA. En este caso la fuerza es usada como medio para abrir la molécula, en vez de la temperatura o el pH como en otras técnicas.

Pasados experimentos han mostrado que podemos obtener mejor resolución utilizando técnicas de moléculas individuales que utilizando técnicas en volumen. Aunque la fuerza de unzipping nos proporciona una estimación directa de ΔG a temperatura ambiente, para poder extraer el valor de T_M requiere conocer las contribuciones de ΔH y ΔS y hasta ahora no ha sido posible.

Para llevar acabo una completa caracterización termodinámica de ácidos nucleicos es importante conocer ambas magnitudes (Fuerza y Temperatura). El mejor camino para hacer este análisis es llevar acabo experimentos de unzipping sobre moláculas individuales de ADN a diferentes temperaturas.

Por ello hemos desarrollado un novedoso instrumento de pinzas ópticas con un controlador de temperatura que nos permite modificar y cambiar la temperatura de manera local y rápida. Se ha usado un específico láser calentador con una longitud de onda con una alta absorción en agua que permite cubrir un amplio rango de temperaturas. Este instrumento nos permite grabar diversas curvas de fuerza/extensión para una molécula individual a varias temperaturas con una buena estabilidad térmica y mecánica. Este diseño tiene ciertas mejoras para reducir la convección, el cual ha sido un grave problema en previous equipos calentados através de un láser. Este equipo ha sido usado para hacer experimentos de ADN, lo que nos ha permitido hacer un análisis promediado de ΔG, ΔS y ΔH entre pares de bases en un rango de temperatura entre 5°C y 50°C.

List of Abbreviations

- A: Adenine
- AD: Antidigoxigenin
- ADC: Analogical Digital Converter
- B: Bandwidth
- bp: Base-pair
- C: Citosin
- DAC: Digital Analogical Converter
- DAQ: Data Acquisition Board
- DNA: Deoxyribonucleic acid
- dsDNA: Double stranded DNA
- FJC: Freely Jointed chain
- FJC-Ext: Freely Jointed chain - Extensible
- G: Guanin
- mT: Minitweezers
- nm/s: Nanometer/second
- NN: Nearest Neighbor
- LL: Light Lever
- OT: Optical Tweezers
- PSD: Position Sensitive Detector
- RNA: Ribonucleic acid
- SA: Streptavidin
- SME: Single Molecule Experiment
- SMT: Single Molecule Technique
- ssDNA: Single stranded DNA
- T: Timine
- TC: Temperature controller
- WLC: Worm like chain

Chapter 1

Introduction

Biophysics can be defined as an interdisciplinary science which uses the tools, methods and theories of physics to study biological systems. Biophysics studies $life$ at different levels, from atoms and molecules, to cells and organisms. ScientistS of this field, work to gain understanding in areas such as the interactions between the various parts of a cell and how these interactions are regulated (Section 1.1). This chapter introduces the importance of the thermodynamic characterization of nucleic acids and how traditionally thermodynamic properties of DNA have been determined using bulk techniques such as calorimetry or UV absorbance (Section 1.2).

In biophysics one of the main uses of single molecule techniques (Section 1.3), and in particular optical trapping, has been the study of the mechanical and thermodynamic properties of nucleic acids (Section 1.4). Experiments of *mechanical melting* or *unzipping* which consists of pulling apart the two strands of dsDNA until the base pairs are disrupted and the molecule converts into ssDNA are described in section 1.5. The unzipping force provides a direct estimation of free energy differences between the dsDNA and the ssDNA. At the end of this section we introduce the importance of temperature to determine the entropy and enthalpy contributions.

1.1 Molecular biophysics

The cell (from Latin *cell*, meaning ”small room” [1]) is the basic structural, functional and biological unit of all known living organisms. Cells are the smallest unit of life that can replicate independently. Cells consist of a cytoplasm enclosed within a membrane and contains a set of components including membrane, cytoskeleton, organelles and genetic materials. Organisms can be classified as unicellular (consisting of a single cell; including most bacteria) or multicellular (including plants and animals). Most plant and animal cells are visible only under the microscope, with dimensions between 1 and 100μm [2].

All cells contain the hereditary information necessary for regulating cell functions and for transmitting information to the next generation of cells. This process starts in the cell nucleus, which contains most of the cell’s genetic material. This material is organized by a set of macromolecules, called *biomolecules*. The best known among these are Deoxyribonucleic acid (DNA) or Ribonucleic acid (RNA) molecules. The cell also contains a large variety of proteins including histones which help to form chromosomes.

DNA and RNA comprises the nucleic acids, which along with proteins constitute the three major macromolecules essential for all known forms of life. These macromolecules perform multiple vital roles in cellular processes such as genetic transcription, replication and packaging (Fig 1.1).

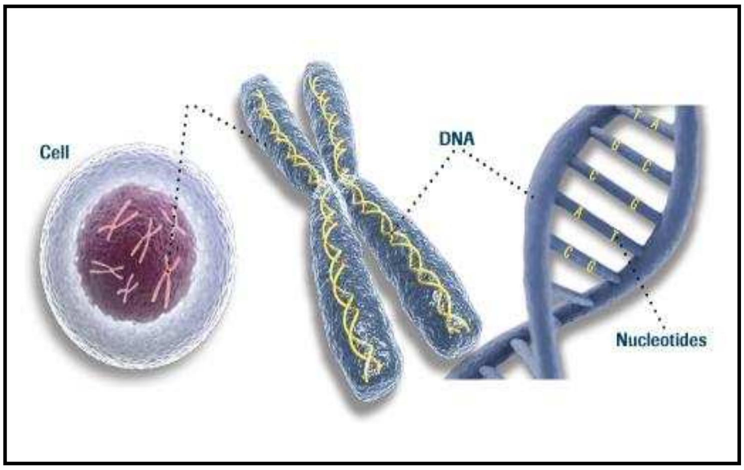

Figure 1.1: *The nucleus of the cell contains chromosomes made from long DNA molecules. The diagram shows the relationship between the cell, its nucleus, chromosomes in the nucleus and the nucleotides of the DNA. The image is originally obtained from the Joint Genome Institute website.*

1.1.1 Molecular Structure of DNA

"*We wish to suggest a structure for the salt of deoxyribose nucleic acid (D.N.A). This structure has novel features which are of considerable biological interest*", these were the first words used by James Watson and Francis Crick when they announce the discovery of the double helix structure of DNA in 1953 [3] (Fig.1.2). The discovery of the structure and function of DNA marked the beginning of *molecular biology* as a field.

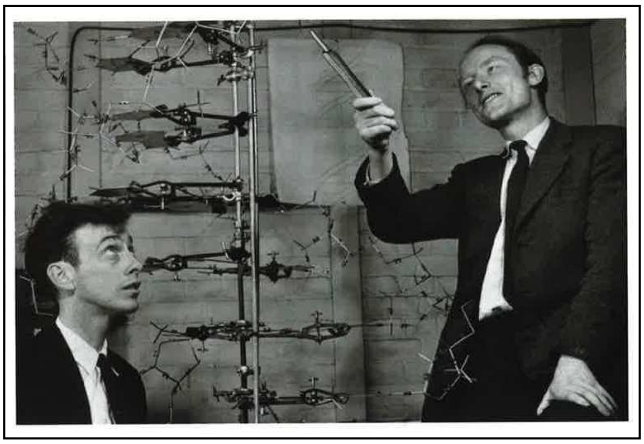

Figure 1.2: *James D.Watson (left) and Francis Crick with their model of DNA molecule in 1953. Image obtained from Special edition* The double helix. *Nature* 50 *years Vol. 421, No. 6921 (23 January 2003).*

DNA is a polymeric chain composed of monomers. The monomer units of DNA are called *nucleotides*. Each nucleotide consists of one molecule of sugar (deoxyribose), one molecule of phosphoric acid and a nitrogenous base attached to the sugar. The phosphate group and the sugar form the external structure of the helix (called the sugar-phosphate backbone) and the nitrogenous bases form the ladder rung like internal structure (Fig.1.3). There are four kind of nitrogenous bases: Adenine (A), Guanine (G), Cytosine (C) and Thymine (T).

The sugar in DNA is a pentose sugar composed by five atoms of carbon and it is called 2-deoxyribose. The sugars are attached together by phosphate groups that form phosphodiester bonds between the third and fifth carbon atoms of continuous sugar rings. These asymmetric bonds mean a strand of DNA has a direction. Both strands are winding around the same axis however the sugar-phosphate backbones of the two DNA strands are antiparallel (5'→ 3' and 3'→ 5'). The asymmetric ends of DNA strands are called the 5' (five prime) and 3' (three prime) ends. The 5'end has a terminal phosphate group and the 3'end has a terminal hydroxyl group. Normally the sequence is written in direction from 5'-end to 3'-end of the sugar-phosphate backbone.

The double helix DNA structure consists of two helical chains each coiled round the same axis with the two chains held together by weak forces (hydrogen bonds). The bases are classified into two types: purines (A and G) and pyrimidines (C and T). The hydrogen bonds are made as follows: T (pyrimidine)-A (purine) and C(pyrimidine)-G(purine). The union between T-A is formed by 2 hydrogen bonds and the union between C-G is formed by 3 hydrogen bonds. The two strands are complementary to each other. As a result, if the base sequence of one strand of DNA is known, the base sequence of its complementary strand can be easily deduced. The complementary strand provides a backup copy of all genetic information encoded within double-stranded DNA. This structure and redundancy of data make double helix DNA a perfect storage mechanism of genetic information.

Hydrogen bonding and stability

As explained in the previous section, the hydrogen bonds between base pairs form inside the double helix. This hydrogen bonding contributes to the stabilization of the molecule, however it is not the only stabilizing factor. There are two factors mainly responsible for the stability of the dsDNA helix: the base pairing between complementary strands (hydrogen bonding) and the stacking between nearest neighbor bases.

The individual bases form stacking interactions between nearest neighbor bases. These interactions are more prevalent in duplexes that in single strands. Stacking is an intermolecular interaction observed in aromatic molecules that tend to stack the bases in a pile. There are two forces that stabilize the stacking interactions, these are hydrophobic. Therefore stabilization of the DNA by base stacking depends on the DNA sequence, as well as the influence of ionic strength [4, 5, 6, 7]. The DNA double helix is considerably destabilized under low salt buffer conditions (10 mM NaCl), while high ionic strength buffers (1 M NaCl) stabilize the double-helical conformation. This effect can be explained by the hydrophobic and electrostatic contributions of the stacking interactions. In conclusion, the stability of the DNA double helix depends on the balance of interactions between hydrogen bonds between base pairs, base-stacking interactions between nearest neighbor bases and the hydrogen bonds between bases and surrounding water molecules.

1.1.2 The hybridization reaction in DNA

The *hybridization* reaction consists of the formation of the DNA double helix though the bonding of two complementary single strands of DNA. If a DNA molecule is sufficiently heated, the energy of the heat will disrupt the bonds pulling the two strands apart. This process is called *denaturation* (also known as *melting*). When the DNA has been denatured it is separated into its two component strands. This happens because the hydrogen bonds between complementary bases are broken and the base stacking is disrupted (Fig.1.4).

The melting of DNA can be caused by a number of physical variables such as change in salt

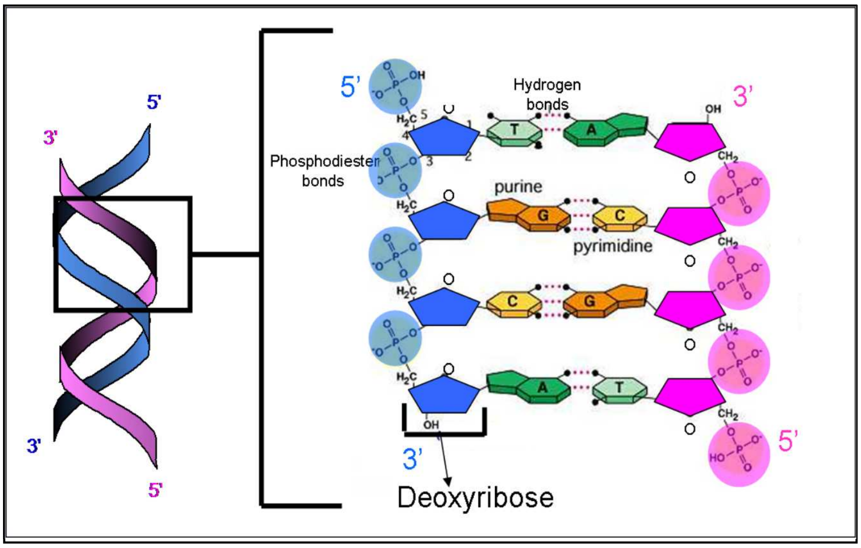

Figure 1.3: *Structure of DNA. DNA double helix and diagram of the 5' and 3' antiparallel strands. Zoom on the detailed structure of the two strands. Each strand is a polynucleotide of deoxyribonucleotides. The sugar-phosphate backbone of the strand is formed by alternately arranged deoxyribose sugar and phosphate molecules which are joined by the phosphodiester linkages. Each sugar in the strand has one base horizontally attached to it at carbon-1. It can be any one of the four: A,T,G or C. These four N-bases can occur in any possible sequence along the length of a strand. The two strands are complementary to each other. Thus, in the double helix, purines and pyrimidines exist in pairs, (A and T) and (G and C). As a result, if the base sequence of one strand of DNA is known, the base sequence of its complementary strand can be deduced.*

concentration, pH or temperature. Melting of DNA by heat is a standard method for preparing single-strand DNA ($ssDNA$). DNA melting occurs in a narrow temperature range. There is a critical temperature called Melting Temperature (T_M) at which this reaction happens. Because the two strands still have the same nucleotide sequences and they are still complementary, if the sample is cooled again, the two strands will eventually find each other through random molecular motion and they will rebound into dsDNA. This process is called *hybridization* or *annealing*.

The G-C union is composed of three hydrogen bonds and the A-T union is composed of only two. Therefore the melting temperature of a particular dsDNA molecule will increase with a higher percentage of GC base pairs. The relationship between melting temperature (T_M) and GC content for long DNA can be expressed as: $T_M = 69°C + 0.41(\%G + \%C)$ [8]. This equation emphasizes that GC pairs are more stable than AT pairs however the phenomenon is more complex because the T_M also depends on the ionic environment, pH and temperature. As it has been shown in different studies ([6, 9, 10, 11, 12, 13, 14, 15, 16]) the T_M depends on DNA length, sequence, ionic environment, pH....

1.2 Thermodynamic characterization of nucleic acids

1.2.1 The Nearest Neighbor model

The Nearest Neighbor (NN) model for DNA was developed by Devoe and Tinoco[17] and Crothers and Zimm [18] in the 1960s. This model predicts the energy formation of the double

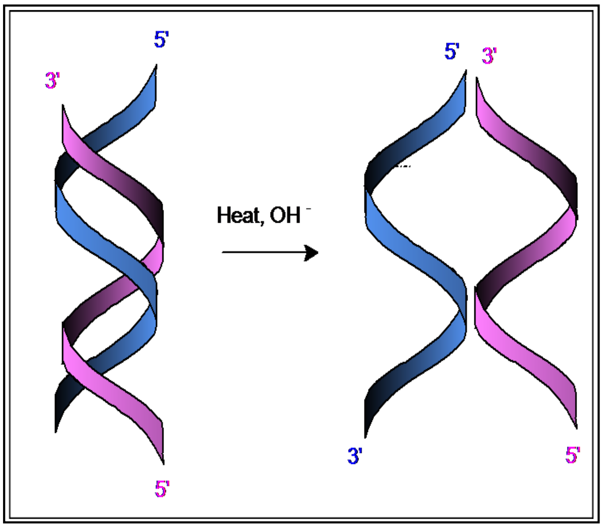

Figure 1.4: *Denaturation of double-stranded DNA.*

helix structure of nucleic acids starting from two single and complementary strands.

This theoretical model shows that the energy between base pairs of two complementary strands depends on the energy of the bases themselves and on that of their nearest neighbors. As Santa Lucia said in his article [6] " *The NN model for nucleic acids assumes that the stability of a given base pair depends on the identity and orientation of neighboring base pairs"*. The NN model assumes that the ssDNA has already been formed (the phosphate backbone is already formed) and only the base-pairing interactions are taken into account.

As has been described, DNA has four types of bases A,T,C,G and by following the NN model there are 4x4=16 different possible interactions (Fig.1.5). However, some combinations are symmetric and these combinations have the same energy. If we discount the symmetric combinations, only 10 different energy values that define the free energy of formation remain. Each combination is called *motif*. The motifs are AA/TT, AT/TA, TA/AT, CA/GT, GT/CA, CT/GA, GA/CT, CG/GC, GC/CG, and GG/CC. The slash ,/, separates strands in antiparallel orientation. The antiparallel orientation means that if the motif AC/TG is oriented as 5'-AC-3', then its complementary base is oriented as 3'-TG-5'. In terms of energy that means that the energy of the duplex can be found by knowing the value of the energy of either strand, as they must be the same in both cases.

The stability of biomolecules is quantified by the standard Free Energy ($\Delta G_{molecule}$) or the difference in Gibbs energy between different states (native and denaturated structures). The total formation energy of the double helix (Free energy) is found by the addition of each Δg_i (formation energy of each motif, depends on itself and on the base pair +1) plus the energy of formation of the ends of the molecule:

$$\Delta G_{molecule} = \sum_i \Delta g_i + \Delta g_{ends} \tag{1.1}$$

To carry out a complete thermodynamic characterization of the molecule the enthalpies (Δh_i) and the entropies (Δs_i) of the motifs must be calculated. The enthalpic and the entropic

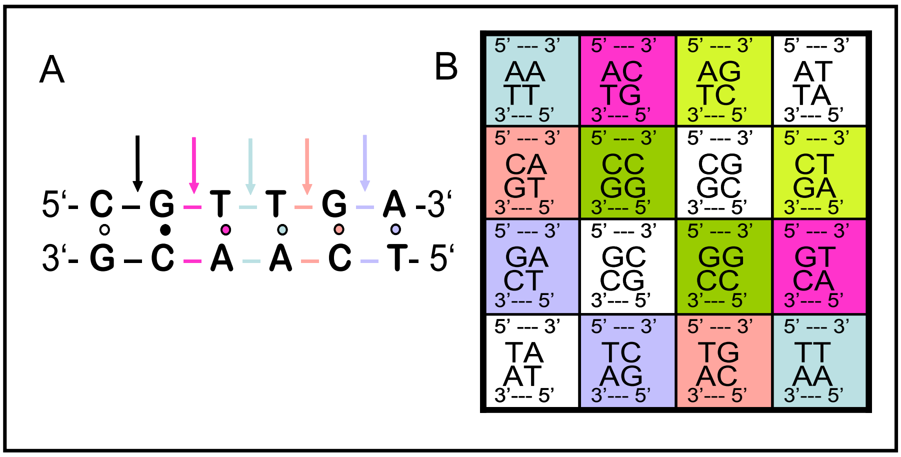

5' --- 3' AA TT 3'--- 5'	5' --- 3' AC TG 3'--- 5'	5' --- 3' AG TC 3'--- 5'	5' --- 3' AT TA 3'--- 5'
5' --- 3' CA GT 3'--- 5'	5' --- 3' CC GG 3'--- 5'	5' --- 3' CG GC 3'--- 5'	5' --- 3' CT GA 3'--- 5'
5' --- 3' GA CT 3'--- 5'	5' --- 3' GC CG 3'--- 5'	5' --- 3' GG CC 3'--- 5'	5' --- 3' GT CA 3'--- 5'
5' --- 3' TA AT 3'--- 5'	5' --- 3' TC AG 3'--- 5'	5' --- 3' TG AC 3'--- 5'	5' --- 3' TT AA 3'--- 5'

Figure 1.5: *Nearest Neighbor model: A. Application of the nearest neighbor model. Each arrow points to the middle of one of the NN basepairs. B. Combination of the 16 NNBP motifs. If we combine all the possibilities (4x4) we can obtain 16 different possibilities. However, there are combinations that are symmetric, and therefore they have the same energy. The symmetric combinations are drawn with the same color. If we discount the symmetric combinations, there are only 10 different energy values.*

contribution of the hybridization reaction can be calculated using the following equations:

$$\Delta H_{molecule} = \sum_i \Delta h_i + h_{ends} \tag{1.2}$$

$$\Delta S_{molecule} = \sum_i \Delta s_i + s_{ends} \tag{1.3}$$

Where h_i is the enthalpic contribution of each motif and s_i is the entropic contribution of each motif. The values h_{ends} and s_{ends} are introduced in the NN model due to the incomplete stacking interaction at the end of the sequences (the last motifs of each chain have no neighbor). This term is a constant contribution independent of the sequence and independent of the motif (h_{ends}=0.2 kcal/mol and s_{ends}=-5.6 cal/mol.K).

To find $\Delta G_{molecule}$ of the molecule, $\Delta H_{molecule}$ and $\Delta S_{molecule}$ are considered to be temperature independent. This allows us to calculate $\Delta G_{molecule}$ as:

$$\Delta G_{molecule} = \Delta H_{molecule} - T\Delta S_{molecule} \tag{1.4}$$

where T is the temperature at which the free energy is calculated.

1.2.2 Melting Temperature

The melting temperature T_M is the temperature at which the hydrogen bonds between the base pairs are disrupted and the double helix is denatured forming two single strands of DNA. The definition of the T_M is the temperature at which half of the molecules of a given sample are in the double helix state and half are in the denatured state.

To find the melting temperature, we assume a model in which ssDNA and dsDNA are suspended in a solution. An equilibrium is established between the ssDNA and the dsDNA molecules. The hybridization reaction can be described as:

$$A[ssDNA] + B[ssDNA] \rightleftharpoons C[dsDNA] \tag{1.5}$$

where $A[ssDNA]$,$B[ssDNA]$ and $C[dsDNA]$ are the concentrations of the ssDNA and the dsDNA.

The NN model predicts the melting temperature of dsDNA. In order to predict the T_M it is necessary to know the enthalpy and the entropy of the formation of the molecule as explained in the last section. At equilibrium, when $\Delta G = 0$, $\Delta G_{molecule}$ is related to the equilibrium constant K_{eq} between the two states by:

$$\Delta G = \Delta G_{molecule} - RTlnK_{eq} = 0 \tag{1.6}$$

where R is the gas constant, K_{eq} is the equilibrium constant and by using Eq.1.4 it is possible to find the T_M

The equilibrium constant K_{eq} can be written as a function of the sum of concentrations of the ssDNA and dsDNA:

$$K = \frac{C[dsDNA]}{A[ssDNA] * B[ssDNA]} \tag{1.7}$$

By considering α as the concentration of single strands in equilibrium (in units of mol/l) where distributed as $A[ssDNA]$ =α, $B[ssDNA]$=α and $C[dsDNA]$=2*α.

By considering that the total concentration of the sample (C_T)defined as: C_T=α+α+2*α=4*α. By definition the T_M is that at which $A[ssDNA] = B[ssDNA] = C[dsDNA]$, therefore it is possible to relate the K_{eq} with the total concentration of the sample as $K_{eq} = (4/C_T)$ therefore $lnK_{eq} = ln(4/\mathrm{C}_T)$.

At $T = T_M$ the hybridization reaction is in thermodynamic equilibrium where Δ G=0. Therefore,for non-self-complementary strands and after rearranging terms:

$$T_M = \frac{\Delta H_{molecule}}{\Delta S_{molecule} + Rln(C_T/4)} \tag{1.8}$$

where $\Delta H_{molecule}$ is the enthalpy change and $\Delta S_{molecule}$ is the entropy change.

1.2.3 Experimental bulk techniques

In the past, thermodynamic properties of DNA have been determined using bulk techniques such as calorimetry [6] or UV absorbance [19], [20]. Both are *denaturation bulk techniques.* The *bulk techniques* use big quantities of samples such as moles, mililiteres and grams.

Calorimetry: It is the classic method used to characterize the thermodynamics of nucleic acid structure. This technique uses heat to study the conformational transitions of biomolecules (for example between the folded and the unfolded structure of a protein or between single and double stranded DNA). Upon heating a sample of DNA, the molecules change conformation from the native state (dsDNA)to the unfolded state (ssDNA). When a biomolecule changes its thermodynamic state (dsDNA to ssDNA), a heat capacity change (ΔC_p) is observed in the solution in which the sample molecules are suspended. This change is due to the fact that the heat required to raise the temperature of a solution of unfolded molecules is greater than that required for a solution of native molecules. Heat capacity changes are due to the restructuring of the solvent molecules around the no-hydrophobic side of the chain exposed to the solvent during the unfolding process.

The technique of calorimetry measures the excess heat capacity of a solution (C_p) of the molecule of interest as a function of T (Fig.1.6). The transitions shows a peak where the maximum value of C_p is obtained at T_M. The area of the curve C_p versus T provides the value of $\Delta H_{molecule}$ and the shift in the baseline yields the ΔC_p that is the characteristic signature of a first-order phase transition separating two conformations.

This technique measures directly the $\Delta H_{molecule}$ with an accuracy of 2-5 % [6]. If it is plotted $\Delta C_p/T$ vs T the area between this curve is provide us $\Delta S_{molecule}$. From $\Delta H_{molecule}$ and $\Delta S_{molecule}$, the value of $\Delta G_{molecule}$ can be determined [21].

UV absorbance:Heating the double stranded DNA sample causes the denaturation of the molecule by disrupting the stacking of the bases and by breaking the hydrogen bonds. This process can be monitored by an increase in UV absorbance (A) as the double strands converts into single strands. Fig.1.6.B shows a melting curve (UV absorption as a function of temperature). This transition is expressed as a curve where UV absorption increases with temperature and the T_M is the temperature at the maximum absorbance gradient (dA/dT) which corresponds to the 50% of the concentration of dsDNA and ssDNA. This technique measures the absorbance and concentration of the sample (C_T) vs T. The curve $1/T_M$ vs $ln(C_T/4)$ allow us to extract the values of $\Delta H_{molecule}$ and $\Delta S_{molecule}$ by a Van't Hoff analysis following the relation: $1/T_M = (R/\Delta H_{molecule})ln(C_T/4) + (\Delta S_{molecule}/\Delta H_{molecule})$ (Eq.1.8).

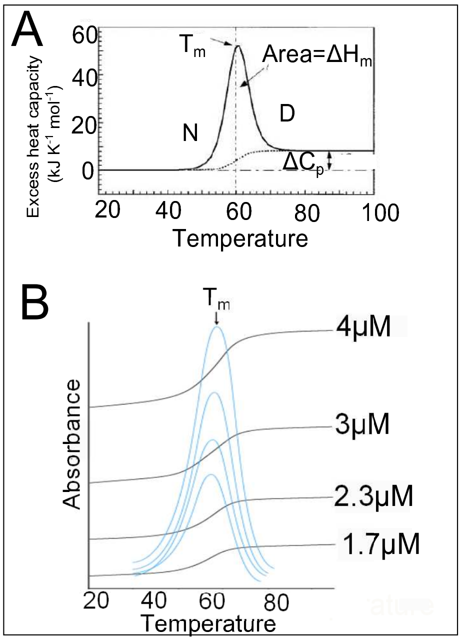

Figure 1.6: *Thermodynamic characterization by bulk techniques: A. Differential scanning calorimetry (DSC) experiment for the two-state unfolding of a globular protein (Adapted from [21]). B. UV melting curves*

1.2.4 Unified Oligonucleotide predictions

As explained in previous sections, *thermal denaturation* has been used to measure the *melting temperature* of DNA duplex formation and the NN model is used to predict the melting temperature of DNA molecules and to make a thermodynamic characterization.

In 1998 John Santa Lucia [6] reported the experimental results in DNA melting obtained by several labs that were found to be in fairly good agreement and provided a set of 10 NNBP energies determined using the Calorimetry technique. These values are known as the Unified Oligonucleotide (UO) values (Fig.1.7). These UO values are now considered a very successful model and they have been used in the MFOLD program for the prediction of the secondary structure of biomolecules. The UO values have been followed as a reference for single molecule experiments too [14, 22].

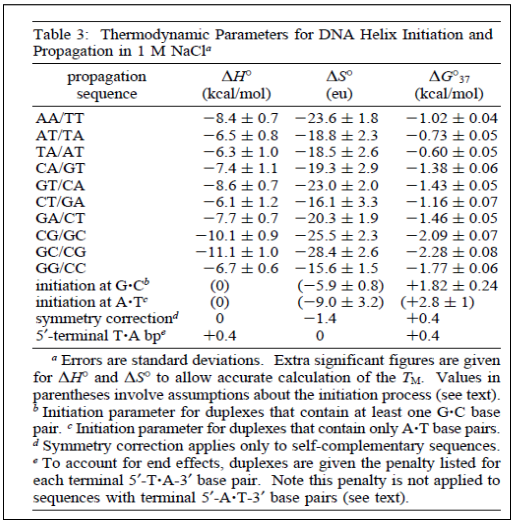

Table 3: Thermodynamic Parameters for DNA Helix Initiation and Propagation in 1 M NaCl[a]

propagation sequence	ΔH° (kcal/mol)	ΔS° (eu)	ΔG°_{37} (kcal/mol)
AA/TT	-8.4 ± 0.7	-23.6 ± 1.8	-1.02 ± 0.04
AT/TA	-6.5 ± 0.8	-18.8 ± 2.3	-0.73 ± 0.05
TA/AT	-6.3 ± 1.0	-18.5 ± 2.6	-0.60 ± 0.05
CA/GT	-7.4 ± 1.1	-19.3 ± 2.9	-1.38 ± 0.06
GT/CA	-8.6 ± 0.7	-23.0 ± 2.0	-1.43 ± 0.05
CT/GA	-6.1 ± 1.2	-16.1 ± 3.3	-1.16 ± 0.07
GA/CT	-7.7 ± 0.7	-20.3 ± 1.9	-1.46 ± 0.05
CG/GC	-10.1 ± 0.9	-25.5 ± 2.3	-2.09 ± 0.07
GC/CG	-11.1 ± 1.0	-28.4 ± 2.6	-2.28 ± 0.08
GG/CC	-6.7 ± 0.6	-15.6 ± 1.5	-1.77 ± 0.06
initiation at G·C[b]	(0)	(-5.9 ± 0.8)	$+1.82 \pm 0.24$
initiation at A·T[c]	(0)	(-9.0 ± 3.2)	$(+2.8 \pm 1)$
symmetry correction[d]	0	-1.4	$+0.4$
5′-terminal T·A bp[e]	$+0.4$	0	$+0.4$

[a] Errors are standard deviations. Extra significant figures are given for ΔH° and ΔS° to allow accurate calculation of the T_M. Values in parentheses involve assumptions about the initiation process (see text). [b] Initiation parameter for duplexes that contain at least one G·C base pair. [c] Initiation parameter for duplexes that contain only A·T base pairs. [d] Symmetry correction applies only to self-complementary sequences. [e] To account for end effects, duplexes are given the penalty listed for each terminal 5′-T·A-3′ base pair. Note this penalty is not applied to sequences with terminal 5′-A·T-3′ base pairs (see text).

Figure 1.7: *UO values given by [6]. The UO values are given at standard conditions of pH 7.0, 25° C and 1 M NaCl. These values are considered a very successful model and have been used in the MFOLD program for the prediction of the secondary structure of biomolecules.*

The UO values are given at standard conditions of pH 7.0, 25°C and 1 M NaCl. Some corrections have been made to extend the values to other conditions of temperature and salt concentration. However, it was shown in the work published by Huguet et.al, that some discrepancies appear between the *single molecule experiment* predictions and the UO predictions.

1.3 Single Molecule Techniques

The structural property of DNA is important for biological processes such as transcription and replication reactions where genetic information needs to be read. Some of the mechanical and elastic physical mechanisms governing biomolecule processes inside of the cell are force, tension and deformation. During the last decades scientific instruments and techniques to manipulate and visualize individual cells or molecules and measure microscopes forces have been developed. These techniques are known as the *Single Molecule Techniques* (*SMT*) [23]. Some of these are: Atomic Force Microscopy (*AFM*), Magnetic tweezers (*MT*), Single-molecule fluorescence (*SMF*) and Optical Tweezers (*OT*) among others. A comparison of the OT method with various others SMT can be found in Table 1.1. The relevant force ranges, minimum displacements, probe stiffnesses, practical advantages and consequently the applications of each technique vary significantly.

Methods	$F_{min-max}(pN)$	$x_{min}(nm)$	$k(pN.nm^{-1})$	Advantages
AFM	$10^1 - 10^5$	10^{-1}	$1\text{-}10^6$	High spatial resolution
MT	$10^{-2} - 10^1$	10^1	Not defined	Specificity to magnets/Ability to induce torque
OT	$10^{-1} - 10^2$	1	$10^{-1} - 10^2$	High force resolution/Specific manipulation

Table 1.1: *Methods of single molecule manipulation. Summary of the range of minimum and maximum forces, distance resolution, stiffness and advantages of this technique.*

These techniques allow us to obtain information complementary to the traditional bulk studies explained in section 1.2.3. With these techniques it may be possible to measure forces in the range of 0.1-1000 pN and distances down to 1 Armstrong. the principal difference between the SMT and the bulk experiments is that by using SMT a individual molecule can be manipulated and analyzed one at a time. With the Single Molecule manipulation techniques is not necessary to relay on the averages used in bulk studies. SMTs allow us to access biomolecular processes by following a single molecule and measuring instantaneous deviations from the average behavior. By using SMTs it is possible to characterize kinetic reactions and potentially observe kinetic intermediates that are difficult to detect using bulk techniques. Some of these techniques, such as SMF allow us to visualize the experiments which helps us to understand the process. A recent trend is to combine different SMTs to give knowledge about molecular systems.

1.4 Introduction to the Optical tweezers technique

1.4.1 Historical view

Optical tweezers find application in a wide range of disciplines, including physics and biology. The first observations of radiation pressure on matter date back to 1609 when German astronomer Johannes Kepler noticed that the tails of comets always point away from the Sun. In 1876 scientist James Maxwell theorized that electromagnetic radiation can exert a pressure upon a surface. Arthur Ashkin was a pioneer in radiation pressure experiments. In 1971 he was the first to observe how by using a single laser beam it was possible to accelerate a tiny particle, such as polystyrene microspheres along the path of the laser light [24].

Moreover, in 1978 Ashkin used two opposing laser beams to trap and cool atoms [25]. In 1986, Ashkin developed the first optical trap. He had the idea to focus a laser, by using an objective lens, so that a dielectric micro-particle feels the gradient force that tends to take it into the region of maximum intensity of light [26] (Fig.1.8). By using this method an optical trap can be formed when the gradient force is higher that the scattering force. This describes the single beam scheme of optical tweezers. By using this setup Ashkin and co-workers demonstrated that optical tweezers can manipulate a wide range of particles with diameters between 25 nm and 10 μm. In 1987 some biological specimens such as Escherichia coli bacteria, Tobacco mosaic virus and protozoas were trapped for the first time with an Argon laser of 514.5 nm and also with 1064 nm Nd:YAG laser [27], [28]. With the YAG laser damage to the cells and organisms is avoided while still allowing them to be manipulated. Following this the instrumentation and applications of the optical tweezers improved together throughout the 90's.

1.4.2 Applications of Optical Tweezers

Manipulation of biological systems with OT began with large objects, such as bacteria, organelles and cells. However, recently optical trapping combined with microsphere handles linked

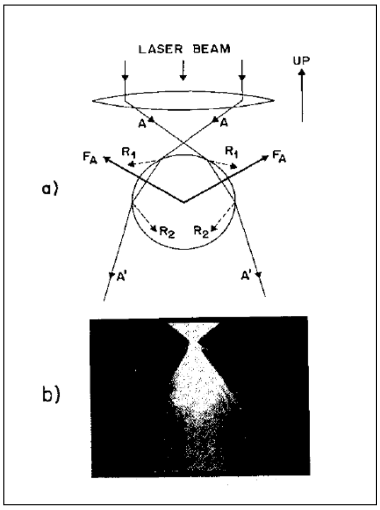

Figure 1.8: *Figure from the 1986 seminal paper by Ashkin et.al, demonstrating single-beam gradient force optical trapping. This image taken by fluorescence demonstrated the optical trapping of a micro-sphere (of 10 μ m of diameter) showing the incident and the scattering light rays. Figure taken from [26].*

to biomolecules of interest (such as DNA, RNA, proteins and molecular motors) has enabled single molecule biophysics experiments [29]. This area of research includes DNA elasticity [30, 31], the behavior of molecular motors [32, 33] and protein folding [34]. In comparison with different methods of SMT, OT present several unique advantages.

The force on the trapped object can be calibrated against displacement and laser power, this provides a method of direct, high-resolution force and position measurement (< 1 pN and < 10 nm, respectively). Moreover OT allows forces to be exerted and measured in a range between 10^{-1} - 10^{2} pN and with a spatial resolution of 1 nm in distances. This resolution is ideal for single molecule biophysical experiments. A major disadvantage of OT is the laser damage that can be produce in some of the biological samples [32]. Also, the limitation of handling only one molecule at a time, makes it necessary to perform several repeated experiments in order to collect enough statistical data to extract reliable conclusions.

The experimental configurations of the OT are highly variable and depend on the kind of experiment the scientist is interested in conducting. Normally the experimental conditions consist of a molecular construction divided into two parts: the molecule under study and the handles that link the molecule to the microspheres. The handles are used as spacers to separate the sequence of the molecule from the beads. This prevents the beads from coming into contact with each other. Usually the optical trap works as the sensor of force and the point of reference is a fixed anchor such as a micropipette or a glass microscope coverslip surface.

Applications for OT include experiments in the areas of mechanical, kinetic and thermodynamic properties of biomolecules.

The mechanical properties of the nucleic acids are observed in biological process such as packing, replication or transcription carried out by proteins on the DNA molecule. These proteins apply tension on the DNA to open or unpack the dsDNA. One typical experiment to characterize the mechanical properties of a single biomolecule is to exert mechanical force by pulling the ends of the molecule. This kind of experiment allows the investigation of the elastic response of the molecule. The first experiment conducted into the elasticity of the DNA were completed using magnetic tweezers [30]. Some years later, the same group repeated the same experiment using OT [35] (Fig.1.9). Other experiments have been carried out to study the behavior of the elasticity of DNA by changing some physiologically relevant conditions such as pH [16], ionic concentration [36] or temperature [37]. Other experiments have been conducted using OT to explore protein folding [34] and the behavior of molecular motors [41].

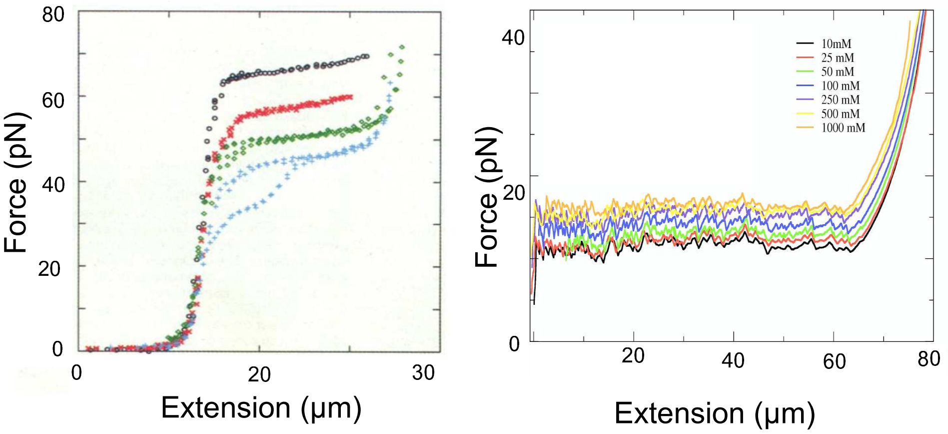

Figure 1.9: *A. Figure taken from [30]. Force versus Extension (FEC) curve characteristic of DNA. The black curve show a full stretching/relaxing cycle of a dsDNA molecule from* λ*-phague DNA at 150 mM NaCl, 10 mM Tris, 1mM EDTA, pH.8.0. The red curve at 5mM, the green curve at 2.5 mM and the blue curve at 0.625 mM. B. Figure taken from [40]. Unzipping the molecular construct by varying monovalent salt concentrations (10, 25, 50, 100, 250, 500 and 1000 mM of NaCl).*

1.5 Temperature in molecular biology

As has been explained in section 1.3, the development of a new technology to manipulate biological molecules or biological motors has opened a new area of investigation in the biophysical properties of small biosystems.

A characteristic property of small biosystems is that the energy that they interchange with the environment is of the same order of magnitude as that of the thermal fluctuations around them. As a consequence, the thermal fluctuations of the system contain important and valuable information. For example, molecular motors with dimensions around 100nm work in molecular processes on the order of a few $k_B T$, where 1 $k_B T$=4pN.nm at T=298K. Then, by using, SME it is possible to observe and to deduce the rare events and the large deviations from the average behavior. This new area of study is called $The\ Non-equilibrium\ thermodynamics\ of\ small\ systems$ [41, 42].

In macroscopic systems, the thermal fluctuations are small in comparison with the average behavior. It is only under very specific conditions that these kinds of fluctuations produce significant consequences in macroscopic systems. However in the case of microscopic systems, the interactions of microscopic objects with their environment is dominated by thermal fluctuations. Specially, in a nonequilibrium microscopic system, thermal fluctuations can produce large deviations from the average behavior. For example, one of the more interesting topics in small systems are the molecular motors of the cell. In this type of biomolecule, thermal fluctuations are very important because they determine the efficiency of the molecular machine. Thermal fluctuations dominate the behavior of such motors.

Molecular motors are complexes which work as transducers of chemical energy into mechanical work used for the mobility of the entire cell, intracellular transport or replication, transcription and repair of DNA. The energy and kinetic cycles that convert chemical energy into force are affected by temperature change and the speed of a molecular motor is dependent on thermal fluctuations and therefore on T.

1.5.1 Measurement of free energy in mechanical melting of DNA

In *mechanical melting* or *unzipping* experiments, mechanical force is applied to the ends of the DNA molecule. The molecule is pulled until a critical value of force is reached and the molecule starts to unfold until the base pairs are disrupted and the molecule converts into ssDNA. A loop at the end keeps the two strands linked and allows the elastic response to the ssDNA to be recorded. When the pulling process is reversed the molecule refolds again.

In this kind of experiment the force exerted upon the system is recorded as a function of f vs distance giving the so-called the Force-Distance Curve (FDC) (Fig.1.10). During the unzipping process, the molecule is pulled at very slow speed to permit a reversible path process which means that free energy of the system can be obtained by knowing the area under the FDC curve:

$$\Delta G = \int F dx \tag{1.9}$$

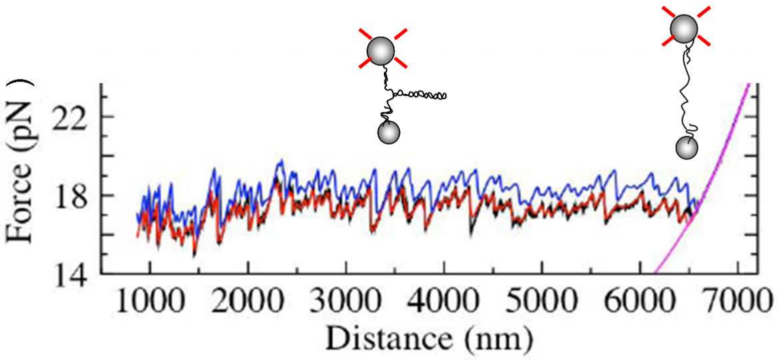

Figure 1.10: *Force - Distance curve (FDC) for a sequence of 6.8kb λ-phage DNA at 1M NaCl, pH:7.5. The black curve is the experimental measurement taken with an OT setup. The blue curve is a prediction obtained used the values of UO. The red curve is the theoretical prediction produced by Hughet.et.al. Figure modified from [14]*

Although the unzipping curve provides a direct estimation of $\Delta\ G_{molecule}$, to extract the value of T_M requires knowing the entropic contribution ($\Delta\ S_{molecule}$) and enthalpic contribution ($\Delta\ H_{molecule}$) of the melting process. However, it has not yet been possible to accurately measure the enthalpy and the entropy in single molecule experiments. To carry out a full thermodynamic characterization of nucleic acids both magnitudes (force and temperature) must be known. The best way to carry out this analysis is by conducting unzipping experiments of DNA at different temperatures. For this reason it is useful to implement a temperature control function in the instrument capable of measuring unzipping curves at different temperatures.

This thesis will describe our efforts to develop and implement an optical tweezers setup with a real-time temperature control system capable of conducting single molecule experiments at various temperatures allowing the accurate measurement of entropy and enthalpy of single molecules.

Chapter 2

Objectives

The OT is a versatile instrument which allows us to change the physiological conditions in the experiments such as the ionic strength buffer and the pH in real time without interrupting the experiment. This allows us to conduct experiments on one individual molecule while surrounding conditions are changed. However, until now, the temperature (T) has been an experimental parameter difficult to control in this instrument.

A significant amount of research has been done throughout the last 15 years in an attempt to find a method to control the temperature in OT. One of the principal problems in building a temperature controller (TC) is the limited working space of the instrument. Traditional OT instrument are quite large often occupying an entire optical table. This makes the placement of the entire instrument in a heated or cooled environment problematic. In order to heat/cool the experiments by Williams et. al [16] made a Peltier heater-cooler device connected to the fluidic-chamber by copper plates. Their method used air-gap objectives so that there was no immersion fluid and the objective lenses did not get hot or cold with the chamber. However they found some serious problems with the air objectives which had a N.A=0.9. With this N.A the force and the distance are not as accurate as with other types of lenses. Mao et.al [43] used water immersion objectives (N.A=1.2) with hot-cold circulating water collars on the objective lenses. In this setup the fluidic-chamber comes to the same temperature as the objective lenses due to heat conduction through the immersion fluid. The use of the cooper jackets allowed them to create a homogeneous cold or hot region though the immersion fluid meniscus and the coverslip glass creating an area where the temperature inside of the chamber was uniform. With this method it is possible to obtain temperatures between 5°C and 70°C. However, one of the disadvantages of this method is the thermal drift produced in the objective lenses when they are heated. The dimensions of the objective lenses change by many microns during a temperature cycle and thus the dual-beam trap goes out of alignment. It is necessary to wait for many hours for the objective lenses to equalize before the experiments can continue. Therefore it was not possible to perform experiments on the same molecule at different temperatures. In addition Mao et. al [43] tested a laser-heating method finding 4 important problems that were not be easily resolved. First, the convection effect inside of the chamber would disrupt the experiment. Second, this method could only heat the buffer solution. Third, the laser used to heat the experiment could only increase the temperature by 6°C. Fourth, the heating laser was focused in a small spot thus producing another optical trap. This effect produces that the bead is sucked partially away from the primary optical trap. The aim of our project is build a TC for an OT instrument to measure the free energy, enthalpies and entropies at the single-molecule level. In the next section we will explain how we overcame the problems described above to develop a functional TC system in an OT setup.

This thesis is structured as follows:

- Chapter 3 contains the description of some of the applications of the OT setup. This chapter explains in detail different kinds of experiments and several methodologies carried out to study thermodynamic and kinetic properties on DNA hairpins. Although these works are not the direct aim of my thesis project, I have made contributions in each of them during my time with the Small Biosystems Lab. These projects have importance in my scientific formation because they have allowed me to learn how to perform various types of experiments on DNA hairpins and to develop and implement new technology such as the Fast Data Acquisition system in the OT setup (Appendix A).

- In Chapter 4 an introductory description about the theory of optical trapping is provided. The description of the OT setup is explained in detail and the methods to calibrate the instrument are detailed as well. A full description of the OT with the Temperature Controller and the tests carried out to obtain a range of temperature between 5°C and 50°C is described in detail in this chapter. The methodology of the unzipping experiments and the theoretical models used to analyze ssDNA are described at the end of this section.

- Chapter 5 describes how using *mechanical melting* or *unzipping* experiments we have measured how the rupture forces of dsDNA vary with temperature. The change in entropy is derived from the force vs temperature analysis. This analysis has been compared with results obtained from past experiments. Moreover we have conducted single molecule experiments with buffers of various concentrations of salt at various temperature. With these experiments we have been able to show in detail how temperature affects molecular extension. Moreover we have carried out the characterization of ssDNA elasticity at different temperatures with unexpected results. Finally we have analyzed the enthalpy/bp, entropy/bp and the free energy/bp of the dsDNA formation.

- Chapter 6 summarizes the main conclusions derived from this phD thesis.

Chapter 3

Applications of Optical Tweezers

Applications for OT include experiments in diverse areas of mechanical, kinetic and thermodynamic properties of biomolecules. The biomolecules exhibit complex free energy landscapes that determine the molecular folding kinetics and influence the way the molecules fold into their native structures. The application of forces makes it possible to disrupt the bonds (hydrogen bonds plus stacking interactions) from their native configuration and to arrive at a stretched unfolded configuration. This kind of experiment allows us to determine the thermodynamics (e.g the free energy of formation) and kinetics (e.g. the rates of folding and unfolding) of the DNA hairpin.

Following are some examples of the many applications where the OT instrument has been used:

Improving signal-to-noise resolution in single molecule experiments using molecular constructs with short handles. *Forns.et.al [44] have investigated folding/unfolding kinetics in DNA hairpins with a novel design of short dsDNA handles of 29 bp in comparison with the conventional long handles constructed of approximately 700bp. In this work hopping experiments have been carried out [45, 46], where the molecule transitions between different states while the trap-pipette distance is maintained stationary (passive mode) or the force is maintained constant with a feedback system (constant-force mode). By using the hopping experiments it is possible to investigate the kinetics of the DNA hairpin. By meaning the lifetime of the molecule in each state, it is possible to obtain the rates of the folding-unfolding transition. Furthermore, these experiments allow us to determine the parameters that characterize the shape of the free energy landscape, such as the free energy of formation. The short handles are very rigid and are expected to behave like rigid rods that fully transmit forces to the DNA hairpin. The higher stiffness of the new molecular setup intensifies the signal-to-noise ratio (SNR) and slows down the folding/unfolding kinetics aiding the detection of the fast structural transitions. This methodology can be extended to other single molecules (e.g. RNA and proteins).*

In this work, the experiments with the short handle constructs have been carried out on two different DNA hairpins: 1) a hairpin that folds and unfolds in a cooperative two states manner (called 2S hairpin) (sequence and the free energy landscape shown in Fig.3.1, A and B) and 2) a hairpin that has a fast intermediate state (called 3S hairpin) (sequence and the free energy landscape shown in Fig.3.2, A and B). In order to investigate the folding/unfolding kinetics and the thermodynamics of these hairpins, hopping experiments have been carried out in passive mode and in constant force mode.

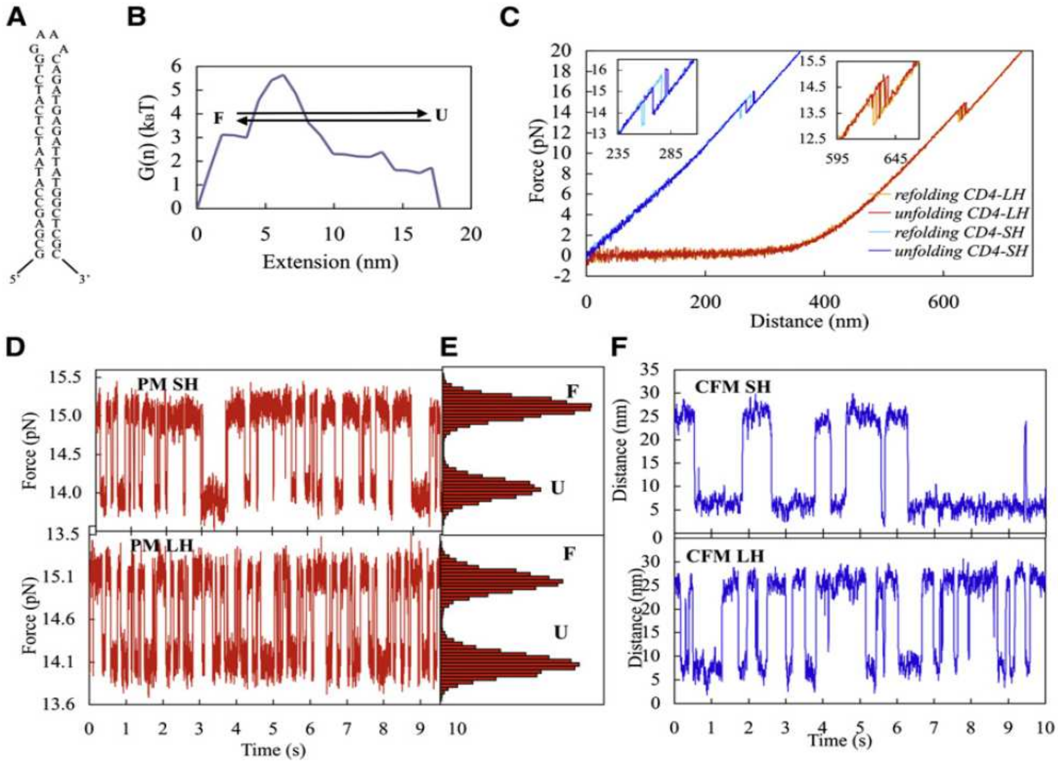

Figure 3.1: *Figure taken from [44]. (A) Sequence of the hairpin. (B) Free energy landscape plotted as a function of the molecular extension (nm) at force $f = 14.1$ pN (at 25° C and 1M NaCl). This was computed as described in Section S1. We also indicate the different transition rates (arrows). (C) FDC of pulling experiments with long and short handles. The insets show the unfolding and refolding of the hairpin. (D,E) Force traces and their distribution in the PM experiments for the short (upper panels) and long handles constructs (lower panels). (F) Time-dependent relative distances in the CFM experiments for the short (upper panel) and long handles constructs (lower panel).*

The free energy landscapes as a function of the molecular extension have been calculated for hairpins 2S and 3S at various forces by using the free energy values from Mfold server at 25°C 1M NaCl. The predicted free energy landscape of the 2S hairpin (Fig.3.1.B) at the coexistence force of 14.6 pN shows two equal free energy minim (corresponding to the folded -F- and unfolded -U- states) separated by a single free energy barrier. The folding/unfolding reaction of the 2S hairpin can be schematically described by:

$$F \overset{k_{FU}}{\rightarrow}\overset{k_{UF}}{\leftarrow} U \tag{3.1}$$

where k_{FU} and k_{UF} denote the force dependent unfolding and folding rates between states F and U as given by:

$$k_{s\rightharpoonup s'} = k_m e^{\beta f x_{ss'}} \tag{3.2}$$

$$k_{s'\rightharpoonup s} = k_m e^{-\beta f x_{s's}+\beta\Delta G_{ss'}} \tag{3.3}$$

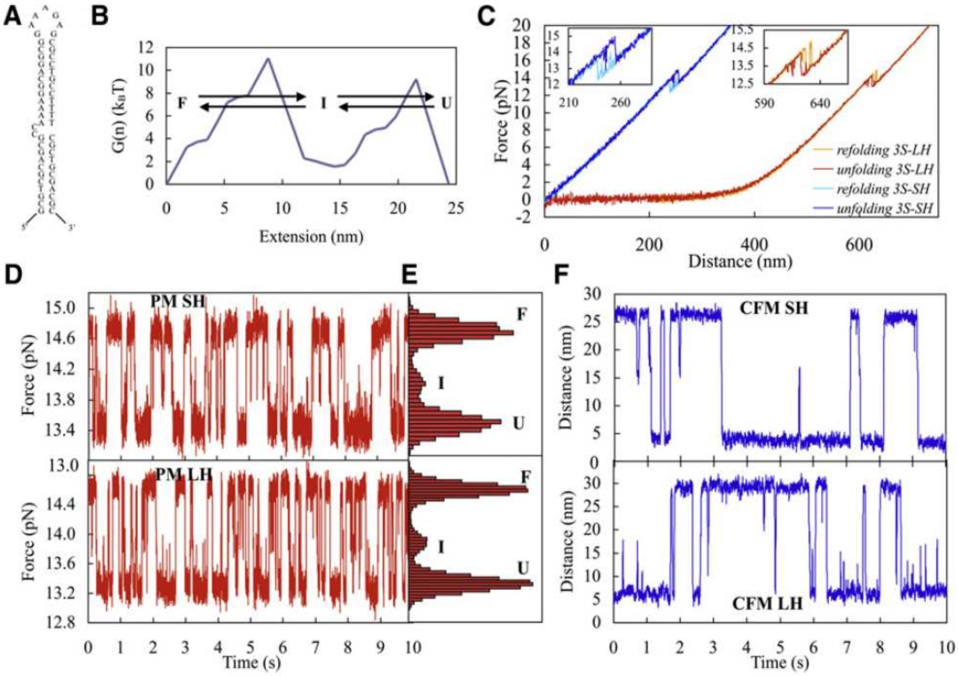

Figure 3.2: *Figure taken from [44]. (A) Sequence of the hairpin. (B) Free energy landscape plotted as a function of the molecular extension (nm) at force f = 14.1 pN (at 25° C and 1M NaCl). This was computed as described in Section S1. We also indicate the different transition rates (arrows). (C) FDC of pulling experiments with long and short handles. The insets show the unfolding and refolding of the hairpin. (D,E) Force traces and their distribution in the PM experiments for the short (upper panels) and long handles constructs (lower panels). (F) Time-dependent relative distances in the CFM experiments for the short (upper panel) and long handles constructs (lower panel).*

where according to Bell-Evans theory it is possible to determine the parameters of the free energy landscape ($\Delta G_{ss'}$, B, $x_{ss'}$ and $x_{s's}$) by fitting the kinetic force-dependent rates to the 3.2 and 3.3 equations. This model involves four parameters: the free energy difference between states s and s', $\Delta G_{ss'} = G_{s'} - G_{s'}$; the height of the kinetic barrier B, defined as the free energy difference at force f between the TS and the s state; and the distances $x^{+}_{ss'}$ and $x^{+}_{s's}$ along the reaction coordinate that separates the TS from the s and s' states respectively. In these equations $\beta = 1/k_BT$, k_B is the Boltzmann constant and T is the room temperature. The coexistence rates $k^{c}_{ss'}$ and coexistence forces $f^{c}_{ss'}$are defined by $k^{c}_{ss'}$=$k_{s\rightharpoonup s'}(f^{c}_{ss'})$ =k$_{s'\rightharpoonup s}(f^{c}_{ss'})$.

In all cases free energy differences, molecular extensions and coexistence forces could be also estimated by using the balances property or Van't Hoff equation:

$$\Delta G_{ss'}(f) = -k_BTlog(w_{s'}/w_s) = \Delta G_{ss'} - fx_{ss'} \tag{3.4}$$

where $x_{ss'} = x^{+}_{ss'} + x^{+}_{s's}$ and w_s and $w_{s'}$ are the statistical weights of states, s and s' respectively.

The predicted free energy landscape for the 3S molecule at the coexistence force between the folded and unfolded states (14.1 pN) shows the presence of an intermediate on-pathway generated by the entropy cost associated to the internal loop. The sum of the distances between folded (F) and intermediate (I) and between intermediate (I) and unfolded state (U) at the coexistence force is 22.6 nm, consistent with the extension change measured during unfolding of the 3S hairpin in CFM, 22.0±1.1 nm (average over 9 molecules, see Fig. 3.2). Four different transition rates describe the force kinetics in the 3S hairpin. These transition rates are described by the following scheme and are illustrated in Fig. 3.2.B:

$$F \overset{k_{FI}k_{IF}}{\rightarrow\leftarrow} I \overset{k_{IU}k_{UI}}{\rightarrow\leftarrow} U \tag{3.5}$$

where k_{FI}, k_{UI}, k_{IU}, k_{IF} stand for the force dependent transition rates between states F, I and U as given by Eq.2 and Eq.3.

The thermodynamic parameters, such as coexistence forces, molecular extensions and folding free energies have been obtained from the hopping traces using two different molecular constructs. The results in both cases are consistent for the two kinds of hairpins (2S and 3S). The main differences observed between the two constructs of handles is in the folding/unfolding rates. As expected the higher effective stiffness of the experimental setup in the short construction leads to slower kinetics. Therefore the higher stiffness of the new molecular setup intensifies the signal-to-noise ratio (SNR) and slows down the folding/unfolding kinetics aiding the detection of the fast structural transitions.

To evaluate and quantify the elastic properties of the molecular setup based in the short handles, a novel method based on the high-bandwidth noise force fluctuations at different forces has been developed. This method allows us to determine the stiffness of the trap, and at the same time, to characterize the elastic properties of the molecular system tethered between the beads.

In the past, several works have explained how the length of the handles, the stiffness of the optical trap and instrument limitations affect the measurement of kinetic properties of the molecule [47, 48, 49]. The signal to noise-ratio (SNR) of the measurements, limited by the Brownian motion of the bead $<\delta x^2>$, depends on the stiffness of the molecular construct attached to the bead (handles plus hairpin), ϵ_x, and that of the trap, ϵ_b, as given by the fluctuation-dissipation theorem:

$$<\delta x^2>=\frac{k_B T}{(\epsilon_b+\epsilon_x)} \tag{3.6}$$

or

$$<\delta f^2>=\frac{k_B T \epsilon_b^2}{(\epsilon_b+\epsilon_x)} \tag{3.7}$$

Note that ϵ_x is the combined stiffness of two serially connected springs: one represented by the handles and the other by the hairpin. Along the folded branch we assume a very rigid hairpin, ϵ_x being just the stiffness of the handle. According to the Eq.3.5 and Eq.3.6, the stiffer the linker the higher the SNR is, to confirm this the variance of the signal from 1 pN to 15 pN have been measured with the short and long handled constructions. The next figure shows some examples of force-time traces for both constructions and the result of the force variance for both cases. The force variance is higher with long handles. The SNR measured for the 2S hairpin at the critical force is 6.2 ± 0.3 and 8.0 ± 0.8 for long and short handles respectively.

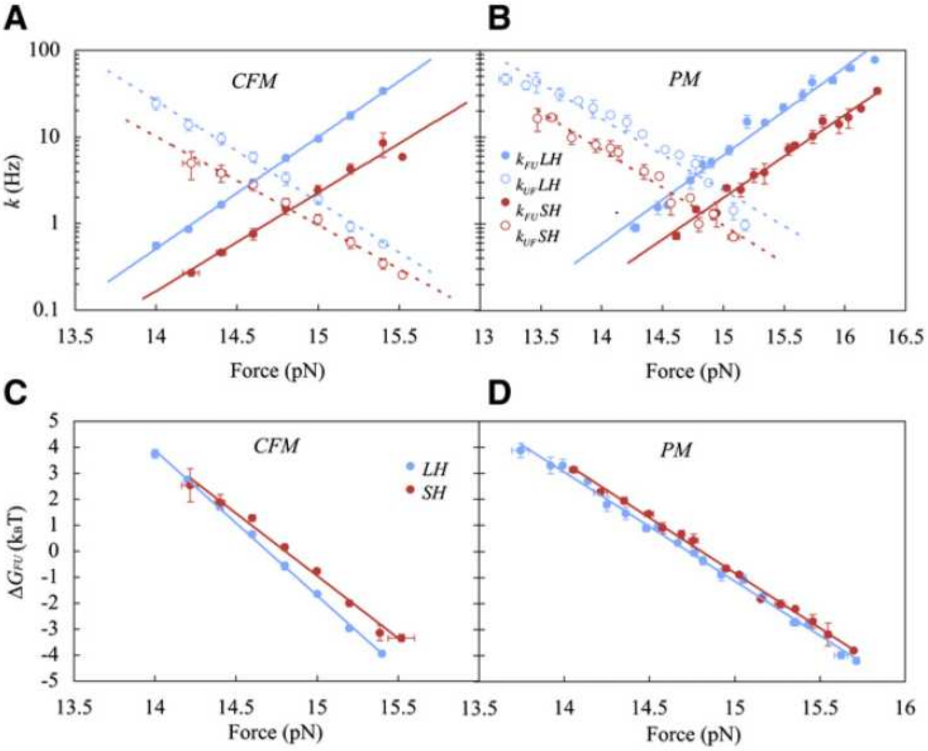

Figure 3.3: *Figure taken from [44]. Results for the 2S hairpin with short handles (red or dark gray) and long handles (blue or light gray) (color online). (A and B) Plots of k as a function of force for CFM experiments (A) and PM experiments (B) and the linear fit (lines) for the log of the rates, where solid symbols and lines represent the unfolding rate (k_{FU}) and dotted symbols and lines the folding rate (k_{UF}). (C and D) Plots of the ΔG_{FU} versus force for CFM (C) and PM (D) experiments and their linear fit (lines). We show the mean values for each point and the standard error.*

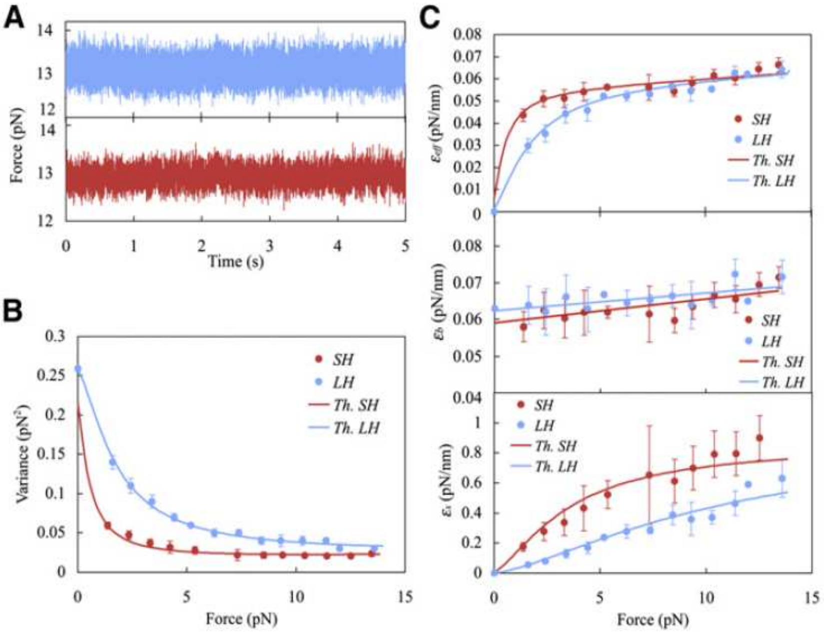

Figure 3.4: *Figure taken from [44]. Analysis of force variance and stiffness (from 1 to 15 pN) for 2S hairpin. (A) Typical force traces (at ± 13 pN) with long (blue) and short handles (red). (B) Measured force variance for short (red circles) and long handles (blue circles). (C) The measured effective stiffness (ϵ_{eff}, top panel), the stiffness of the trap (ϵ_b, middle panel) and the stiffness of the molecular system (ϵ_x, bottom panel) for short (red circles) and long (blue circles) handles. Fits to the elastic model are shown for long (blue line) and short (red line) handles. Results are the average over 3 and 4 different molecules for the short and long handles cases respectively.*

The force jump Δf between two states at the coexistence force is $\Delta f = \epsilon_{eff}(f_c)\Delta x$, where Δx is the molecular extension and the effective stiffness ϵ_{eff} of the system is:

$$1/\epsilon_{eff}(f) = (1/\epsilon_b) + (1/\epsilon_x(f)) \tag{3.8}$$

where ϵ_b and ϵ_x are the rigidities of the trap and the molecular system attached to the bead (handles+hairpin) respectively. According to the definition of SNR [1] and using the Eq.xxx, the SNR can be measured by the following expression:

$$SNR_f = \epsilon_x \Delta x/(k_B T(\epsilon_x + \epsilon_b)^{1/2}) \tag{3.9}$$

To analyze the elasticity of short and long handles from our high bandwidth measurements, the effective stiffness $\epsilon_{eff}(f)$ (defined by $\epsilon_{eff}(f) = \Delta f/\Delta x$) for the 2S hairpin in a range of forces from 1 pN up to the coexistence force $\cong$ 15pN has been measured. The value of ϵ_{eff} has been measured over that range of forces by determining the derivative $\Delta f/\Delta x$ where Δf=1pN

---

[1] The signal-to-noise ratio (SNR) is defined by the ratio between the jump in force in PM or in CFM in folding/unfolding transitions and the standard deviation of the signal. If s corresponds to a generic signal (force in PM and extension in CFM) then $SNR = \Delta s/\sigma_s$ where Δs is the jump in the signal and σ_s is the standard deviation. For determination of σ_s the relevant forces have been collected using a high rate Data Acquisition Board (around 2-3 kHz). SNR measurements were done under PM conditions because in CFM experiments the force feedback control operates at a frequency much lower than the corner frequency of the bead.

and Δx is the corresponding trap displacement. The values of the effective rigidities decrease for long handles (Fig.3.4). By combining the equations 3.5, 3.6 and 3.7 is possible to solve them at each value of the force and determine ϵ_x and ϵ_b as a function of force:

$$\epsilon_b = \epsilon_{eff} + (\langle \delta f^2 \rangle / k_B T) \tag{3.10}$$

$$\epsilon_x = ((\epsilon_{eff} k_B T) + (\langle \delta f^2 \rangle)(\epsilon_{eff} / \langle \delta f^2 \rangle) \tag{3.11}$$

The results are shown in Fig.3.4. This work has presented a novel method to extract accurate information about the elastic properties of the molecular setup based on high bandwidth measurements of force fluctuations. This method of analysis has two main applications: it can be used to determine the stiffness of the trap and at the same time can be used to extract information about the elastic properties of polymers.

Single molecule stochastic resonance *Kumiko.et.al [50] used the Stochastic resonance (SR) to investigate the folding and unfolding kinetics of DNA hairpins in a bistable free-energy potential. The SR is a phenomenon where a signal, which is too weak to be detected, can be amplified by adding white noise which contains a wide spectrum of frequencies to the signal. The frequencies in the white noise corresponding to the original signal's frequencies will be amplified while the rest of the frequencies in the white noise will remain unchanged. In this work the first experimental study of SR in single DNA hairpins under the action of an oscillating mechanical force applied with OT is carried out. When an applied force oscillates close to the average unfolding force, the hopping kinetics between the folded and the unfolded states synchronizes with the frequency of the applied force. This experiment allows us to calculate the SR by recording the oscillations produced in the molecular extension relative to the magnitude of the thermal noise. The power spectral density of the molecular extension allow us to obtain details of the frequency dependence of the output signal, the background noise and the signal-to-noise ratio (SNR). A good evaluation of the SR can be made using the SNR of the spectral density measured in the fluctuations of the molecular extension in a hairpin of 20 bp which exhibits hopping between two states. A peak is produced in the frequency of the SNR power spectral density corresponding to the frequency value given by the resonance condition. After that the research have explored how several parameters of the experimental setup such as the size of the hairpin, the length of the handles, the stiffness of the trap and the force oscillating amplitude influence the resonance behavior in the experiment. In this work a systematic study of SR in hairpins of 20 bp, 10 bp and 8 bp as a useful tool to determine the kinetic properties of the biomolecules has been performed. These kinds of experiments in short hairpins show how SR might be useful for the detection of conformational transitions of low SNR.*

Experimental setup and hopping experiments

The recent advances in single-molecule techniques make possible the measurement of SR at the level of individual molecules. Biomolecules show rough and complex free-energy landscapes that determine molecular folding kinetics and influence the way the molecules fold into their native structures. By applying a mechanical force on an individual molecule and then recording the time evolution of the molecular extension, it is possible to obtain information about the folding reaction and the thermodynamics and kinetics of the molecule can be determined.

In these kinds of experiments the oscillation frequency of an applied force on the molecule might be ideal for studying SR in biomolecules. SR appears as a maximum in the response of a biomolecule at a characteristic frequency (called the *resonance frequency*). When an applied force oscillates around the average unfolding force, thermally activated hopping kinetics between the folded (F) and unfolded (U) states synchronize with the frequency of the external driving force, leading to SR. SR can be measured by recording the oscillations produced in the molecular extension relative to the magnitude of the thermal noise. In Fig.3.5 the experimental setup, the DNA sequence of hairpin H1 and the detection of the SR in experiments with OT is shown.

Around a particular force called the coexistence force, $f_c \cong 14.5pN$, the hairpin hops between the F and U states populating them with equal probability. As it has been explained in Forns. et al [44], the hopping experiments can be performed in two different modes: Constant Force Mode (CFM) where the force applied to the molecule is maintained at a preset value by moving the optical trap through force-feedback control (Fig. 3.5.B). By following the nomenclature of this work, $X(t)$ is the recording the trap position during the folding and unfolding transitions of the DNA hairpin. The second mode is called Passive mode (PM). In PM the position of the optical trap is maintained stationary without any feedback. The bead moves in the trap in response to changes in the extension of the DNA hairpin (Fig. 3.5.B). Both hopping and the oscillation experiments have been carried out using CFM, by recording the position of the trap, $X(t)$. From $X(t)$ it is possible to extract the residence-time distribution at each state that shows the exponential form shown in Fig.3.5.C. The fit of the the time distribution to an exponential function allows us to obtain the average residence-time. The kinetic rates (k_c=$k_{FU}(f_c)$=$k_{UF}(f_c)$=$1/\tau_c$) are measured at the coexistence force $f_c = 14.5 \pm 0.3$ pN giving around $k_c = 0.66 \pm 0.04$ s^{-1}.

SR Experiments

To induce the SR phenomenon, an oscillating force $f(t)$ is applied to the hairpin using the force-feedback protocol, where $f(t) = f_c + f_{OS}(t)$. For $f_{OS}(t)$ have been chosen a square-wave signal of amplitude A and frequency $\nu_{OS} = 1/T_{OS}$, where T_{OS} is the period of oscillation (Fig.3.5.D). The four levels of extension observed in Fig.3.5.D middle correspond to the molecular extensions in the F and U states at the two force values, $f = f_c + A$ and $f = f_c - A$. The power spectral density is defined as the Fourier transform of the correlation function of the signal $X(t)$:

$$S(\nu) = \int_{\inf}^{+\inf} \langle X(t)X(0)\rangle \, exp^{-i2\pi\nu t} dt \tag{3.12}$$

where $\langle\rangle$ denotes a time average over the signal. To extract the signal from the background noise, it is defined the output signal (OS), the background noise (BN) and the signal-to-noise ratio (SNR) as:

$$OS = lim_{\Delta\nu\to 0} \int_{\nu_{OS}-\Delta\nu}^{\nu_{OS}+\Delta\nu} S(\nu) d\nu \tag{3.13}$$

$$BN = S_N(\nu_{OS}) \tag{3.14}$$

$$SNR = \frac{OS}{BN} = \frac{1}{S_N(\nu_{OS})} lim_{\Delta\nu\to 0} \int_{\nu_{OS}-\Delta\nu}^{\nu_{OS}+\Delta\nu} S(\nu) d\nu \tag{3.15}$$

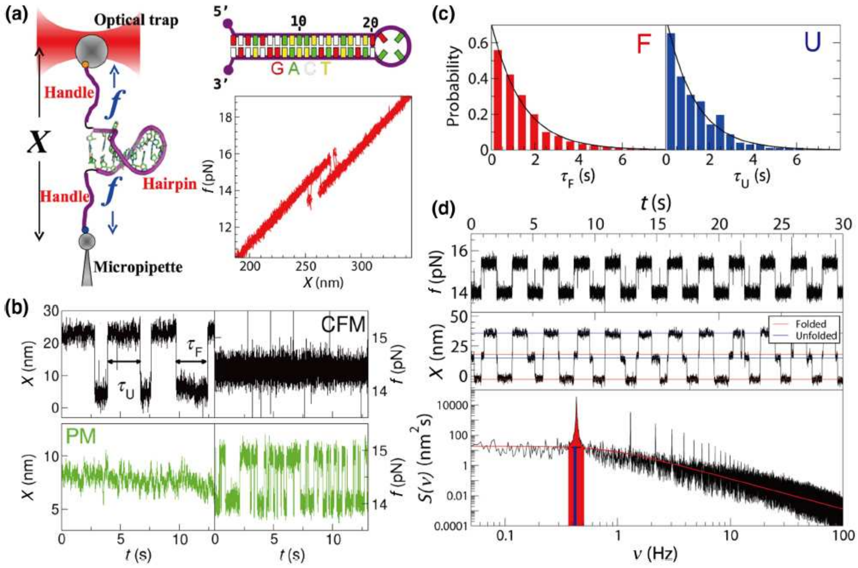

Figure 3.5: *Figure taken from [50]. Experimental setup, hopping and SR experiments. (a) Illustration of the experimental system, DNA sequence of the two-state hairpin H1 (upper right, sequence shown in color code), and experimental force-distance curve for H1 obtained from a pulling experiment (lower right). (b) Typical force and extension traces of the hopping experiments for H1 obtained in CFM (upper) and PM (lower). (c) Probability distributions of the residence times for H1 in the F (red) and U (blue) states obtained from the hopping experiments at* $f = f_c \cong 14.5pN$ *in the CFM. The black curves show the exponential fit,* $(1/a)exp(-\tau/a)$*, to the data, with a=1.42 s (a=1.34 s) for the F (U) state,respectively. (d)Typical force and extension traces (upper and middle) obtained by applying an oscillating-force protocol with amplitude A=0.7 pN and frequency* $\nu_{OS} = 0.4Hz$ *around the coexistence force* $f_c = 14.5\ pN$*. In the lower panel, we show the measured power spectrum,* $S(\nu)$*, calculated by fast Fourier transform of* $X(t)$ *with window size* $N = 2^{17}$ *shown in the middle panel. The sampling rate of the instrument is 1 kHz. The red area is the output signal and the vertical blue bar represents the background noise.*

Fig.3.5.D illustrates how the OS (red area) and the BN (blue area) from the spectral density has been measured. Both indicators, OS and SNR are equally valid for identifying resonant behavior, even though the peak is often more visible in SNR.

For the hairpin H1 at high trap power and trap stiffness ($\kappa_{trap} \cong 70pN/m$), the resulting OS and BN as a function of ν_{OS} are depicted in Fig.3.6.A and Fig.3.6.C showing the SNR. In contrast to the OS, there is a presence of a peak around $\nu_{OS} = 0.4 \pm 0.05$ Hz.

The OS and SNR can be calculated as a function of the oscillation frequency for a Brownian particle in a continuous double-well potential. In this theoretical mode, the OS and the SNR exhibit a soft and a sharp peak, only when SR is induced at large enough forcing amplitude. These large forcing amplitudes correspond to a nonlinear regime of the system in which the shape of the double-well potential is so deformed that the barrier separating the wells vanish at the maximum of the oscillation. In the experiments carried out in this work a large amplitude of 0.7 pN has been applied. Fig. 3.5.A shows that the region of the coexistence force between the F and U states spans less that 3 pN. An extra force of 0.7 pN strongly alters the barrier and the relative free energy between states.

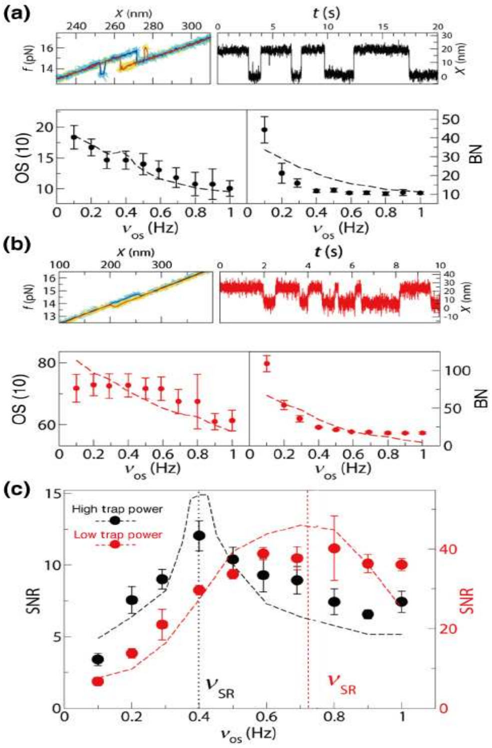

Figure 3.6: *Figure taken from [50]. SR experiments for hairpin H1 at different trap stiffness. (a) Pulling cycle (unfolding in blue and refolding in red), hopping trace, OS and BN for H1 with amplitude A=0.7 pN at high trap stiffness, $k_{trap} = 70$ pN/μm. (b) the same experiments at low trap stiffness, $k_{trap} = 24$ pN/μm. Results have been averaged over 5-10 molecules. (c) SNR at high trap stiffness (low trap power) depicted in black (red). Units OS (nm^2), BN (nm^2/Hz) and SNR (Hz). Simulation results are shown as dashed lines. The error bars represent the standard error over different molecules.*

In order to see what happens for lower oscillation amplitudes, the response of hairpin H1 to an oscillating force of a lower amplitude (0.2 pN) has been explored. A very soft peak can be seen around 0.4 Hz in agreement with the results obtained for the higher amplitudes, A=0.7 pN. However the peak for A=0.2 pN is much less clear than the peak for A=0.7 pN showing the importance of using oscillation amplitudes beyond the linear-response regime.

Influence of trap stiffness and length of the handles

As it has been explained in Forns. et al, the experimental setup, such as the trap stiffness or the length of the handles plays an important role in kinetic measurements on single-molecule experiments. For this reason experiments were conducting using various experimental setup conditions. By varying the conditions we observed that these effects change the intrinsic noise of the system.

When the trap stiffness (κ_{trap}) decrease from 70 pN/μm to 24 pN/μm, the peak in the SNR is shifted to higher frequencies and becomes less clear.

Likewise if the handles length is increased (from 29 bp to 580 bp) while the trap stiffness is constant (κ_{trap}=70 pN/μ m), it is found that the resonance frequency shifts to a larger value for the long handles (Fig 3.7).

In both cases, the soft-trap stiffness or the long handles contribute to increased hopping rates as it possible to see in Fig.3.6 and Fig.3.7.

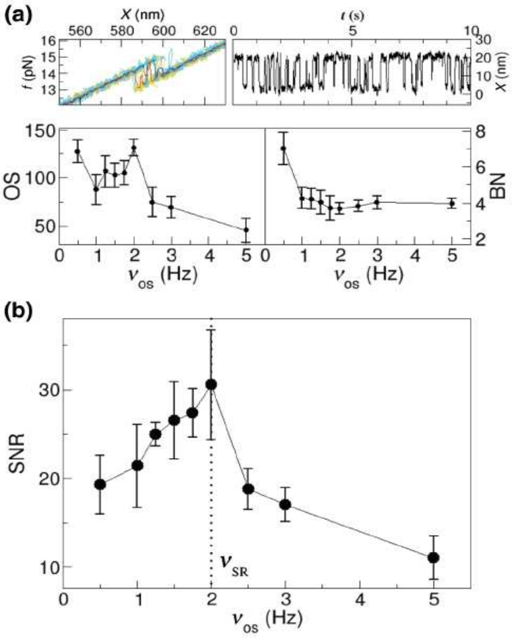

Figure 3.7: *Figure taken from [50]. SR experiments for hairpin H1 with long DNA handles. (a) Upper left: cycle (unfolding, blue: refolding, red). The dark blue and red curves are the time-averaged data of the paler blue and yellow lines. Upper right: hopping trace. Lower left:OS. Lower left: BN.* (b) The resulting SNR in the case of high trap stiffness, k_{trap}=70 pN/μ m and the amplitude A=0.7 pN. Results have been averaged over 5 molecules.Units OS (nm^2), BN (nm^2/Hz) and SNR (Hz). The error bars represent the standard error over different molecules.

SR in shorter hairpins

Another application of SR phenomenon is the detection of the transitions between F and U states in cases where the hopping events of a hairpin are hard to detect. In this case the hopping signals are on the same order as the standard deviation of noise fluctuations. To investigate this question two short hairpins (SH10 and SH8) have been designed. SH10 has 10 bp and SH8 has 8 bp along the stem (Fig. 3.8). The free-energy landscapes are calculated for the two sequences at the theoretically predicted coexistence force. As the length of the stem decreases, the landscapes show lower coexistence force values, molecular extensions and kinetic barriers. Measurements for SH10 and SH8 are taken at low trap stiffness to decrease the hopping signal (k_{trap}=32 pN/μ m and k_{trap}=17 pN/μ m). As it is possible to see in Fig.3.8.A, while the transitions are visible for SH10, they are hardly distinguishable for SH8. Measured jumps in the molecular extension upon unfolding or folding are equal to 10.5 ±0.5 nm and 7.0 ± 0.5 nm for SH10 and SH8.

The power spectra of SH10 can be fit to a sum of two Lorentzian with two corner frequencies of 0.64 ± 0.02 Hz and 2.4 ± 0.3 kHz. However the quality of the power spectrum is worse for SH8 (9.8 Hz and 15.6 kHz). The low frequency in the power spectrum of SH8 corresponds to the hopping kinetics of the hairpin, the higher frequency corresponds to the random motion of the optical trap caused by the force feedback. Once the hopping properties of the hairpins are characterized, then the oscillating experiments for SH10 and SH8 around the coexistence force are carried out. For SH10 the peak in the SNR around ν_{SR}=0.5Hz is close to $k_c/2$ where k_c is measured to be 0.43 ± 0.07 s^{-1} from the hopping traces for $X(t)$.

However in the case of hairpin SH8, the coexistence force can still be located, but the hopping signal is not clear from the fluctuations. The OS and SNR exhibit a maximum around ν_{SR}=5 ± 1Hz, which gives k_c=10 ± $2s^{-}1$. This value agrees with the value of 9.8 Hz obtained from the Lorentzian fit to the power spectrum.

SR offers an alternative of estimating the hopping rate of SH8. The two states (F and U) can not be easily detected from the hopping trace. In this case, SR confirms the value of the hopping frequency initially obtained from the Lorentzian fit of the power spectrum.

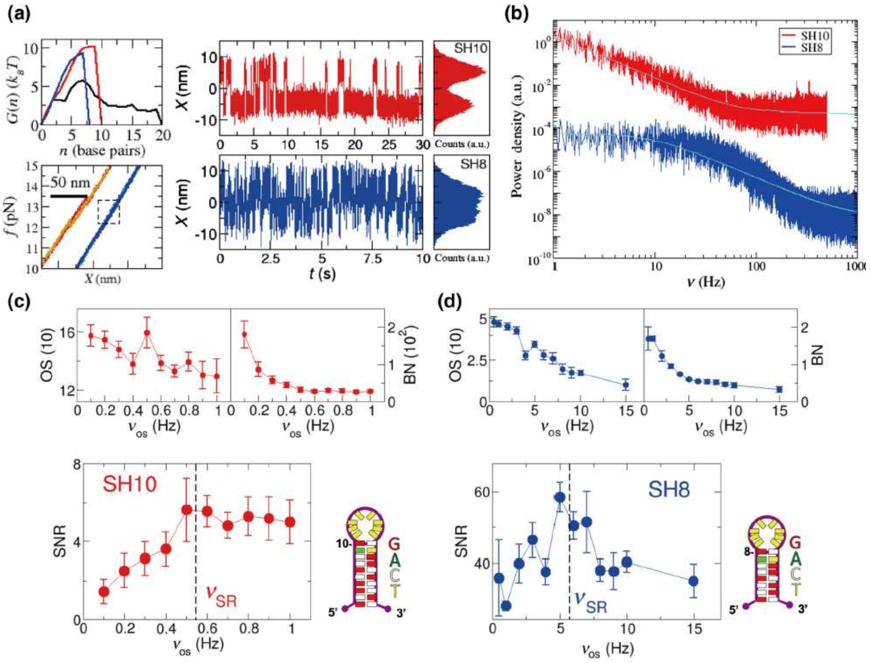

Figure 3.8: *Figure taken from [50]. SR experiments in shorter hairpins. (a) Free energy landscapes (upper left), force-distance curves (lower left) and hopping traces in the CFM for SH10 (red), SH8 (blue) an H1 (black). Measurements have been carried out with a low trap power* k_{trap}*=32 pN/µm for SH10 and* k_{trap}*=17 pN/µm for SH8. For simplicity, all pulling curves in the lower left panel are shown parallel with equal average slopes. The dashed square region for SH8 curves indicates the region where unfolding and folding transitions occur. Distributions of trap position, X, show clear transitions for SH10 but not for SH8. (b) Power spectrum for SH10 and SH8. Cyan curves are fits to a sum of two Lorentzians. Colors mean the same as in (a),(c). (d) OS, BN and SNR for SH10 and SH8. The amplitudes of oscillation force are A=0.5 pN for SH10 and A=0.15 pN for SH8. Colors mean the same as in (a). Statistics (SH10,SH8): molecules (5,7); duration of hopping traces (4,2 minutes); average number of hopping transitions (250,1200) at each input frequency. Units OS (nm*^{2}*), BN (nm*^{2}*/Hz) and SNR (Hz). The error bars represent the standard error over different molecules.*

Measurement of work in single-molecule pulling experiments [51]. *A main goal of single molecule experiments is to evaluate equilibrium free energy differences by applying fluctuation relations to repeated work measurements along irreversible processes. Mossa.et al, quantify the error that is made in a free energy estimate by means of Jarzynski equality when the accumulated work expended on the whole system (including the instrument) is erroneously replaced by the work transferred to the subsystem consisting of the sole molecular construct. It is found that the error depends on the number of experiments and on the bandwidth of the data acquisition apparatus.*

One method to study the folding of biomolecules is the so-called pulling experiment (Fig.3.9). This method allows us to repeatedly measure the folding-unfolding transitions of the molecule using different speeds of pulling. In this way the force versus extension trace shows two paths: the forward path (F → U) and the reverse path (U → F)(Fig.3.10). By using fluctuations theorem, such as the Jarzynski equality [82] it is possible to recover free energy differences between U state and F state . The Jarzynski equality relates the work along the nonequilibrium trajectories with the equilibrium free energy difference.

$$\Delta G = -k_B T log \left\langle exp(\frac{-W}{k_B T}) \right\rangle \tag{3.16}$$

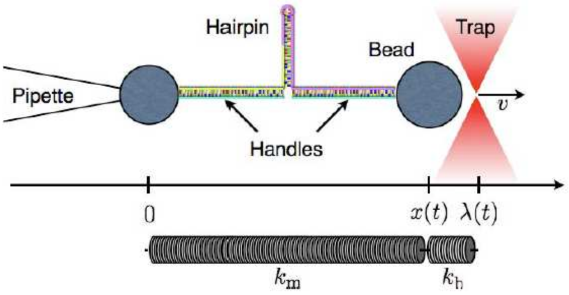

Figure 3.9: *Figure taken from [51]. Schematic definition of the model under study. The pipette is at rest with respect to the thermal bath, while the trap is moving with velocity v. The trap and the system: molecule + handles are approximated by two harmonic potentials with stiffness k_b and k_m.*

The expression in the angle brackets (⟨ ..) is averaged over an infinite number of trajectories realized using the same experimental protocol. The free energy difference (ΔG) depends on two parameters: the control parameter λ and a state parameter s. The control parameter is the distance between the trap and the pipette and we can be experimentally controlled. However, s is the state of the system, which for short molecules is either U of F. This parameter is not directly manipulated by the experiments. In our case, we consider two paths forward process (F → U) and the reverse process (U → F). The ΔG is given by:

$$\Delta G = G(\lambda_1, U) - G(\lambda_0, F) \tag{3.17}$$

where G(λ_1,U) corresponds to the free energy of the unfolded state at λ=$\lambda_1$and G(λ_0,F) corresponds to the free energy of the folded state at λ=λ_0

How can we measure the work in a single molecule experiment? The work is given by:

$$W = \int_{\lambda_0}^{\lambda_1} f d\lambda \tag{3.18}$$

where λ_0 and λ_1 are the initial and final distance and f is the force exerted upon the molecule. In other words, in our experiments W is the area below the force versus extension curve (Fig.3.10.A).

What advantages can we obtain with a high acquisition rate in this system? There are certain experimental settings where the control parameter λ is not directly measured [83] and its more practical to use the molecular extension x. In this case the transfer work is given by (Fig.3.10):

$$W' = \int_{x_0}^{x_f} f dx \tag{3.19}$$

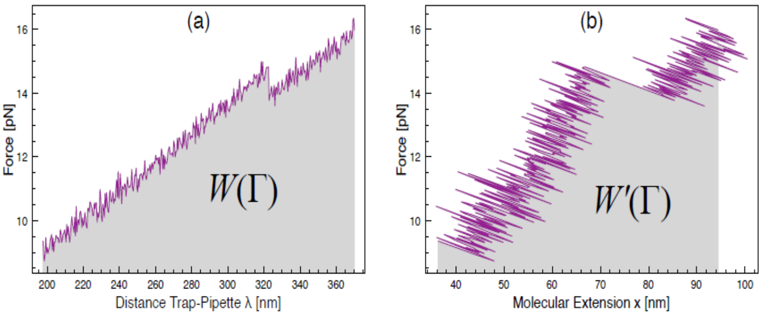

Figure 3.10: *Figure taken from [51]. (a) A typical force-distance curve (FDC). The shaded area is equivalent to the accumulated work $W(\Gamma)$ (eq.3.18). (b) The force-extension curve (FEC) associated to the pulling experiment represented in Fig.3.10.a. The shaded area is equivalent to the transferred work $W'(\Gamma)$ (eq.19).*

It is known that to use W' in the last equation is a source of error, but so far nobody has experimentally measured how small it is. The area under the curve is the work W' transferred to the molecule subsystem, while the latter curve allows the measurement of the accumulated work W, the total amount of work expended on the whole system (experimental apparatus included).

We call ΔG' the incorrect value of ΔG which is given by applying the last equation:

$$\Delta G' = -k_B T log \left\langle exp(-\frac{W'}{k_B T}) \right\rangle \tag{3.20}$$

The difference between ΔG and ΔG' depends on the number of experiments and on the amplitude of force fluctuations. This work quantified how large an error is to affect the estimation of the free energy at zero force ΔG' of the molecule if W is erroneously replaced with W' (Fig.3.11).

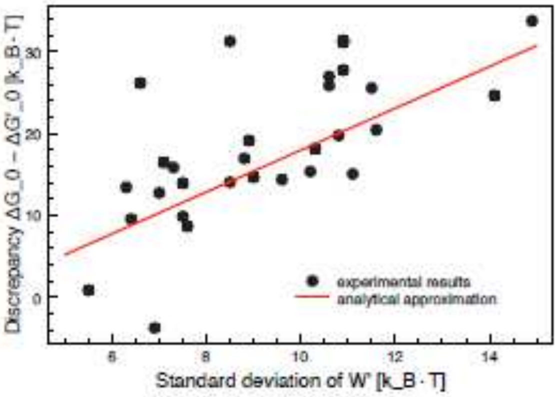

Figure 3.11: *Figure taken from [51]. Experimental test. In abscissa,* s' *is the standard deviation of the transferred work values* W_i'*; different values of* s' *are obtained by varying the stiffness of the trap and the bandwidth. In ordinate, it is represented the error (due to the erroneous use of* W' *in the Jarzynskin estimator)* $\Delta G_0 - \Delta G_0'$ *(in* $k_B T$ *units) on the determination of the free energy of formation of the hairpin.*

Chapter 4

Methodology

Over the past two decades optical trapping has provided a new technique to work in biophysics by manipulating individual objects, from microscopic particles to nanoparticles, from living cells to single molecules. In this chapter (Section 4.1) we review the theory of optical trapping and how the OT measures force by determining the change in light momentum. In section 4.2 of this chapter the miniTweezers (mT) setup is described in detail. In section 4.3 the methods used to calibrate the force and the distance in this setup are described. In section 4.4 we present the novel setup of the TC in the mT instrument. This TC system has been developed as an improvement on the original mT setup. This section describes the modifications made to the mT to implement the TC system and the methodology used to carry out single molecule experiments in a wide range of temperature. Section 4.5 describes the tests carried out to characterize the size of the heating laser beam spot, the measurement of the adsorption coefficient and various tests carried out to ensure that the TC system works correctly. Finally the synthesis of the DNA molecule under study and the unzipping experiments are described in section 4.6.

4.1 Theory of Optical trapping

4.1.1 Physical principles

In 1873 James.C.Maxwell theorized that photons can exert a force as it described in his equations of electromagnetism [52]. This effect is known as radiation pressure. However this was not demonstrated experimentally until 1970 when the development of lasers allowed the study of the radiation pressure on an object. Experiments on radiation pressure using lasers were performed by Arthur Ashkin in the early 70s at ATT Bell Telephone Laboratories [53]. He observed that objects of high refractive index were drawn towards the center of an unfocused laser beam, and pushed in the direction of propagation.

Radiation pressure is produced by the interaction between light and matter. By controlling the radiation pressure it is possible to apply forces on microscopic particles. The force exerted by photons on a particle depends on the index of refraction of the particle. Particles can be classified as dielectric or metallic. It has been demonstrated that dielectric particles are more attracted to the regions of maximum light intensity. However the metallic particles can be attracted to or repelled from the high intensity spot of light.

To understand the basis of optical trapping consider a ray of light that falls on a dielectric sphere as shown in Fig.4.1. Due to the diffraction of the light ray by the dielectric particle, the momentum of the outcoming ray changes. The change in the momentum experienced by each photon is transferred to the sphere, generating force $\vec{F}$ on the particle. The trapped object feels a force which is equal but opposite to the change of momentum $\Delta\vec{p}$. This force is the result of reflections and refractions of the incident rays on the particle.

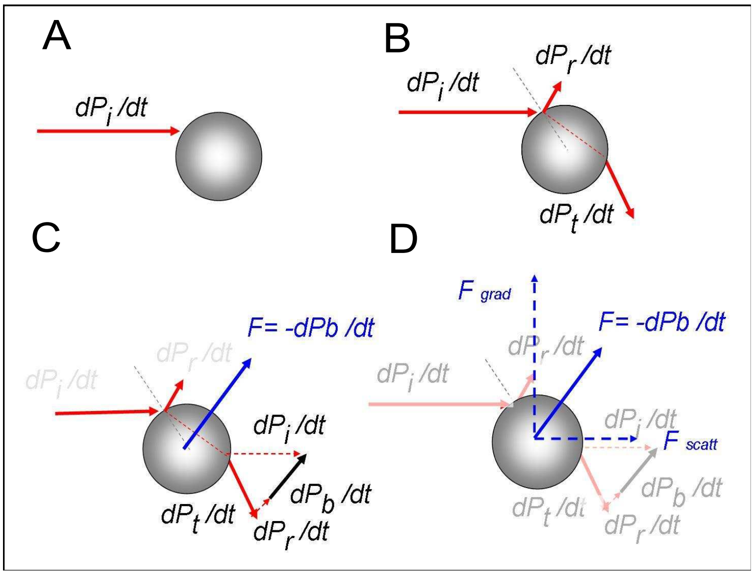

Figure 4.1: *Optical forces on a dielectric sphere: A. One incident (i) ray falls on the dielectric particle (incoming ray). B. Due to the diffraction of the light ray by the dielectric particle the momentum of the outcoming ray changes. Part of the light is reflected (r), part is transmitted (t) on the particle. C. The linear momentum ($d\vec{p}_i/dt$, $d\vec{p}_t/dt$, $d\vec{p}_r/dt$) is transferred to the bead ($d\vec{p}_b/dt$) and the trapped object induces a force which is equal but opposite to the change of momentum ($\vec{f}$=$d\vec{p}_b/dt$). D. The total force on the bead is divided in two components: the scattering (F_{scatt}) and the gradient (F_{grad}) forces.*

The linear momentum of the incident light $\vec{p}_i$ is divided into components: the reflected and the transmitted ray, each one inducing a different quantity of linear momentum ($\vec{p}_r$ and $\vec{p}_t$). The balance between them is the resulting linear momentum transferred to the bead $\vec{p}_b$. This linear momentum is expressed as:

$$\vec{p}_i = \vec{p}_r + \vec{p}_t + \vec{p}_b \tag{4.1}$$

$$\vec{p}_b = \vec{p}_i - (\vec{p}_t + \vec{p}_r) \tag{4.2}$$

The force applied to the bead corresponds to the amount of $\vec{p}_b$ transferred per unit of time:

$$\vec{f}_b = \frac{d\,\vec{p}_b}{dt} \tag{4.3}$$

The reflected component is negligible in comparison with the transmitted ray. Then the transmitted ray can then be split into two perpendicular components: the scattering and gradient forces (Fig.4.2.A).

- *The scattering force*: The photons running into the particle will push the particle in the direction of light propagation. The resulting force will have the same direction as the photons flux.

- *The gradient force:* This force arises from the region of maximum intensity of light. In the plane perpendicular to the beam, the intensity profile of the laser has a Gaussian shape. This pulls the particle towards the regions of highest light intensity.

In order to create a stable optical trap, Ashkin developed a system of two counter propagating beams along the same optical path which created a three dimensional trapping beam [53]. However he later developed a more dimensionally stable optical trap by using a laser and a microscope objective lens [26] (Fig.4.2.B). By focusing a laser beam though the objective lens a focal region of maximum intensity was generated and a single beam gradient force optical trap was created. Stable trapping requires that the axial gradient force dominates versus the scattering force. For this reason OT are usually constructed using microscope objective lenses whose high N.A and well corrected aberrations focus light as tightly as possible.

There are three theories developed to describe the mechanical force of radiation pressure of light on a spherical particle. These three theories depend on the ratio between the wavelength of the light (λ) and the size of the particle (d). The *ray optics* or Mie theory describes the dispersion of light by small particles when d>>λ. The opposite theory is when d<<λ. This is known as the Rayleigh theory. However, most of the work done with optical tweezers uses the intermediate theory where d is comparable to λ. The calculation of optical forces when using this theory requires the full solution of Maxwell's equation.

4.1.2 Optical tweezers as a force transducer

As described by Ashkin [53]: *"In a laser-light there are stable optical potential wells in which particles were trapped by radiation pressure alone."*

It has been experimentally demonstrated by several authors [54, 61, 38] that the optical trap can be characterized by an *harmonic potential* which follows Hooke's Law: $F = \kappa \Delta x$ (Fig.4.3) where κ is the stiffness of the trap and where the forces acting on the bead are directly proportional to the distance between the bead and the center of the trap. As a consequence of the simple relationship observed between displacement x and restoring force F, an optical tweezers can be used as a force transducer. This method is useful and allows measurement of subnanometric distances and forces around 1-100pN on a particle in a trap. Once the trap stiffness α is calibrated, the force measurements are reduced to a position measurement.

The displacement of the particle in an optical trap is linear in a wide range of forces [54], however there are some difficulties with the calibration of the stiffness of the trap as explained by Smith.et.al [56, 57]. For example the calibration of the α could be determined by using methods such as Stoke's law or the analysis of Brownian motion. However, these calibration methods require knowledge of the size of the particle and the viscosity of the medium (Section 4.3)

A major improvement in the optical tweezers setup was the development of a system of two counter-propagating beams [56]. This system consists of two counter propagating laser beams which share the same focal point and optical path. The advantage of this setup is that the trap

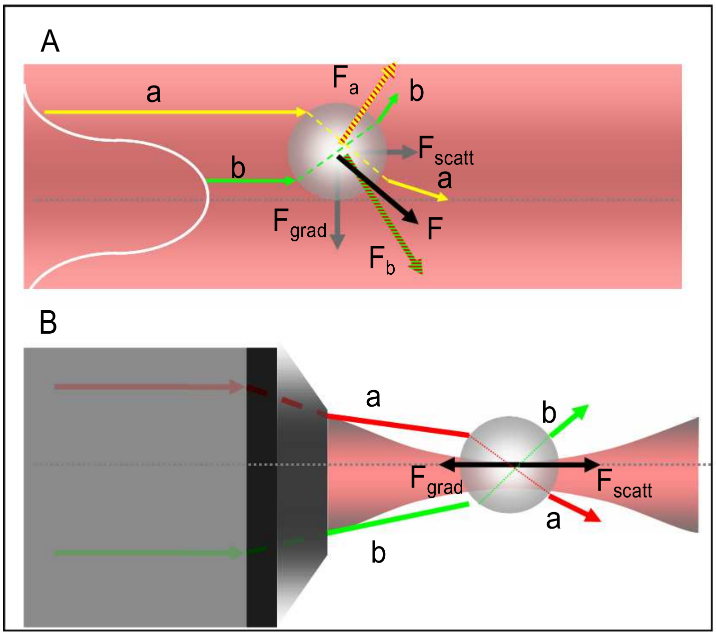

Figure 4.2: *A. A depiction of the scattering force (F_{scatt}) and the gradient force (F_{grad}) components of the optical force on a sphere due to a Gaussian laser beam. The scattering force pushes the particle in the direction of the light. The gradient force pulls the particle towards the beam axis. B. A focused Gaussian beam creates a strong intensity gradient along the propagation direction of the beam. Axial stability is obtained thanks to the gradient force that prevents the sphere from being pushed away by the scattering force.*

stability is improved because the scattering forces of both lasers cancel with each other and it is not necessary for the lasers to work at high power in order to achieve 100 pN of force on the particle in the trap. In fact in single beam optical traps the lasers would have to use several Watts of power in order to produce 100 pN of force on the particle in the trap whereas with the counter-propagating system the same 100 pN of force can be produced using less that 100 mW of laser energy. This is a vast improvement which greatly reduces the potential for damage from laser radiation to the biomolecule or cells being studying in the trap. However the most important improvement in this setup is that the calibration of force can be obtained using the principle of conservation of the linear momentum.

4.1.3 Calibration of force by the conservation of linear momentum

A new method of calibrating the force independently of the size of the bead or the viscosity of the medium was developed by Smith.et.al in 2003 [56]. This method consists of measuring the change in the momentum flux of the photons when they interact with the surface of the particle. The change in the momentum flux of the photons between entering and leaving the optical trap is equal to the force applied to the particle [56].

To measure the force by using this principle it is necessary that the force sensors collect all of the light that leaves the trap after interacting with the particle. The direction and intensity of the light are then analyzed to extract the components (x,y,z) of the light momentum. As shown in Fig.4.4, when an external force pushes the particle, light is deflected and leaves the optical trap with an angular distribution different to that when it entered the trap. In order to collect all the light leaving the trap, another microscope objective lens with a high N.A. is used. A

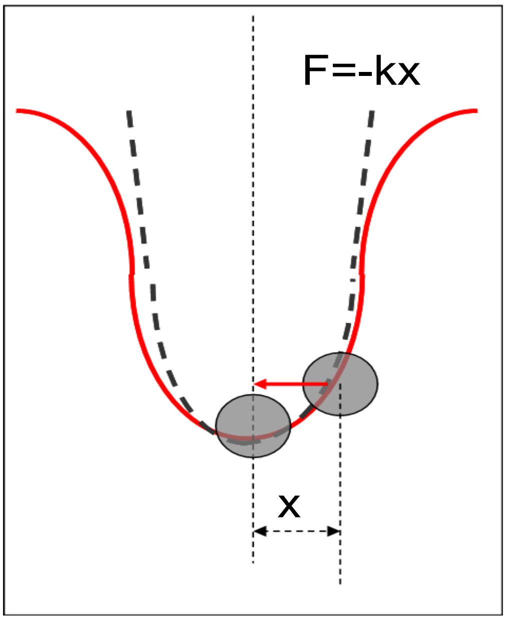

Figure 4.3: *Optical trapping potential experienced by a dielectric particle in a Gaussian beam. For small displacements* x*, the equilibrium position is restored by a Force given by* $F = -\kappa x$ *where* κ *is the stiffness of the optical trap.*

Position Sensitive Detector (PSD) is used to measure the position and power of the light leaving the trap.

The measurements of force are obtained using the signals of the deflected light that arrive at the PSD (D_x and D_y) as well as the following parameters: R_D radius of the area of the PSD, R_L focal length of the lens, c speed of light and Ψ power sensitivity of the PSD ($signal/watts$ referenced to the trap position).

$$F_x = \frac{D_x R_D}{c R_L \Psi} \tag{4.4}$$

$$F_y = \frac{D_y R_D}{c R_L \Psi} \tag{4.5}$$

The force exerted on the z axis can be measured by an attenuator (called a $bull's\ eye$) placed in front of a photodetector with a transmission profile (explained later in detail) [58]. The z force can be written as :

$$F_z = \frac{D_z n}{c \Psi} \tag{4.6}$$

By using this method the transverse force (x and y) of a trapped particle are independent of the particle's size or refractive index as well as the viscosity or refractive index of the solutions and the variations in laser power. This is because the factors R_D,R_L,Ψ are constant in a typical experimental setup.

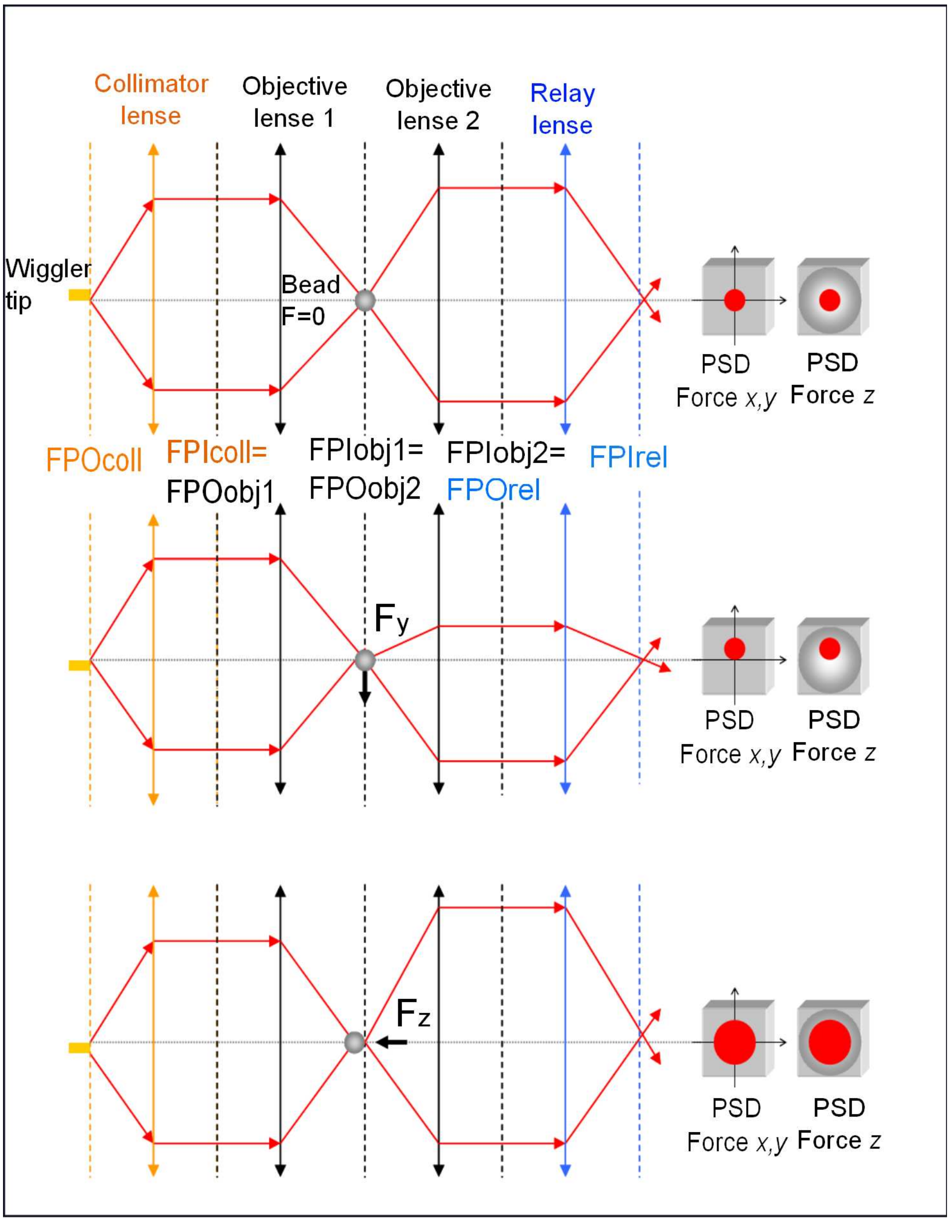

Figure 4.4: *Ray tracing of one of the trapping lasers. In this diagram the two Objective lenses, the collimator lens and the relay lens, are depicted. "Objective lens 1" correspond to the focuser and "Objective lens 2" corresponds to the condenser. To simplify the drawing, the objective lenses which are complex devices are shown as thin lenses. The light travels from the tip of the wiggler (end of the optical fiber) to the photodetectors (PSD). The discontinuous lines show the focal plane object (FPO) or focal plane image (FPI) of each lens. The FPI of the collimator lens coincides with the FPO of the focuser lens, this effect produces an infinite system (where the light beam is parallel), as well as the FPO of the condenser lens with the FPI of the relay lens.*

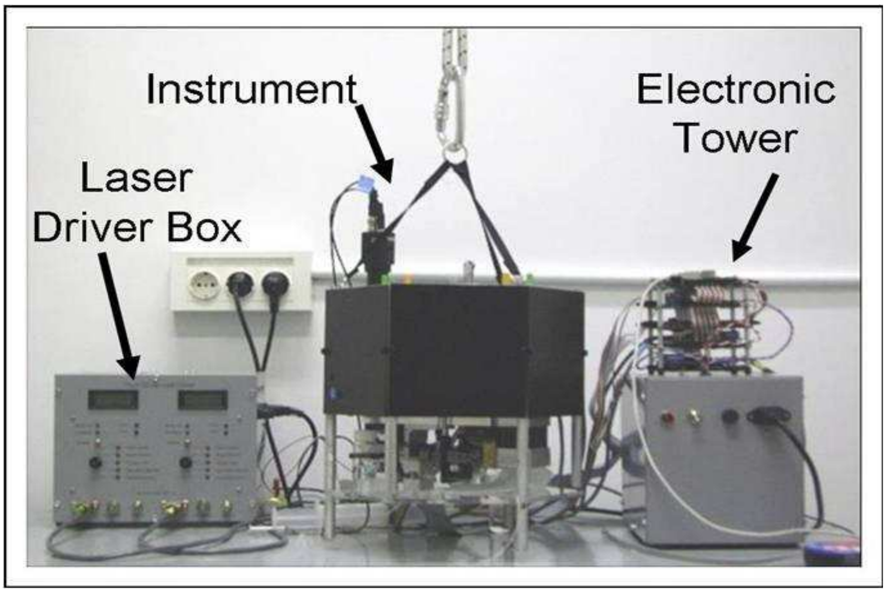

Figure 4.5: *Components of the mT instrument. The computer is not shown in this image.*

4.2 Minitweezers setup

Dr. Steven B. Smith has developed a new generation of optical tweezers instrument called miniTweezers (mT) [58, 59] (Fig.4.5). One of the biggest advantages of the mT setup is the use of two counter propagating beams to form a single optical trap in which the scattering forces cancel each other out. This improvement allows the use of reduced NA lasers. This combined with high NA objectives allows all of the deflected light exiting the trap to be collected thus permitting the use of the conservation of light momentum method of force calibration in the mT instrument. This system is a vast improvement over the single laser beam traps that use high NA objectives and lasers to reduce the scattering force effect on the object in the trap. In the single laser setup it is not possible for the objectives to collect all of the deflected light exiting the trap, thus making the use of the conservation of linear momentum method of force calibration impossible in this type of instrument.

The mT measures forces by the conservation of linear momentum. This allows a high stability and resolution. The miniaturized setup allows more precise force/distance measurements to be obtained while reducing the effect of floor vibrations, acoustic noise and room temperature changes.

4.2.1 The instrument head:

The principal part of the mT is the instrument head which contains the optical and the mechanical components of the setup. The instrument head weights around 10 kg. Its compactness allows it to be suspended from an extension spring to isolate it from building vibrations that could affect the experiments. The instrument head is composed of three levels (Fig.4.6.A). The top level where lasers and CCD camera are fixed. The second level can be divided in two: up side and down side. The up side contains the motor stage, the three motors and the PSD's of force and position. The down side contains the prism boxes and the optical rail with some of the optical components of the instrument such as the objective lenses and the quarter wave plates. The third level contains the fluidics system. Each of these levels are explained in greater detail below.

The instrument head is symmetric for each laser and each laser source generates one beam that is focused in the trap and travels through the same (but opposite) optical path (Fig.4.6.B). The instrument uses two counter propagating laser beams of 845nm (Lumics LU0845M150). Each laser diode produces an electromagnetic mode TEM00 with a Gaussian profile. The intensity and the temperature of each laser are controlled by a laser driver box (more information about the laser driver box at the end of this section). At the end of each laser diode there is a FC/PC connector which is connected to an optical fiber that transmits the light to a device called a *wiggler*.

The *wiggler* is a key innovation of the mT setup. There are two wigglers in the instrument one for each laser. This device allows the user to change and control the orientation and the position of the beams that forms the two traps and therefore to move the traps independently.

Each wiggler is constructed from two concentric brass tubes (Fig.4.7.A). The outer tube has a spherical enlargement which is connected to two piezoelectric actuators, one on the x axis and the other on the y axis. By moving the actuators, the spherical enlargement is moved thus moving the outer tube. Inside of the outer tube, the inner tube remains straight and in the center of the inner tube is located the optical fiber which transmits the light from the laser. The optical fiber is glued to the inner tube which acts as a pivot point. The optical fiber then passes though a pivot screen fixed to the end of the outer tube. By activating the piezoelectric actuators, the tip of fiber tilts thus changing the direction at which the light emerges. The range of displacement is around 10 μm for each axis.

The optical path of laser A and laser B are equal but opposite. Here we will describe the optical path of laser A. When the light leaves wiggler A it is split in two directions by a pellicle beam-splitter. Around a 92% is sent to the objective lenses to create the optical trap. The remaining light is directed to the position PSD's in order to measure the position of the beam.

After leaving the pellicle, the light that is directed to the objective lenses, arrives at the prism box-A. The prism box is a closed aluminum box which houses 2 Polarizing Beam Splitter (PBS), 3 lenses and 2 prisms. The light enters though a hole on the top of the box and is collimated by a f=20mm lens, polarized horizontally by PBS-1 and redirected out of the box though another hole on the side of the box (Fig.4.6.B).

Next the light arrives to a quarter wave plate which selects circular polarization and redirects the lights to the microscope objective lenses (Olympus UPLSAPO 60XW with N.A=1.2). The light is then focused by the objective lens to form the optical trap.

Light that exits the trap is then collected by using an identical but opposite objective lens and is converted to vertically polarized light by another quarter wave plate. The quarter wave plates ensure that the light of laser A does not interact with that of laser B and viceverse. Next the light arrives to prism box-B and enters though the hole on the side of the box. The light passes though PBS-1 and is redirected out of a hole on the top of the box by PBS-2. Next the light passes though a Relay lens and arrives to the force photodetector.

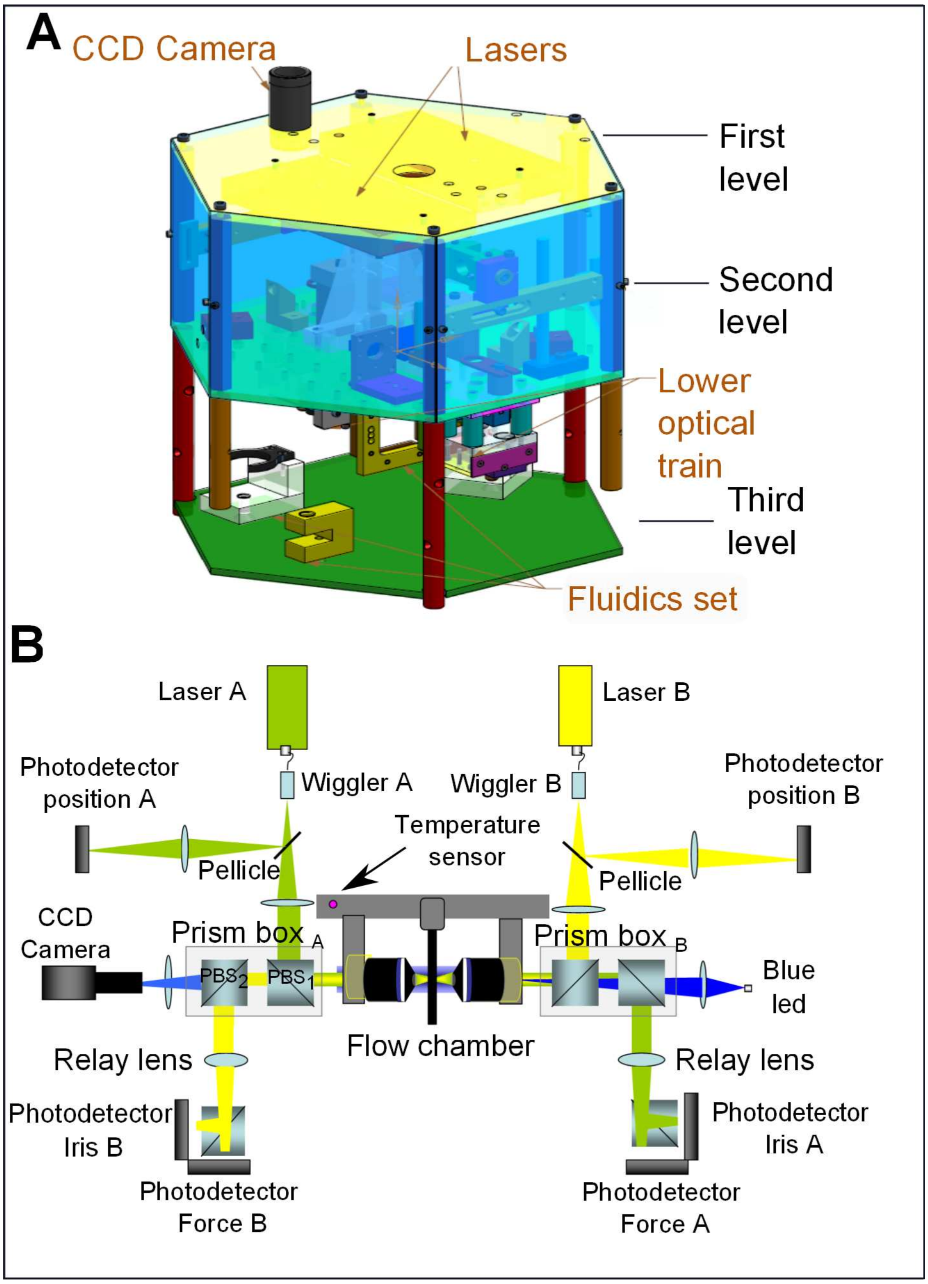

Figure 4.6: *Instrument head of the mT. A. This drawing shows the three levels of the instrument: 1) Lasers (not shown) and CCD Camera; 2) the second or intermediate level is divided into two parts: the up and the down sides. The instrument cover plates shown in transparent blue, enclose the inside of the instrument where are placed the x-y-z motors, the wigglers, the blue led and the PSD's of force and position; the down side creates the lower optical train created by the prism boxes, the quarter wave plates and the objective lenses; 3) the third level contains the fluidic set. (Drawing credit SEGAINVEX-UAM). B. Sketch of the optical setup used in the MT. The experiments are carried out in a microfluidics chamber specifically designed for use in the mT instrument (see Main text). The microfluidics chamber is placed between the two objective lenses.*

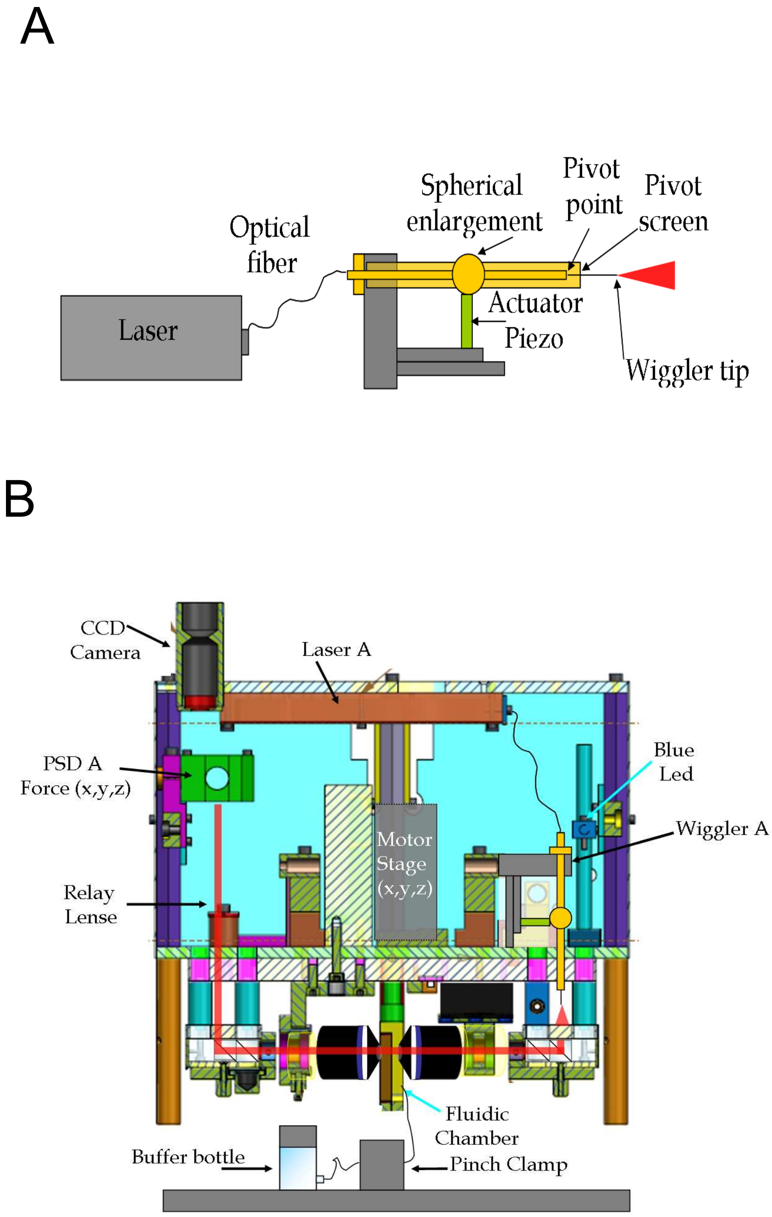

Figure 4.7: *A. The wiggler. The x,y actuator piezos push on the spherical enlargement producing the movement of the outer tube. The optical fiber is fixed in the pivot screen and the movement of the outer tube from the actuator piezo bends the fiber. The optical fiber remains fixed at the pivot point but the tip of the fiber (wiggler tip) can be bend and the laser beam directed by exerting pressure (through the piezo actuators) on the external brass tube (Only one piezo actuator is shown in the drawing). B. Optical path of one of the lasers viewed from inside of the instrument head. In this drawing the optical path from laser A to the force PSD is shown. As the instrument is symmetric then laser B follows the same path but in the opposite direction.*

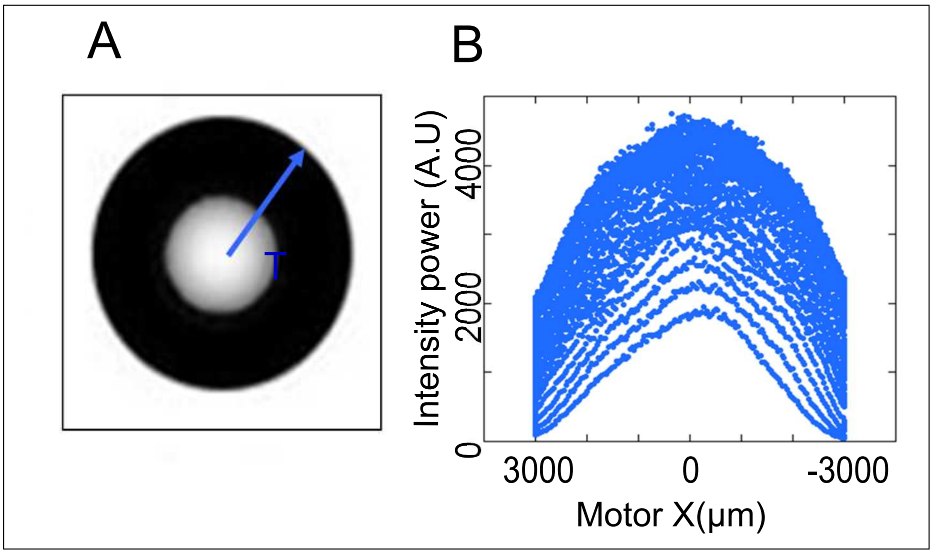

Figure 4.8: *A. Image of a Bullseye. The T shows an actual circular-profile transmission filter similar to Fig.4 in [58]. B. This figure is a raster scan of one such silter where the different X-scan lines are taken at different values of Y. The purpose of this scan was to check if the bullseye pattern was properly centered on the optic axis.*

This instrument measures the transverse and axial forces acting on the particle in the trap (F_x,F_y and F_z) using position sensitive detectors (PSDs). The PSDs are optoelectronic devices that provide an analog output current proportional to the position of the beam. There are six PSDs in the instrument, three for each laser. Each laser needs two PSDs to measure force and one to measure distance.

The force PSDs are located in a box designed specially for them. This box has one PBS which splits the beam in two parts. One part of the beam is directed to the PSD which measures F_x,F_y and the rest is directed to the PSD which measures F_z. The PSD which measures F_x and F_y measures light deflection to produce the values of D_x and D_y explained further in section 4.1.3. However to measure the axial force F_z a different kind of PSD is required which allows the measurement of the power concentration of the incident beam. To accomplish this an attenuator called a $bull's\ eye$ (Fig.4.8) is placed in front of the PSD. This attenuator has a transmission profile [58]. When the beam is axial to the PSD, 100% of the light is transmitted. However an off-axis beam suffers an attenuation reducing the intensity of the power to the PSD. This attenuator signal is known as IRIS. Observation of the IRIS value for each laser also indicates correct laser alignment.

To measure distances the instrument has two additional PSDs called *light-levers*. As mentioned before, about 8% of the light that leaves the wigglers is redirected to measure trap position. The light leaves the pellicle and is focused on the PSD though an aspherical lens.

One important improvement in the measurement of force and distance in the mT setup is that the optical trap and not the microfluidics chamber moves to apply forces to the trapped particle. This dramatically reduces drift effect in the experiments. Moreover the motorized stage makes it possible to easily move the microchamber to pick up beads or to calibrate distances.

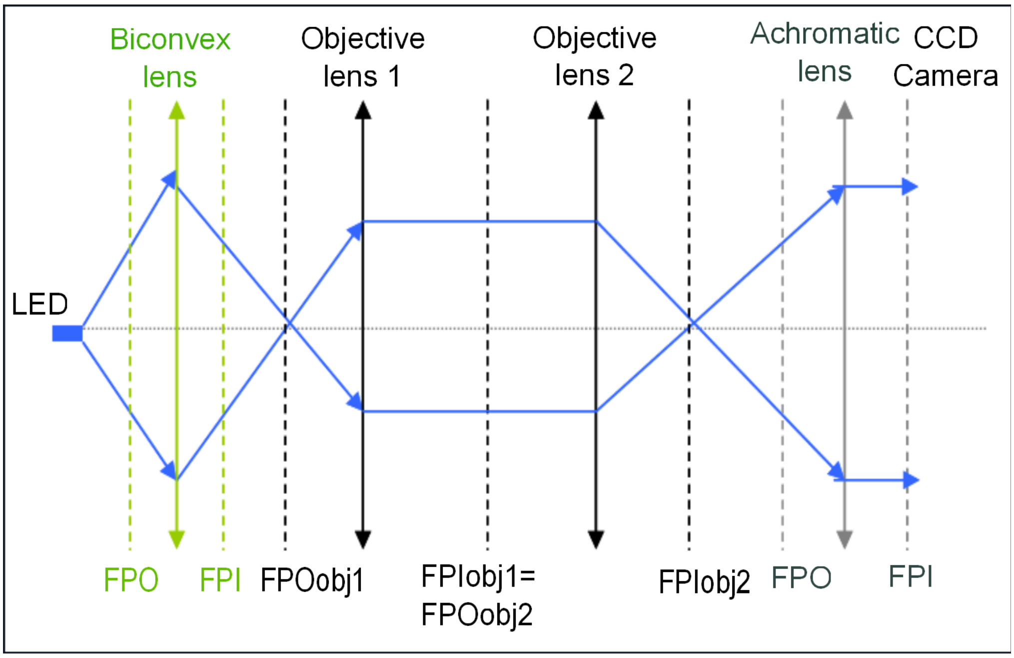

Figure 4.9: *Formation of the Kohler illumination. The Kohler illumination creates parallel rays through the focal region between the objective lenses. "Objective lense 1" corresponds to the focuser and "Objective lense 2" corresponds to the condenser. To simplify the drawing, the objective lenses, which are complex devices, are shown here as thin lenses. The light travels from the LED to the CCD camera. The discontinuous lines show the focal plane object (FPO) and the focal plane image (FPI) of each lens.*

The *x,y,z motorized stage* (Newport 561D-XYZ) is installed on the second level of the instrument and it is operated by three *motors* (Thorlabs Z606). The microfluidics chamber is fixed to the motorized stage by a support called the *stage spreader plate*. By moving the stage spreader plate, the microfluidic chamber can be moved in the axis perpendicular to the laser (x and y axis) as well as in the longitudinal axis (z axis).

The microfluidics chamber is positioned between the objective lenses. One objective lens is fixed and the other is mounted on a linear stage (Newport DS40-X). This stage allows the displacement of the objective lens in the z axis to increase or decrease the distance between the objective lenses and to focus the beams.

A blue LED has been used to illuminate the experiment and to obtain a CCD camera image (Fig.4.9). The light from the LED passes though a bi-convex lens (KBX034) and an achromatic lens (LAO-175.0-25.0-CVI-Melles Griot) creating a Kohler illumination before arriving to the CCD camera (Watec 902H3- Supreme) (See in section 4.5.2). A focus tube of 5.7 cm has been placed in front of the CCD camera to allow the image to be focused and to depurate marginal rays before they arrive to the CCD detector. Two IR filters have been placed along the optical path, one just after the achromatic lens and the other at the free side of the focus tube.

The fluidics system is mounted on the third level of the instrument. This system is composed of a set of bottles and valves to control the circulation of the buffer and the beads. The experiments are carried out in a microfluidics chamber specifically designed for use in the instrument with TC

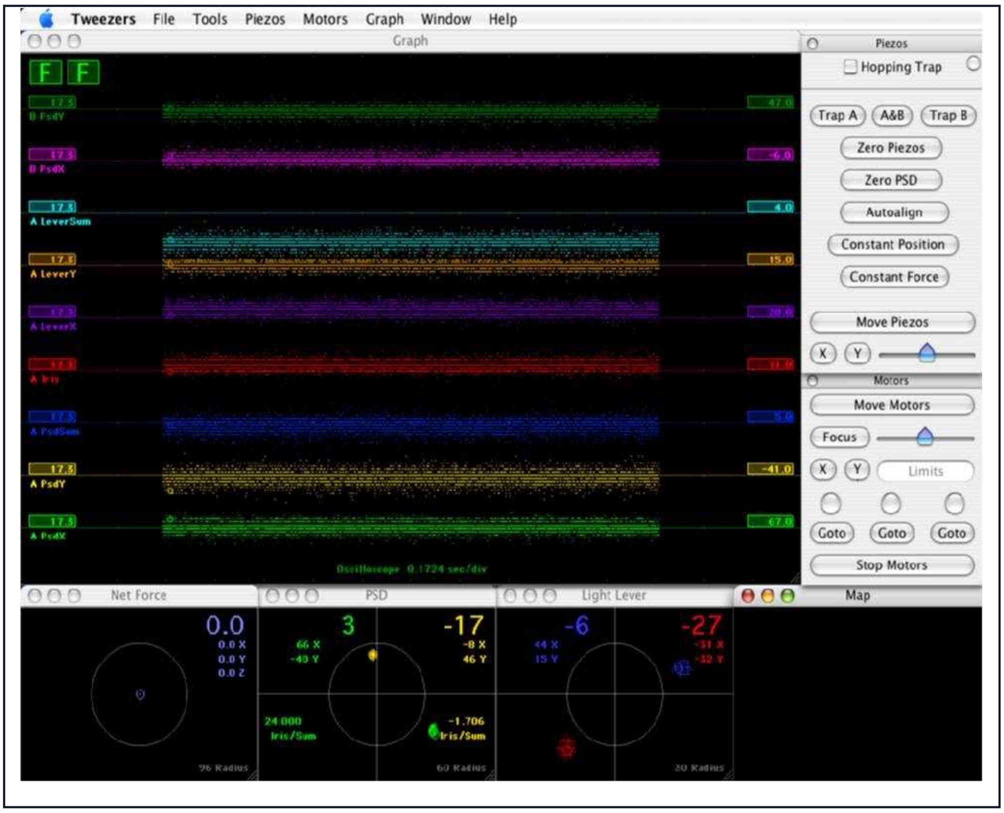

Figure 4.10: *User interface of the lt application.*

(Section 4.5.4). An improved fluidics setup that contains an electric solenoid valve for flushing buffer and also for washing the chamber of sticky beads and bubbles. The electric valve creates a shock wave in the fluid whenever it is activated, which is useful when trying to break multiple tethered molecules. The valve is also useful for admitting a big flow from an external buffer syringe.

4.2.2 Host computer:

The host computer enables users to send commands to the instrument. It is also used to collect and record data as well as to implement experimental protocols. The host software is called "*lt*" for *laser tweezers* (Fig.4.10). It runs on a Mac computer and it is compiled for the version Mac OSX 4 (*Tiger*). The communication between the host and the electronic boards is accomplish by USB.

The data from the experiments is saved in two files, $nameofthefile.txt$ and $nameofthefile.com$. The $nameofthefile.txt$ contains the columns with the raw data. The *lt* application allows us to choose up to 40 parameters of data collection ($CycleCount/n$, $PsdX_A$, $PsdY_A$, $PsdSum_A$, $DistX_A$, $DistY_A$, etc). The $nameofthefile.com$ saves the chronological information of the experiment, for example: when one protocol is turned on/off, when the zero force is applied, when the file stopped to take data, etc....

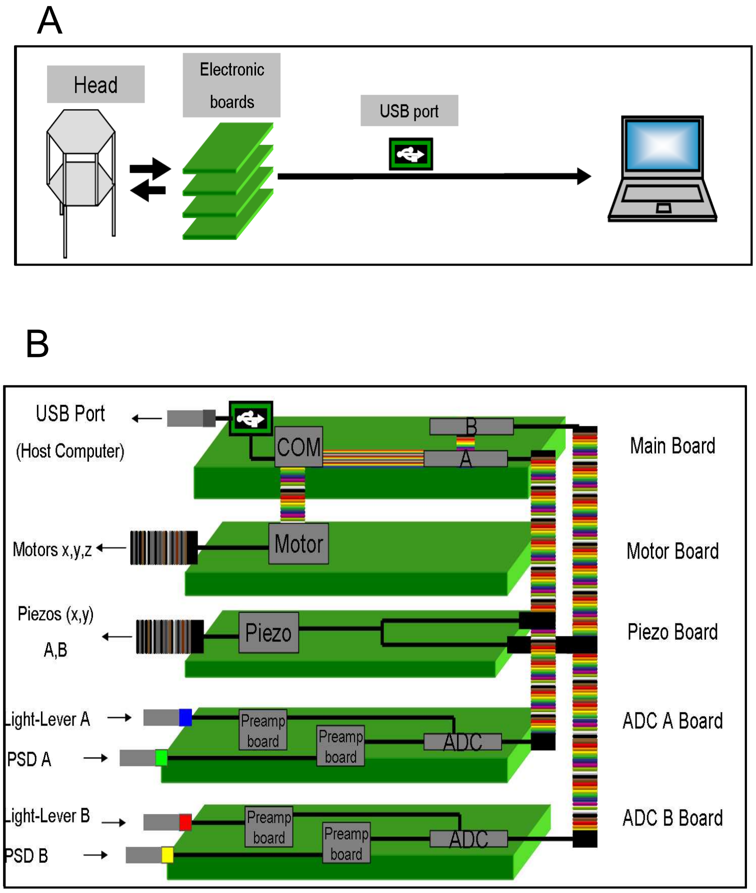

Figure 4.11: *A. Minitweezers setup schematic showing the connections between the different components. Data leaves the head and arrives at the electronic tower. The electronic tower has 5 microprocessors called Peripheral Interface Controllers (PIC). The PICs are responsible for the measurement of data and the interface between the tower and the host computer. The connection between the tower and the host computer is made by USB, which sends the information at 1000 lines/s. This means that the data are received by the host computer with an acquisition rate of 1kHz. B. Electronic boards schematics.*

4.2.3 Electronic boards:

The electronic tower is formed by 5 electronic boards: the *Main* board, the *Motor Control* board, the *Piezo Control* board and 2 *Analogical Digital Converters* (*ADC*) boards. The two ADC boards are identical and independent, one for each optical trap. The electronic boards enable the communication between the instrument head and the host computer (Fig.3.11.A).

Going in order, first is the *Main* board. This board establishes the interface between the host computer and the electronic tower using a USB transceiver. It contains three microcontrollers called Peripheral Interface Controllers (PIC) *PIC*18*F*6520 which perform various functions including the feedback algorithms of constant force or constant position. The first microcontroller (*ComPic*) establishes the communication between the USB transceiver and the two others PICs and it is connected to another PIC installed in the *Motor Board*. The second PIC establishes the communication between trap A and the rest of the electronic boards. The third PIC establishes the communication between trap B and the other electronic boards.

Next is the *Motor control* board. This board has a PIC which controls the motorized stage in the instrument head. The *MotorPic* is connected to the *ComPic* in the Main board and controls the functions of the three motors (Thorlabs Z606) which moves the x,y,z stage. The use of the stage and motors represent a very important improvement over the piezoelectric platforms used until now to move the microchamber in OT instruments.

The *MotorPic* records the positions of the motors in each movement. This allows an automated experimental methodology in which given positions such as the position of the pipette or the position of the dispenser tubes can be recorded to automatically reposition the chamber.

Next is the *Piezo control* board. This board has a Digital-Analog converter which receives orders from the host as a digital signal and converts the signal into analog pulses. The pulses are sent to the piezoelectric actuators of the wigglers.

The last two boards are the *Analogic Digital Converter* (*ADC*) boards. These boards are identical, one for each optical trap (A and B) and receive the analog signals from the PSDs. Each ADC board receive two signals of force (PSD_x, PSD_y) and two signal of position LL_x, LL_y. These signals first arrive to the *Preamboard*. There is one *Preamboard* for each *ADC* board (Appendix A).

The *Preamp board* transform the 2 signals of force (PSD_x, PSD_y, LL_x, LL_y) into one: $PSDSUM$ (total intensity of the beam). After that the $PSDSUM$ signal and the LL_x and LL_y signals are sent to the ADC board which makes the conversion to digital data.

4.2.4 Laser driver box:

The laser driver box is an electronic device that adjusts the power of the lasers and control their temperature. It is specially designed to control both lasers. The values of power and temperature are monitored on two panels on the box. It has a dual digital voltmeters to indicate laser current, temperature, power, set-points, limits, etc. Temperature is monitored with a the thermistor in the laser while controlling their temperatures through Peltier coolers. Inside of this box there are 2 Thorlabs Diode Drivers (IP500) and 2 Thorlabs Temperature Control Modules (TCM1000T), each kind of bord to control the current and the temperature of each laser.

4.3 Methods of calibration

Calibration is critical to maintain the accuracy of measurements by the instrument. The calibration process converts analogical data into physical magnitudes. In the mT setup parameters such as temperature, time, force and distance must be calibrated. The calibration of the mT involves three primary magnitudes: time, distance and force. The rest of the magnitudes such as motor velocity and pulling rate could be measured by combinations of those three ones.

This thesis will explain in detail the calibration of $force$ (Section 4.3.1) and of *distance* (Section 4.3.2).

4.3.1 Calibration of Force

The mT force calibration can be performed using several methods, allowing cross-check between the methods.

Calibration by Conservation of linear momentum:

The advantage to this method of calibration versus others is that this method works independently of the size of the bead, the viscosity and index of refraction of the medium. As described in the previous section, the equations used to calibrate the forces are equations 4.7 and 4.8 developed and explained in detail in [56], where:

$$F_x = \frac{D_x R_D}{c R_L \Psi} \tag{4.7}$$

$$F_y = \frac{D_y R_D}{c R_L \Psi} \tag{4.8}$$

To calibrate the force using this method it is necessary to know the values of R_L, Ψ and R_D. As it was described by Smith et.al: " *They can be obtained from manufacturers specifications but it is best to measure these quantities in situ to account for attenuation in lenses, cubes or filters and also the magnification factor from lenses acting on the position detectors.*" where:

- D_x and D_y are the signals of the deflection of the light that arrive to the PSDs from the optical trap. As shown in Eq 4.7 and Eq 4.8, these values are proportional to F_x and F_y. The signals from the PSDs pass though the *Preamp* and are converted to digital signals in the *ADC* boards.
- c is the speed of the light ($c = 2.997 \cdot 10^8 m/s$).
- R_L is the focal length of the objective lenses. The specifications of an infinity-corrected objective allows R_L to be obtained using the tube-lens focal length of the microscope (specific to each manufacturer) and the *Magnification* of the objective.

  $$R_L = \frac{TubeLength}{ObjectiveMagnification} \tag{4.9}$$

  According to Olympus, their tube lenses all have a focal length of 180 mm. Since our objectives have 60X magnification, the value of R_L should be 3 mm. However careful measurements using apparatus similar to Fig.6 in [56] indicate the actual values of R_L average about 2.95 mm for our objectives.
- Ψ is defined as the power sensitivity of the PSDs. This factor measures the sensitivity of the PSDs by transforming the PSD signals (*SUM Counts*) to power (*Watt*). The unit of Ψ is *Counts/Watt*.

The calibration is carried out using a micro-chamber filled with water and running only one laser at a time. The power factor Ψ is calculated by taking geometric mean of Obj_{IN} and Obj_{OUT} to estimate power at the focal point of the trap:

$$\Psi_1 = 1000 \cdot \frac{P^1_{PSD}}{\sqrt{Obj^1_{IN} \cdot Obj^1_{OUT}}} \tag{4.10}$$

$$\Psi_2 = 1000 \cdot \frac{P^2_{PSD}}{\sqrt{Obj^2_{IN} \cdot Obj^2_{OUT}}} \tag{4.11}$$

P^1_{PSD} and P^2_{PSD} are the SUM powers measured by the PSDs from laser 1 and laser 2 in *counts*. Obj^1_{IN} and Obj^1_{OUT} are the signals in mW measured using a power meter (Thorlabs PM100A / S130C set to 845 nm) where Obj^1_{IN} is the power going into the right objective and Obj^1_{OUT} is the power coming out of the left objective for laser 1 when laser 2 is turned off. And the values of Obj^2_{IN} and Obj^2_{OUT} are the same as described above with laser 2 turned on and 1 turned off (Table 4.1)

Laser	Power	Power(IN)	Power(OUT)	Sum(counts)	$\psi(counts/W)$
A	50 mW	42.3 mW	22.1 mW	12120	396402
A	100 mW	85.9 mW	44.9 mW	24225	390071
B	50 mW	46.8 mW	24.9 mW	12630	369982
B	100 mW	94.5 mW	50.6 mW	25470	368330

Table 4.1: *Photodetector Sensitivity measurement*

- R_D radius of the area or the effective width of DL-10 detector (PSD). This number can be taken from manufacturers specifications ($R_L = 5mm$), however it is convenient to measure directly in the setup for each PSD. To measure the effective width of the DL-10 detector experimentally we used the program "Raster test" [59], a 30 mW Melles Griot laser diode at 830 nm wavelength and masked to a spot 2 mm in diameter which transmits 9 mW. The laser diode is then moved in a 6 mm square X-Y pattern.

  The idea is to calculate the effective size of the photodetectors referenced to their conjugate image which is at the BFP of the objectives. We do this by removing the objectives but passing a laser beam through the position where the objective BFP would have been located. That laser beam continues on through the relay lenses and falls onto the PSD. Then we translate the beam continues on through the BFP by a known distance using the motorized actuators, and we measured changes in the deflections D_x and D_y. The deflection signal should change from +SUM to -SUM when the beam passes across the entire width of the PSD. Thus we can define tractional distances on the PSD which are $Dist_x = D_x/SUM$ and $Dist_y = D_y/SUM$. Plotting $Dist_x$ and $Dist_y$ against the motor positions $Motor_x$ and $Motor_y$ gives slopes that are the inverse of the effective detector width in microns.

Then according to the calibration factor given by $ForceSens[x, y] = R_D/cR_L\ \Psi$ the values of the $ForceSens[x]$, $ForceSens[y]$ for each PSD in x and y axis are:

- TrapA$_{FS}ens_X = (4.878/(2.95 * 2.9973\cdot\ 10^8 * 393200) = 0.0140 pN/count$
- TrapA$_{FS}ens_Y = (4.850/(2.95 * 2.9973\cdot\ 10^8 * 393200) = 0.0140 pN/count$
- TrapB$_{FS}ens_X = (4.885/(2.95 * 2.9973\cdot\ 10^8 * 369200) = 0.0150 pN/count$
- TrapB$_{FS}ens_Y = (5.000/(2.95 * 2.9973\cdot\ 10^8 * 369200) = 0.0153 pN/count$

The calibration of the force in the z axis is found using the equation: $ForceSens[z] = n/(c\Psi)$, where the Ψ value is different from the value obtained by the axial direction. In this case, the sensitivity of the photo-detector depends on the profile created by the *bull's*

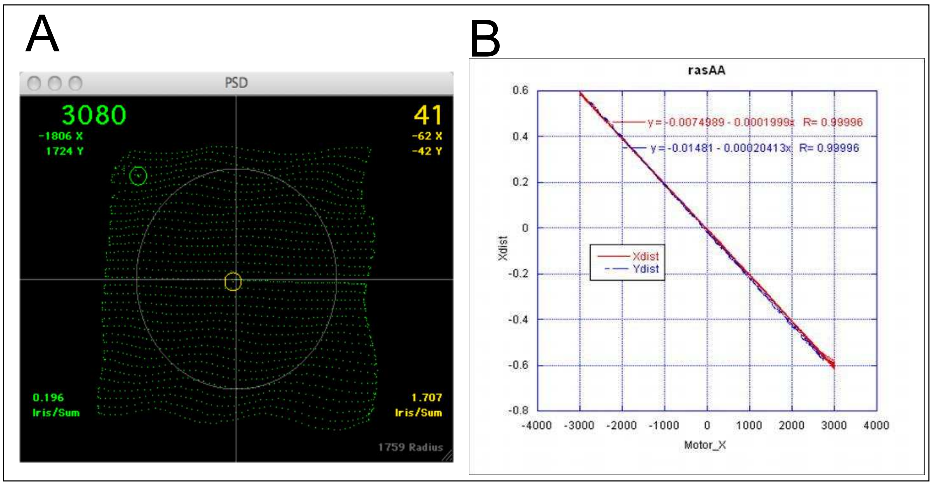

Figure 4.12: *Methodology used in the Raster test. A. To measure the effective size of the photodetector, a laser diode Melles Griot of 830 nm wavelength is moved in a 6 mm square X-Y pattern on each PSD. B. Plot obtained to measure the effective detector width. The slopes shown in this example would indicate:* $R_{Lx} = 1/0.0001999 = 5.0025mm$ *and* $R_{Ly} = 1/0.00020413 = 4.8988mm$.

eye attenuator, where the bull's eye attenuator shape is measured against the radius of the PSD and the intrinsic sensitivities of the detector are measured (Fig. 4.8).

For example, if the values of the z force sensitivities are $IrisSens_A = 452000$ and $IrisSens_B = 425000$ then the force sensitivities for each PSD in z axis are given us by:

- $TrapA_ForceSens_Z = 1.332/(2.9973 \cdot 10^8 * 452000) = 0.0098pN/count$

- $TrapB_ForceSens_Z = 1.332/(2.9973 \cdot 10^8 * 425000) = 0.0105pN/count$

Calibration by Stokes Law

When an object falls through a fluid it experiences a viscous drag. This effect was studied by George Gabriel Stokes in the middle of the nineteen century, who spent most of his life working in fluid properties. His work lead to the development of Stokes Law, a mathematical description of the force required to move a sphere through a viscous fluid at one specific velocity. Stokes Law is written as:

$$F = 6\pi r\eta v \tag{4.12}$$

Where F is the drag force, η is the viscosity of the fluid, r is radius of the sphere and v is velocity of the sphere relative to the fluid. By using this well known equation, it is possible to describe the rate at which the sphere falls. The calibration of the force by using Stokes Law is done in a chamber with pure water and by using specific polystyrene microspheres for calibration of a known size. These microspheres, bought from the company Polyscience, have a nominal diameter of 3.00 μm and a standard deviation of 0.226 μm (Fig.4.13).

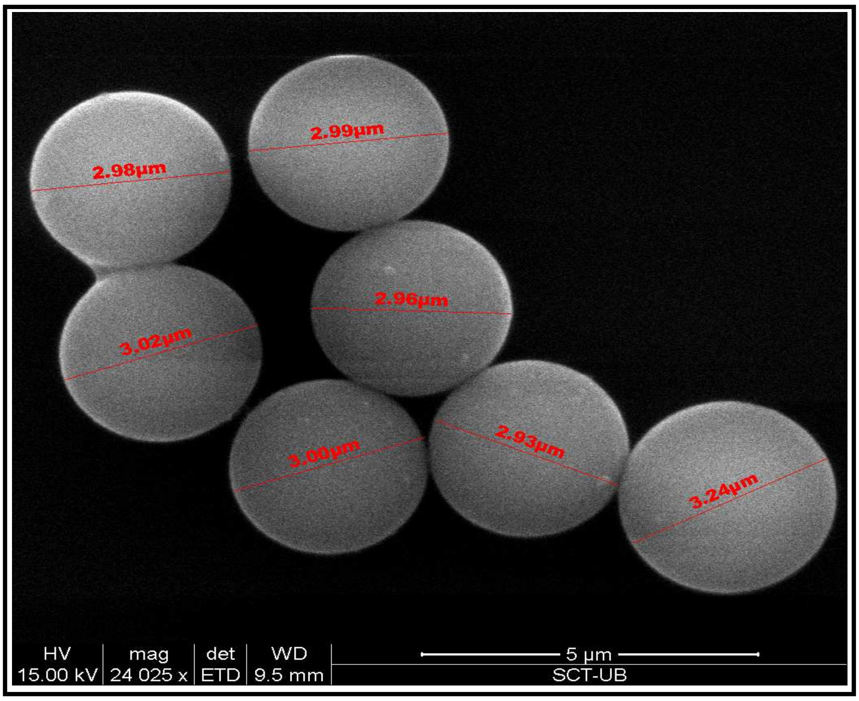

Figure 4.13: *Image of the polystyrene microspheres (Microbead Nist Traceable particle size standard 3.00 μm ± 0.226 μm; Ref:64060 - DISC calibration of Polyscience) obtained by SEM-UB.*

To carry out this method of calibration, one microsphere is trapped in the optical trap. Knowing the velocity at which the chamber is moving and the drag coefficient of the particle in the buffer solution we can calculate the force on the particle by using the equation (3.12). This method is used to calibrate each axis (x, y, z) (Fig.4.14).

Calibration by Brownian motion

It is possible to calibrate the force and the stiffness of the optical trap using the Brownian motion of a trapped bead [60, 61].

The motion of a Brownian particle in an harmonic potential can be used to measure the stiffness of the optical trap (κ). Brownian motion corresponds to the random movement of a trapped bead suspended in a liquid of known viscosity and temperature. This method requires knowledge of the beads diameter.

The analysis to calibrate the optical trap using Brownian motion is carried out using the *power spectrum*. The *power spectrum* is an useful spectral analysis tool which helps identify periodicities and supports us with valuable information about random signals. The power spectrum decomposes the content of a stochastic process into different frequencies present in that process (Fig 4.15).

In that case the random signals are the fluctuations in position x (relative to the center of the trap) and the fluctuations in force of a particle trapped in an optical trap, where the relation between the force and the position are:

$$f = -\alpha x \tag{4.13}$$

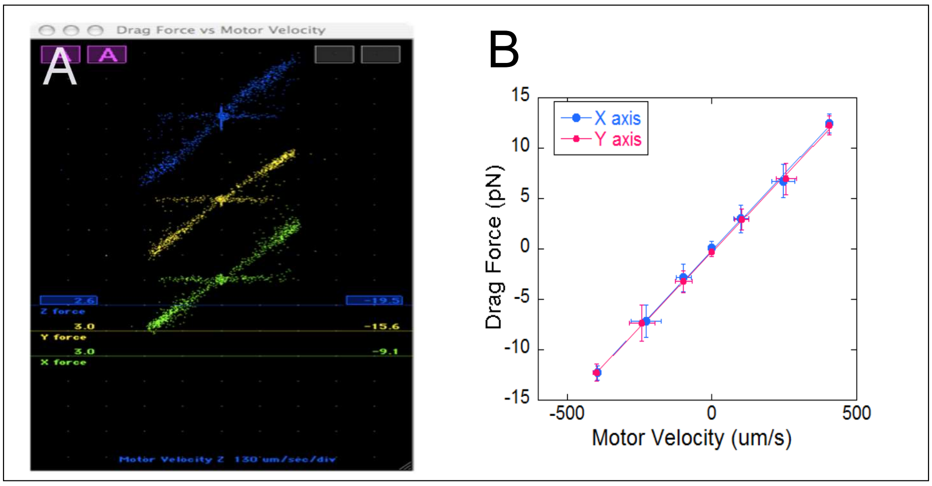

Figure 4.14: *Stokes Law calibration. A. Drag force versus Motor velocity for the x (green dots),y (yellow dots),z (blue dots) axis. This image is taken directly from the screen of lt program. B.Analysis of Stokes calibration test. Blue dots show the experimental measurements for the x axis, Pink dots show the experimental measurements for the y axis. The linear fit is depicted too. The drag coefficient is obtained from the slope of the fit, because* $F = 6\pi\eta r v$. *The slope of the linear fit is the calibration factor.*

The amplitude of the fluctuations in position x and force f in Fourier space are defined by their corresponding power spectrum which is shown as:

$$\langle \Delta x^2(w) \rangle = \frac{2k_B T}{\gamma(w_c^2 + w^2)} \tag{4.14}$$

$$\langle \Delta f^2(w) \rangle = \frac{2k_B T \gamma w_c^2}{(w_c^2 + w^2)} \tag{4.15}$$

where k_B is the Boltzmann constant, T is the temperature, w_c is the corner frequency of the bead and γ denotes the drag coefficient (in distilled water $\gamma = 6\pi r$). Position and force fluctuations represent measurements of noise and their acquisitions depends on the bandwidth of our Data Acquisition (DAQ) system. To calibrate the trap using this method we must determine the corner frequency (w_c) of the power spectrum from which κ is given as:

$$k = w_c \gamma = 2\pi \nu_c \gamma \tag{4.16}$$

With the DAQ system of the mT we can acquire a maximum DAQ rate of 1kHz. The corner frequency of the bead normally falls at around $\nu = 600Hz$. Consequently, in order to calibrate the stiffness of the optical trap, we need a DAQ system with a faster DAQ rate (Appendix A).

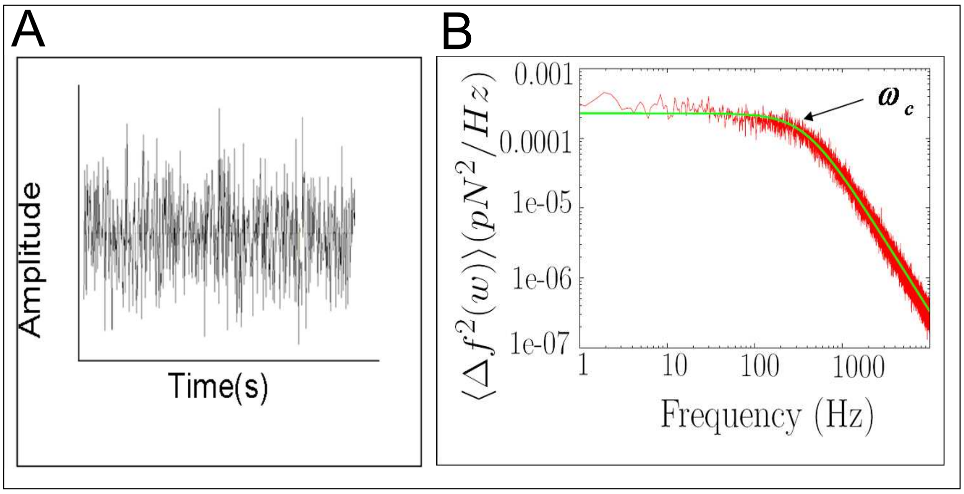

Figure 4.15: *Power spectral density. A. 1 second of recording force signal (data from PSD). B. Power spectrum of the signal from PSD (laser A, coordinate y). The signal is received with a DAQ board which works at 100kHz (Appendix A). Fit of the data to a Lorentzian function with a value of* ν_c *of 365Hz. Data were recorded for 5s.*

4.3.2 Calibration of Distance

The calibration of distance in the mT requires the calibration of the motors that move the chamber and the LL PSDs. In order to calibrate the displacement of the chamber acted by the motors, we must know the full specifications of the motors.

The calibration of the motors is carried out using three important components, the *Motor Control* board, the shaft encoder internal in each motor and the external screw of the motor which makes contact with the motor stage. The *Motor Control* board sends electronic pulses to the shaft encoder. The shaft encoder regulates the direction and number of revolutions of the motor. We know that 48 pulses from the *Motor Control* board are equal to one motor shaft revolution. We also know that 256 shaft revolutions correspond to 1 revolution of the screw. One revolution of the screw is equal to 0.05 μm of travel on the stage. By using these relations ships we deduce that 245760 pulses=1 μm of distance.

The calibration of the LL photodetectors requires the calibration of the motors. To calibrate the LL photodetectors is necessary to do a simple experiments which requires a bead in the optical trap, a pipette and a feedback algorithm of constant force. The bead is fixed in the optical trap, then the bead is immobilized on the tip of the pipette. Next the constant force protocol is applied and the instrument user moves the microchamber in x and y axis. The optical trap automatically follows the bead in real time maintaining a constant force reading on the LL PSDs. Knowing the distance (in μm) the motor stage has moved the microchamber it is possible to determine the conversion between the (Analogical-Distance Units) ADU transmitted from the LL PSDs to μm unit. This calibration is carried out for each laser on the x and y axis.

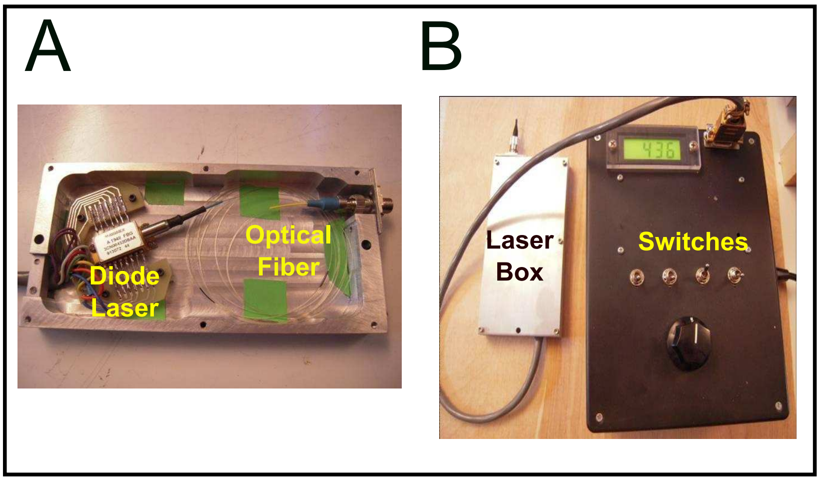

Figure 4.16: *A. Picture of the heating laser mount. Only 8 pins of the butterfly laser are used to measure and control the power and the temperature of the laser diode. B. The heating laser is controlled by a power supply specifically designed for this laser. The power supply incorporates 4 different switches that work as a binary set of switches. These are labeled as 1,2,4,8. In binary each switch has the option to be in 1's or 0's. The combination of the 4 switches and their placement in binary give us 16 set of options. By starting with (0,0,0,0) when the current of heating laser is 0mA until (1,1,1,1) where this set of switches correspond to the maximum current of the heating laser (160mA). Between the two limits there are 14 probabilities, for example (1,0,0,0), (0,1,0,0), (1,1,0,0), (Appendix B) Each switch is related with a specific current of the laser then by increasing the 1s in the position of the switches the heater power will increase too.*

4.4 Developing the Temperature Controller

As it was explained Chapter 2 is difficult to control temperature in OT instruments. By following the same laser-heating method used by Mao. et al [43], one of our aims has been to resolve some of the not easily problems that they found during the development of the TC.

In this section we will describe the technological developments undertaken to resolve these problems. A full description of the modifications of the mT including the addition of the heating laser and the methodology carried out to obtain a range of temperature between 5°C and 50°C follows.

4.4.1 Heating laser: description and optical adsorption

The idea of our setup is to introduce a new method to change the temperature locally and rapidly making possible to change the temperature with the maximum of stability.

In addition to the two trapping lasers of the original setup an additional laser has been added to generate heat around the optical trap. This laser called the *heating laser* is a diode laser which works at λ =1435 nm and according to its specifications the maximum power is 160 mW. The current of the laser is controlled by a power supply specifically designed for this laser (Fig 4.16).

The wavelength of the heating laser has been chosen carefully to generate heat in the bulk solution by Infra Red (IR) absorption without transmitting unnecessary extra heat to the objective lenses or the rest of the optical components (Appendix C) thus effectively eliminating drift. Previous studies have used the absorption of IR light in water as a method to heat rapidly and locally the surrounding medium [62, 63, 64]. We use a wavelength of 1435nm which is readily absorbed and has a penetration depth of 315 microns in water [65, 66]. However for a wavelength of 980 nm, as used in previous studies, the penetration depth is around 19920 microns. Therefore little of the incident light was absorbed in a water cell only 180 μm thick.

The heating laser power is controllable between 0 and 160 mW (Appendix B) with wavelength λ=1435 nm and, and following the literature an adsorption coefficient, $\alpha(\lambda)$, between 31.0 and 31.7 cm^{-1} [65]. The use of this wavelength is very appropriate for our experiments for two reasons: (1)λ=1435 nm does not interfere with the signal of 845 nm in the photodetectors of force. These photodetectors have the spectral response between 500 nm and 1100 nm; (2) According to Beers Law the loss in intensity due to adsorption as light travels through the medium is given by:

$$I = I_0 \exp^{-(\alpha x)} \tag{4.17}$$

where $\alpha(\lambda)$ is the adsorption coefficient and x is the distance that the radiation travels through the water solution. Our measurements show that the adsorption coefficient of the water is equal to 31.1 cm^{-1} (Appendix D).

4.4.2 Design of the temperature controller

Operation below room temperature

A goal of our new temperature controller setup is to create a microfluidics chamber very homogenous and stable when temperature changes. One solution could be to maintain the instrument, the microfluidics chamber, the objective lenses and the air between them at the same temperature. By using this method we make sure that the thermal drift is avoided. The best way to do this is to enclose the instrument in an insulated box where the temperature will be maintained constant at the desired temperature. However there are important issues related with the optical alignment and the focus of the optical trap that must be taken into account (Appendix E).

To reach low temperatures the instrument is placed inside of a 1.5m^3 top-opening icebox containing 20 liters water which is frozen into a block of ice. The icebox is turned off and the ice melts slowly. This maintains the temperature inside the icebox at a constant 4°C-5°C. The optical tweezers instrument is then placed inside of the icebox using a pulley operated vibration isolating suspension system which suspends the instrument inside the icebox without allowing it to make contact with any hard surface. The instrument then needs around 3 hours to equalize with the temperature inside of the icebox. The temperature of the instrument is measured using a thermal sensor installed close to the fluidics chamber. When the temperature of the instrument has stabilized inside of the icebox, it is possible to increase the temperature around the optical trap by using the heating laser.

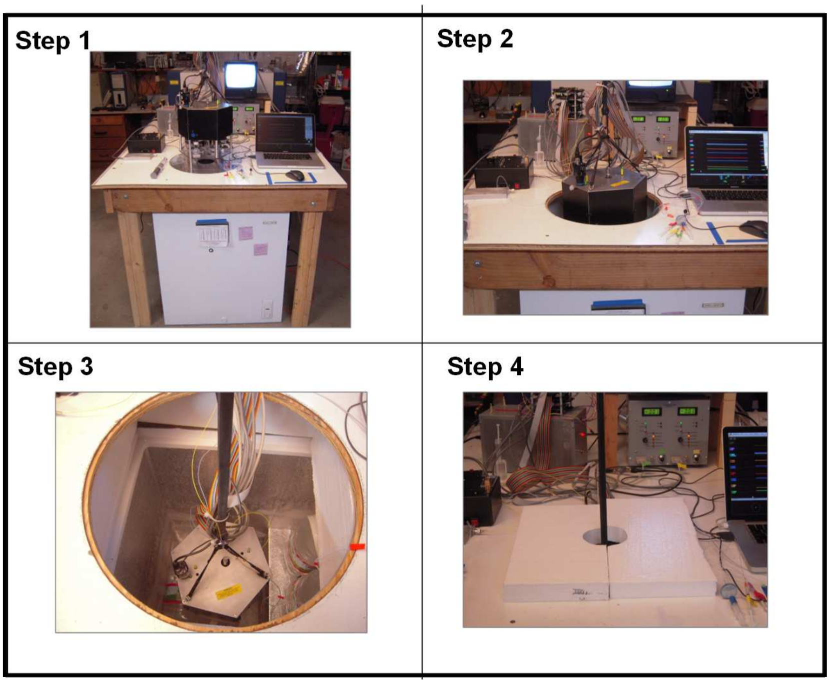

Figure 4.17: *Steps to reach at low temperatures: Step 1) The icebox is turned on. Inside there are two jerry cans with water inside. When this water is frozen, the icebox is turned off and the ice of the jerry cans melts slowly. The temperature inside of the icebox is constant around* $4^\circ C$*-*$5^\circ C$*. The temperature is controlled by a digital thermometer with an external probe. Step 2) and Step 3) When the temperature inside of the icebox is around* $4^\circ C$*, the optical tweezers instrument is placed inside by using a pulley suspension system which suspends the instrument inside the icebox. Step 4) When the optical tweezers is inside needs around 3 hours to equalize with the ambient temperature of the icebox. The icebox is covered with a thermally insulated material to avoid to increase the temperature inside of the icebox. Close to the fluidics chamber is installed a sensor temperature which allow us to know the ambient temperature of the instrument at each moment. The drop of temperature is monitored by using the lt program.*

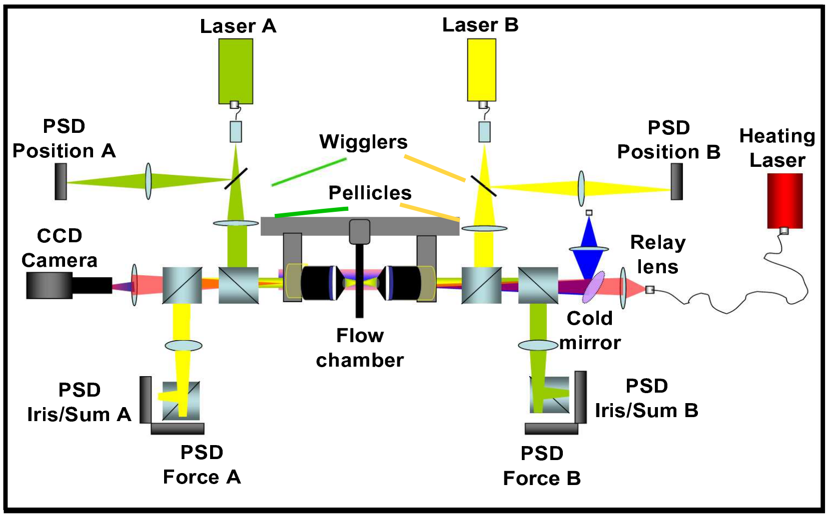

Figure 4.18: *Counter-propagating optical trap with light-momentum force sensor [58, 59, 14, 67] modified to include a temperature controller. The two objective lenses are Olympus 60x Water Immersion, NA 1.2. There are also two trapping lasers (Lumics LU845) both emitting at λ= 845 nm with 150 mW maximum power. The heating laser (Alcatel A1948FBG) emits at λ= 1435 nm with 160 mW maximum power. The heating beam passes through a 45° dichroic long-pass filter (Edmund Optics 69-878), which acts as a "cold mirror". That is, it reflects the blue LED light used by the CCD camera but allows the heating wavelength to pass through.*

Operation above room temperature

To heat the region around the optical trap has been used the heating laser described in the previous section. The transmission of the light between the heating laser and the instrument has been accomplished using 2.0m of single mode optical fiber (Ref: SMF-28-10) with a FC/PC connector at each end. The heating beam enters in the optical tweezers setup through one of its side prism boxes and is directed by a 45° dichroic long pass filter which acts as a *cold mirror* (Edmund optics; Ref: 69-878), which reflects the blue LED light and allows the heating wavelength light to pass. The light of the heating laser expands and travels 8.2 mm until it arrives at the adjustable relay lens (Thorlabs CFC-8X) which is mounted in a 3-screw kinematic mount (Fig 4.18).

4.5 Testing the TC experimental setup

4.5.1 Temperature measurement using viscosity change

We measure local temperature with a similar method to that used by Mao et al [43] and by Peterman.et.al [62]. That is by using a trapped bead as a probe to detect changes in the viscosity of the water surrounding that bead. This method consists of two steps.

(1) Fill the fluid microchamber with an aqueous buffer where the viscosity changes with temperature. Measure the ambient temperature of the chamber with a nearby sensor (Analog Devices AD590) which was previously calibrated against an Resistance Temperature Detector reference thermometer (Thermoworks THS-222-555). A polystyrene bead is captured in the optical trap, the counter-propagating beams are autoaligned and the force

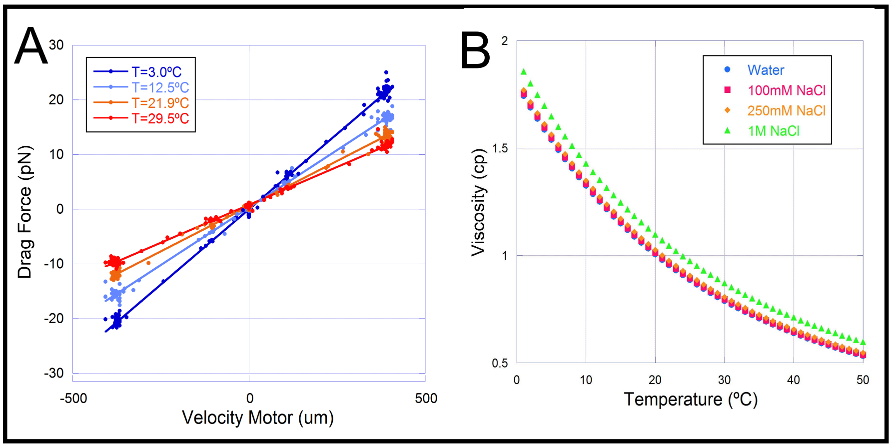

Figure 4.19: *Force calibration at different temperatures. A. Relation between viscous drag force and temperature. Stokes test done with a bead of 3 μm diameter in pure-water. This graph shows the relationship between the viscous drag force and the velocity of the flow at various temperatures. As temperature increases the drag coefficient (proportional to the slope of the force-velocity curve) decreases. B. Relation of Viscosity versus Temperature plotted for distilled water, 100 mM NaCl, 250 mM NaCl and 1M NaCl. Data were taken from Refs [68, 70, 81].*

sit to zero. Use the motorized stage to move the chamber (and buffer fluid) along x and y axis while recording the chamber velocity and force. Make a linear fit to the data points force versus velocity. The slope of that line is dF/dV is the drag coefficient for that bead in that chamber at ambient temperature. Look up the viscosity of the buffer fluid at the known ambient temperature and call that value $\eta(0)$.

(2) Using the same bead, turn on the heating laser to some constant drive current called switch number S. Move the stage back and forth again while recording data of the chamber velocity and force. The slope of the linear fit should be lower because the viscosity of an aqueous solution drops with temperature. Call the new slope $dF(S)/dV$. Calculate the new fluid viscosity as $\eta(0) * (dF(S)/dV)/(dF/dV)$. Consult the viscosity table and determine what temperature corresponds to the new viscosity. That is the temperature of the fluid surrounding the bead for a switch position S (Fig.4.19.A).

A Stokeslaw force calibration of the instrument is carried out using pure water, however the DNA unzipping experiments are carried out in a buffer containing either NaCl (100 mM, 200 mM or 1 M) or $MgCl_2$ (10 mM or 1 mM). Figure.4.19.B shows the effect of temperature on viscosity for various concentrations of NaCl and pure water. These viscosities were entered according to two different sources [68, 70, 81] that were in good agreement. The ionic concentrations used in the experiments with $MgCl_2$ were so low that the viscosity of pure water has been used in these cases.

The viscosity method also allows us to measure the temperature generated by the optical trapping light. The wavelength of 845 nm is absorbed and thus generates some heat at the point of the experiment. For this reason experiments similar to those described above have been carried out at high (80 mW) and low power (20 mW) outputs of the trapping lasers in order to determine how much heat is generated by the optical trap. The difference

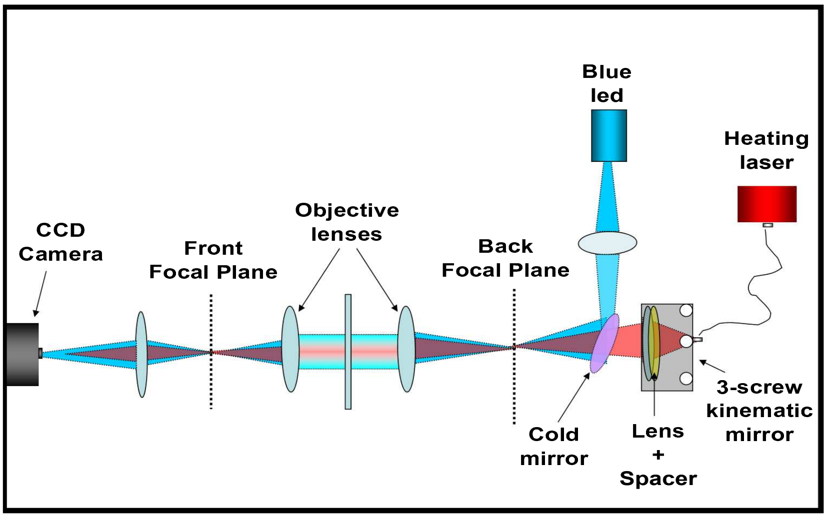

Figure 4.20: *Kohler illumination and heating. The beam from the IR heating laser is focused in the back-focal-plane (BFP) of the right hand objective by using an adjustable-focus collimator assembly (Thorlabs CFC-8X, $f = 7.5$ mm). This assembly has been mounted on a 3-screw kinematic mount (Thorlabs KS05) that allows us to translate the heating laser beam in x-y directions relative to the trapping beam. A 1.5 mm brass spacer ring placed in the fiber-optic (FC) connector of the collimator permits focusing the heating beam onto the BFP of the objective at only 9 cm distance. Thus we create a Kohler like heating beam, about 50 μm in diameter, traveling between the two objectives. All 3 wavelengths (blue, 845nm, 1435 nm) pass the first objective lens and the microfluidics chamber. The light is collected by a second objective lens and imaged on a CCD camera. The wavelength of the heating laser is not visible with a silicon-target CCD. Therefore a 905 nm laser is used for positioning to see the size of the hot spot on the TV screen and to place it near the optical trap.*

in the drag coefficient between the high and low power outputs is about 4% indicating a small temperature rise of 0.9°C-1°C for the highest power of the heating laser.

4.5.2 Kohler illumination for the heating laser:

According to measured changes in water viscosity around the trapped bead, we could increase the temperature by 50°C above ambient if we used full laser power (160 mW) and we also focused the heating laser into a small area of about 10 μm in diameter. However such a small heated area creates a baseline shift in the light momentum force sensor due to refractive index changes in the heated water at the heating laser focus. That is, the 1435 nm heating beam can deflect the 845 nm trapping beam by heating water locally and changing its refractive index. Such refractive interference also occurs when the trap is empty (not occupied with a bead).

To reduce such baseline shift we spread the heating beam out at the focus and changed its shape. Instead of focusing the heater to a point at the experimental plane, we used the heating equivalent of Kohler illumination (Fig.4.20). Thus the heating laser is focused to a point located at the Back-Focal-Plane (BFP) of the objective lens so that the heating beam emerged into the experimental area collimated as a cylinder [43] about 66 μm in diameter (Appendix G). By changing to Kohler heating the typical baseline shift has been reduced

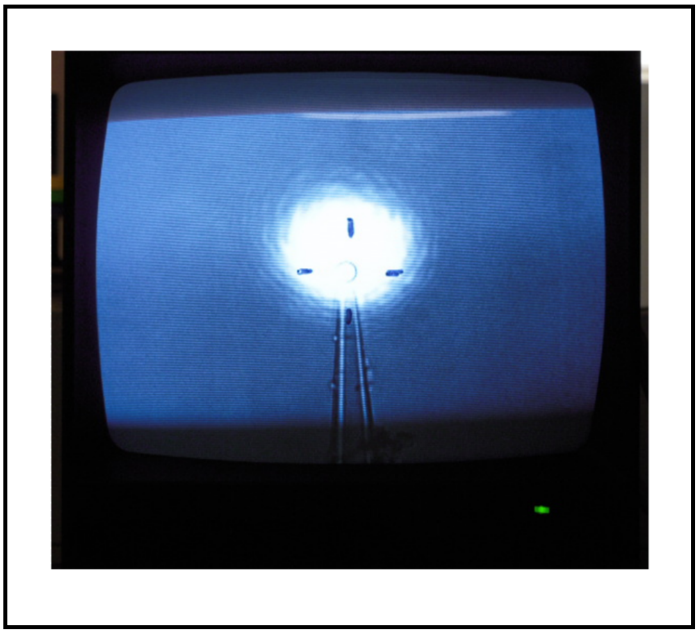

Figure 4.21: *Image of the visible laser. The size of the screen represents around 50 μm x 38 μm and the diameter of the heating laser represents around 66 μm.*

from ≅3pN to only ≅ 0.5pN at full heating power. The maximum temperature increases at the experimental region is however reduced to ≅25°C above ambient temperature. In order to extend the temperature range and to carry out experiments between 5°C and 30°C (cold measurements) the instrument is placed inside of the icebox. For experiments conducted between 25°C and 50°C (hot measurements) the instrument is placed outside of the icebox by operating at room temperature. When the experiments with molecules are done, it is necessary to previously measure each baseline of force after the tether molecule at each temperature has broken.

4.5.3 Size of the heating laser

The laser of 1435 nm is not visible in the CCD camera because the photosensor of the camera is not sensitive to such wavelength. This limitation is a problem not only because it is not possible to see the heating laser but because the placing of the laser in the center of the screen (where the experiments are carried out) is indispensable. In order to place the heating laser in the center of the screen, the laser of 1435nm is replaced by a positioning 975 nm laser (visible laser). This laser is visible in the screen (Fig.4.21). After the visible laser has been relocated in the center of the screen, it is substituted by the heating laser.

The theoretical explanation about how to determine the size of the Kohler illumination cylinder can be found in Appendix G.

4.5.4 Convection problem

By using the laser-heating method a non-uniform temperature profile is created inside the standard microfluidics chamber. The non-uniform temperature region generates a

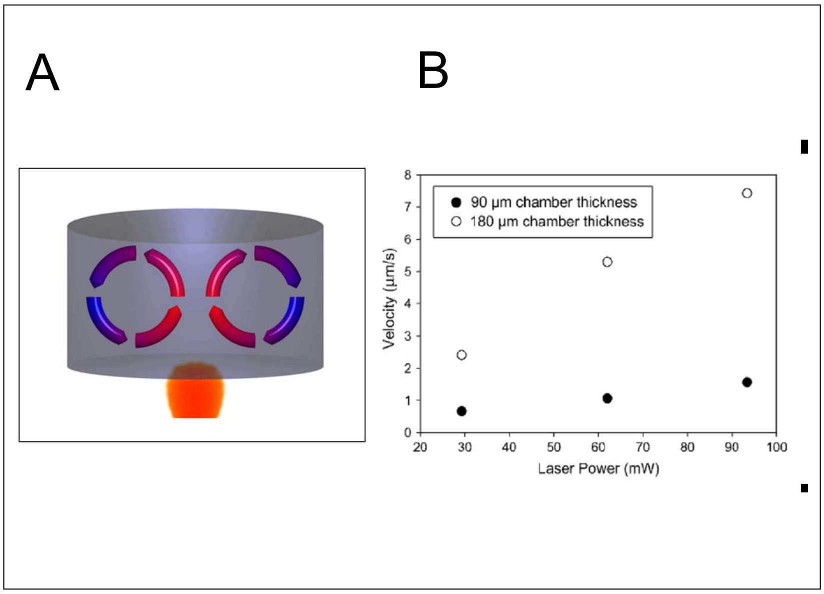

Figure 4.22: *A. Convection effect. B. According to the bibliography [43] the velocity of the convection is reduced from 20 $\mu m/s$ until less of 1 $\mu m/s$.*

convective current inside the chamber. This effect generates hydrodynamic flows between regions at different temperatures that increase with the heat supplied by the heating laser. This is an inconvenient in single molecule experiments, because the flows might exert significant forces on the molecule being pulled (Fig.4.22). The convection effect depends on the amount of heat flux generated around the hot region and is directly related to the power of the heating laser. This effect has been observed to be large with the standard chambers used in the mT. To reduce this effect a new microfluidics chamber has been designed (Fig.4.23).

Experiments were performed by using the new design of the chamber (Fig.4.23) and by using Cargille Labs Refractive Index matching Liquid, Series AAA, N=1.330 (Appendix F) [71] . This liquid is placed between the objective lenses and both sides of the fluidics chamber as a replacement of water. Unfortunately this liquid has lower surface tension than water and is difficult to maintain between the objective lens and the coverglass. To resolve that problem the coverglasses used to make the new fluidics chamber are thicker that those used for the old design [59, 14, **?**]. By using the thick coverglasses the distances between them and the objective lenses become shorter so the Cargille liquid is stably kept for a longer time.

Design of the microfluidics chamber and the fluidics system

The experiments are carried out in a microfluidics chamber specific for mT with TC setup. This chamber is different to the regular chamber design. The microfluidics chamber is done by using two coverglasses (24 mm x 60 mm, N.2 VWR). One of them is drilled with 6 holes for buffer throughput. Between the two coverglasses is placed one layer of Nescofilm (Nesco-Karlan) that has been cut with a specific design (See Fig.4.23.B). The holes of the coverglasses and the drawings on the nescofilm are done by using a laser cutter (Epilog Mini 18).

The assembly of the microchamber starts with the perforated coverglass and with the layer of Nescofilm. The Nescofilm is aligned with the holes on the coverglasses. After that are placed the *dispenser tubes* and the *micropipette* on the layer of Nescofilm. The dispenser tubes are tubes of glass (d_{out}= 100 μm; d_{in}= 25 μm; Garner Glass company) to connect the top and bottom channels with the middle channel where the experiments are done. These tubes can not be positioned further of 5mm from the pipette.

The *micropipette* is done by using a tube of glass (d_{out}= 80 μm; d_{in}= 40 μm; Garner Glass company) and by using a *pipette-puller* to create the micropipette. The tube of the glass is placed in the middle of a circle made by platinum wire. The wire is connected at two electrodes that allow the flow of current for the platinum start to be incandescent. The glass is melted and the weight stretch of the tube producing a *micropipette*. The end of the *micropipette* is around 1 μm of diameter. The *pipette-puller* has been designed and assembled at the University of Berkeley.

When the tubes are placed on the Nescofilm, the assembly is covered by the other coverglass and is heated in a "hot plate" at 120°C until the Nescofilm is homogeneously melted . The thickness of the microfluidics chamber is around 110 μm by using this new design of the microfluidic chamber. The opposite side of the micropipette coming out of the chamber is introduced inside of a polyethilene tube. The micropipette and the tube are connected by using a special glue (Norland,NOA-61; UV Curing Optical adhesives). At the end of the tube it is inserted a syringe which produces suction on the pipette.

4.5.5 How does the force calibration change with respect to the thickness of the chamber?

As was described in Section 4.3, the force calibration could be done by using different methods. A useful method is using the viscous drag exerted by the fluid flow. In the case that the particle is a sphere of radius r_{eff}, the drag coefficient is given by Stokes Law (Eq 4.12). The calibration of the force by using Stokes Law is done in a chamber with pure water and by using polystyrene microspheres specific for calibration. These micro-spheres have a nominal diameter of 3.00 ± 0.226 μm (Fig 4.13).

To carry out this method of calibration, one microsphere is captured by the optical trap. The microchamber is mounted to the stage platform of the optical tweezers instrument that can be moved along the x-y-z axis. From the velocity at which the chamber is moving, the viscosity of pure water and the size of the bead, it is possible to calculate the force on the particle using eq.4.12. This method is used to calibrate force along each axis (x,y,z). Stokes Law experiments have been done using both the old and new microchamber designs (Fig 4.23.B).

With these experimental results it has been demonstrated that if we use Stokes Law as a method of force calibration the proximity of the bead to the wall of the microchamber cover-glass is an important aspect to consider. The effect is known as Faxens Law and could be defined as a correction to the shear viscosity and viscous drag coefficient of a micro-sphere in a viscous fluid sitting close to a wall [72]. However in our case the bead in the trap is in close proximity to two walls comprised of the micro-chamber cover-glasses.

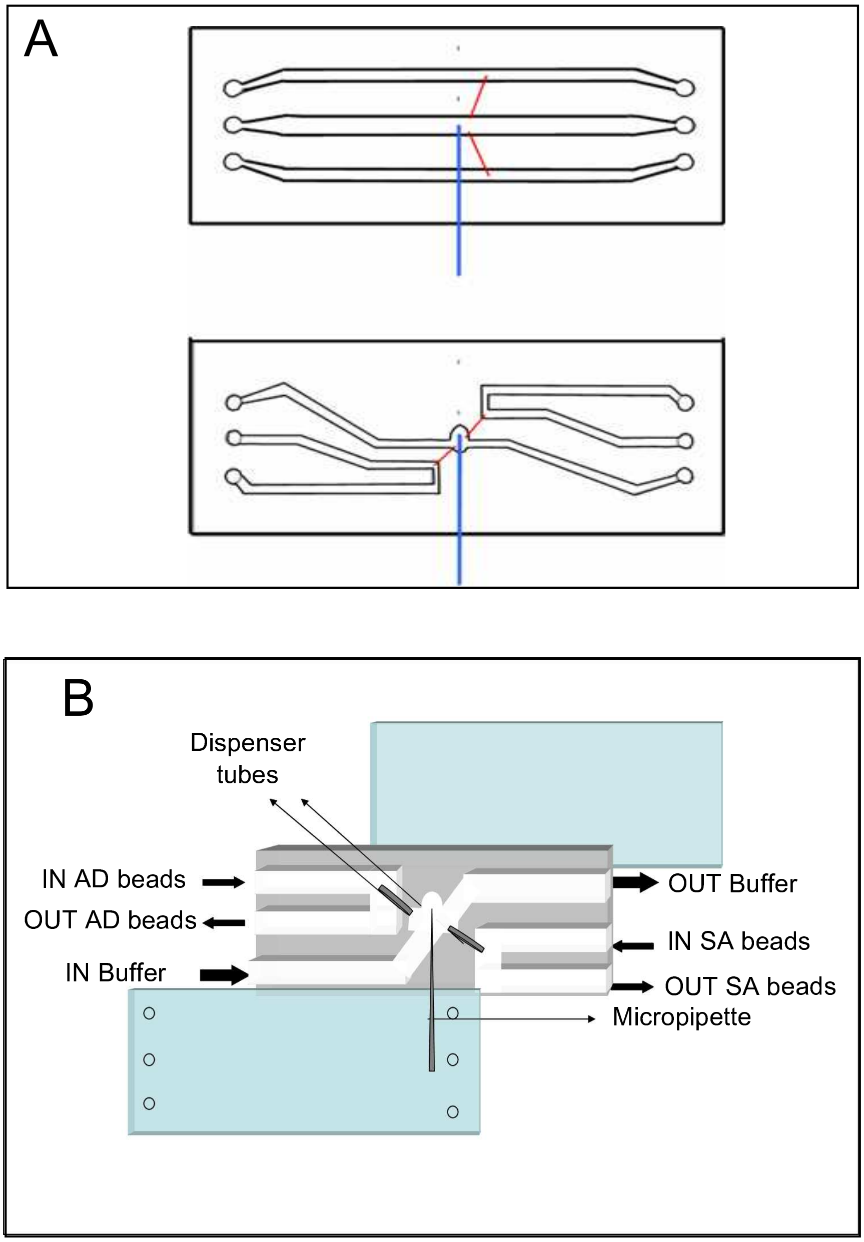

Figure 4.23: *Microfludics chamber. A. Scheme of the old (upper panel) and new (lower panel) microfluidics chamber designed to prevent convection. B. The new design has been made by using two coverglasses (24x60 mm ;2; ref: MARI0103242; VWR) and one layer of nescofilm (instead of two as in the old design). With this design the microchamber thickness has been reduced from 180 µm to 110 µm. The design in the nescofilm has been modified to avoid the obstruction of the lower channel by the micropipette (of approximately 80 µm in diameter).*

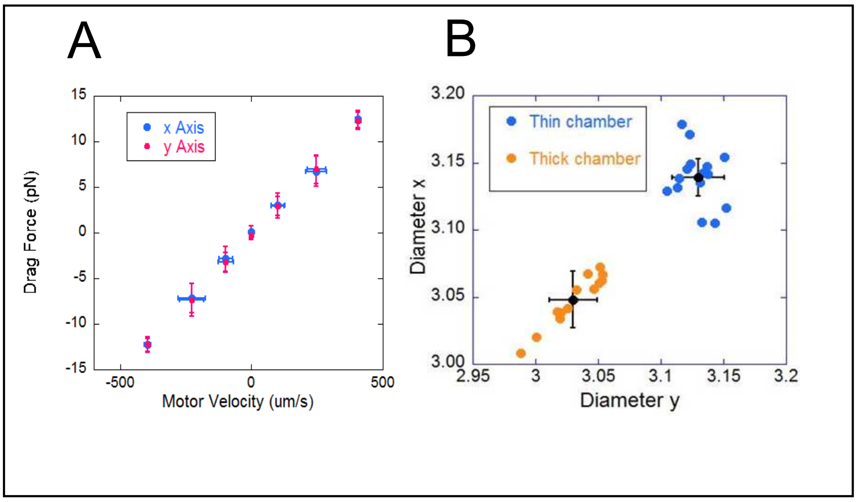

Figure 4.24: *Force calibration using Stokes law. A. Stokes law (Drag force vs motor velocity) used to calibrate the force in the optical plane (x and y). The experiment was done by using pure water and special microspheres for calibration. The points showed in this graph correspond to a single bead and have been obtained by taking the average over the raw data. B. Diameter x-axis vs Diameter y-axis measured by Stokes law calibration and using the standard expression for the drag coefficient* $\gamma = 3\pi\eta d$ *where d is the bead diameter. Data were obtained by measuring over 10/15 beads. The mean diameter obtained in the thick chamber case for the x-axis is 3.05* ± *0.019* μ*m and for the y-axis is 3.03* ± *0.021* μ*m. The mean diameter obtained in the thin chamber case for the x-axis is 3.14* ± *0.021* μ*m and for the y-axis is 3.13* ± *0.014* μ*m. Two different batches of calibration beads have been tested with the same results. The difference observed between the value of mean diameter obtained for both types chambers shows the importance of the Happel correction to the drag coefficient as given in Equation 4.18.*

For this reason we have corrected Stokes Law using the Happel correction [73]. The viscous drag coefficient of a micro-sphere of radius r_{eff} with a distance between the cover-glasses surface equal to $2h$, is given by:

$$\gamma = \frac{6\pi\eta r_{eff}}{[1 - 1.004(r_{eff}/h) + 0.481(r_{eff}/h)^3 - 0.21(r_{eff}/h)^4 - 0.169(r_{eff}/h)^5]} \tag{4.18}$$

Two kind of chambers have been used to know how the distance between walls affect the drag coefficients. The "regular" chamber with a thickness around 180 μm − 200 μm and the "special" chamber, designed to avoid the convection with the changes of temperature (Section 4.5.4), which has a thickness around 110 μm.

In a chamber of approximately 110 μm of the thickness, the effective radius of the bead changes by 4-5 % in x-axis and 3-4 % in y-axis (Fig. 3.24). These results tell us that there is a difference in the calibration factor for the y-axis around 4 % depending on the thickness of the chamber.

As described in references [56, 58], the calibration of a momentum-flux force sensor depends on the sensitivity of its PSD photodetector. In our instrument, both the fluidics chamber and the silicon PSD cool to 4°C when the instrument head is inside of the icebox.

Therefore we did an experiment to measure the Stokes drag force on our calibration beads in cold conditions (4°C water, heating laser off). We found that the PSD reading increased by a factor of 1.69 over the case where the PSD and water were held at room temperature (25°C). However literature values [68] show the viscosity of water increases by a factor of 1.76 between those two temperatures. Therefore the momentum sensor under-reported the test force by 4% of reading at low temperature, consistent with such a reduction in PSD sensitivity. Thus the force calibration must be corrected by +4% for cold experiments compared to hot experiments, regardless of the state of the heating laser, which does not affect the PSD.

4.6 Unzipping experiments

4.6.1 Synthesis of the the molecular construction

The molecular construct used consists of a long DNA stem, extracted from λ-DNA (New England Biolabs) of 6838 bp [14] with a tetraloop at the end of the hairpin. To isolate the piece of the DNA of our interest is done a digestion of the λ-DNA phage with the restriction enzyme BamHI. The target of the BamHI (New England Biolabs) restriction enzyme is 5-GGATCCC-3. This one cleaves the λ-DNA in different points. However the target of our interest is between the bases 41732-48502 that is used as the stem of the DNA hairpin (the cosR end). The DNA stem, the two handles of 29 bp [44] and one tetraloop (3-ATCA-5) are ligated to the cosR end and the previously modified BamHI end. The function of the tetraloop is to avoid the separation of the two strands after unzipping the double helix. To assemble the tetraloop, a self-complementary oligonucleotide, which forms a tetraloop in one side and a cohesive BamHI end at the other, is ligated to the BamHI end of the DNA construction. To construct the DNA handles, an oligonucleotide (previously modified with several digoxigenins by using DIG Oligonucleotide Tailing Kit, 2nd Generation, Roche) is hybridized with a second 5 biotin-modified oligonucleotide (Fig.4.25).

This DNA construction is complementary to cosR end and to two identical 29 nucleotide long ssDNA at the other end. The two ssDNA are hybridized with a third oligonucleotide (SPLINT) which is complementary to them resulting in two dsDNA handles. These handles are attached to the DNA construction by a ligation reaction. The sample is kept in a buffer of 10 mM Tris-HCl and 5 mM EDTA.

4.6.2 Methodology of unzipping experiments

The unzipping experiments have been carried out using a DNA molecular construction of 6838bp described in the previous section. A tetraloop (5-ACTA-3) was attached at the end of the DNA molecule to avoid separation of the two strands.

The DNA molecules are attached to two beads through DNA handles of 29bp each [44]. One handle is functionalized with biotin and the other with digoxigenin. To unzip DNA, the DNA construction is attached to two polystyrene beads. One bead is covered in Streptavidin (SA) (G.Kisher GbR, ϕ=2.0-2.9 μm). The SA bead bonds to the biotin-labeled handle of the molecular construction. The other bead is a protein G microsphere (Spherotec, Lybertiville; ϕ=3.0-3.2 μm) coated with antidigoxigenin (AD) (Roche Applied

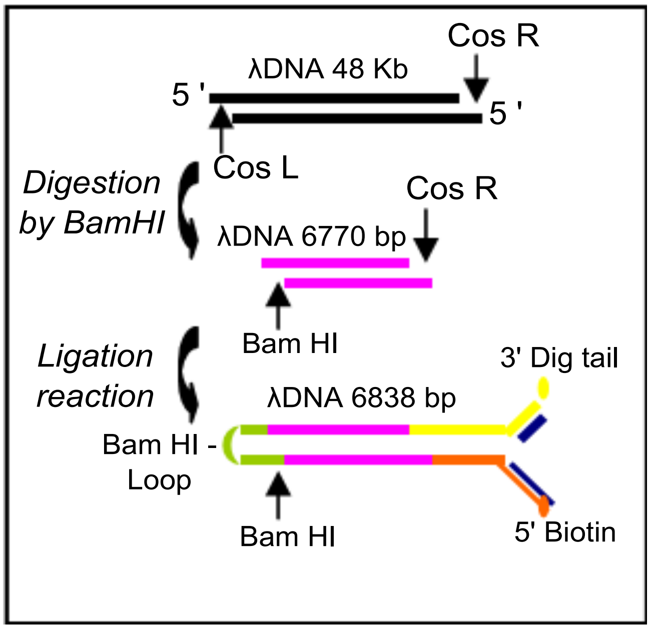

Figure 4.25: *Synthesis of the 6.8 kbp molecular construction.*

Science) antibodies. The AD bead bonds to the digoxigenin labeled handles. To facilitate the bonding between the hairpins and the AD beads, they are incubated together for 15 min in a TE buffer solution.

The micro-fluidic chamber is placed in a frame which is fixed between the objective lenses of the mT. The microfluidic chamber contains three channels. The *bottom* channel contains the SA beads and the *top* channel contains the AD beads. The *middle* channel contains the buffer where the experiment will be carried out. The beads arrive to the *middle* channel through the dispenser tubes. The methodology for an experiment is shown in Fig.4.26. The optical trap is used to trap the beads coming from the *dispenser* tubes. First the SA bead which is then fixed in the micropipette by air suction. Second the AD bead which is moved along side of the SA bead. Finally, the beads are brought close to each other, by moving the optical trap or by moving the chamber, until the connection of the hairpin and the two beads is created.

The experiments of NaCl were carried out in a buffer of pH 7.5 (Tris 10 mM, EDTA 1 mM) and varying concentrations of NaCl (1 M and 100 mM). The experiments of $MgCl_2$ were carried out in a buffer of pH 7.5 (Tris 10mM) and varying concentrations of $MgCl_2$ (10mM and 1mM).

4.6.3 Unzipping curves

DNA unzipping experiments are carried out by increasing the force applied to the strands of the molecule. When the applied forces reach a critical value the base pairs of the molecule are disrupted creating the characteristic sawtooth pattern seen in the Force Distance curves (FDCs)(Fig. 4.27). This pattern is composed of peaks of different shapes and sizes [69, 14]. The sawtooth pattern is related to the sequence of the hairpin. Each slope corresponds

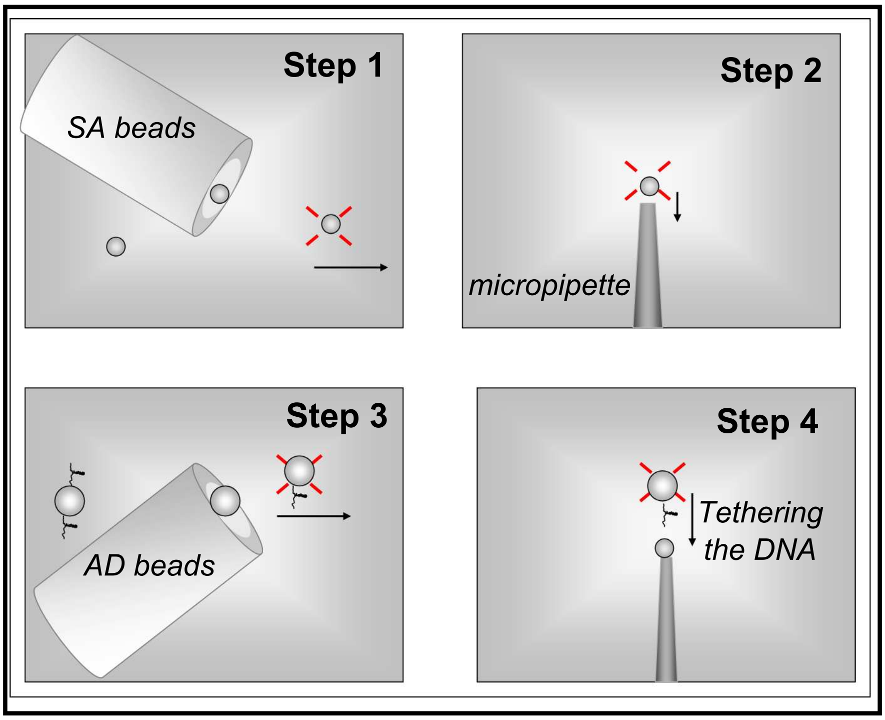

Figure 4.26: *Experimental methodology to carry out the formation of the DNA attachment between the two beads in the microfluidic chamber. Step 1) Trapping the SA bead; Step 2) The SA bead is immobilized by air suction in the tip of the micropipette; Step 3) Trapping the AD bead and Step 4) Creating the union between both ends of the molecule and the two beads.*

to the elastic response of the ssDNA when the molecule is being opened. When a group of basepares are opened, the tension is relaxed and the force drops. When the molecule is fully unzipping, the elastic response to the ssDNA is shown at the end of the curve.

The procedure to measure the FDCs consists of the following steps. First, a hairpin is tethered between the two beads, one immobilized in the tip of the micropipette and the other in the optical trap. Then the AD bead is moved away from the SA bead at a constant pulling speed of 50 nm/s (this speed is variable). The separation of the two beads pulls the molecule apart and the FDC is measured (Unzipping). Next we bring the two beads back together at the same speed as before and measure the rezipping forces.

To find the length of the molecule it is necessary to subtract the elastic contribution of the optical trap. In this range of forces the conversion between Force-Distance curve (FDC) and Force-Extension curve (FEC) is done by assuming that the optical trap can be approximated by a linear spring. The measured FDCs are then converted to FECs by correcting for the trap stiffness:

$$x = x_{TOT} - \frac{f}{\kappa} \tag{4.19}$$

Where x_{TOT} is the measured distance, f is the force and κ is the stiffness of the trap. The stiffness of the trap is around 0.07 ± 0.005pN/nm. After the resulting FEC conversion,

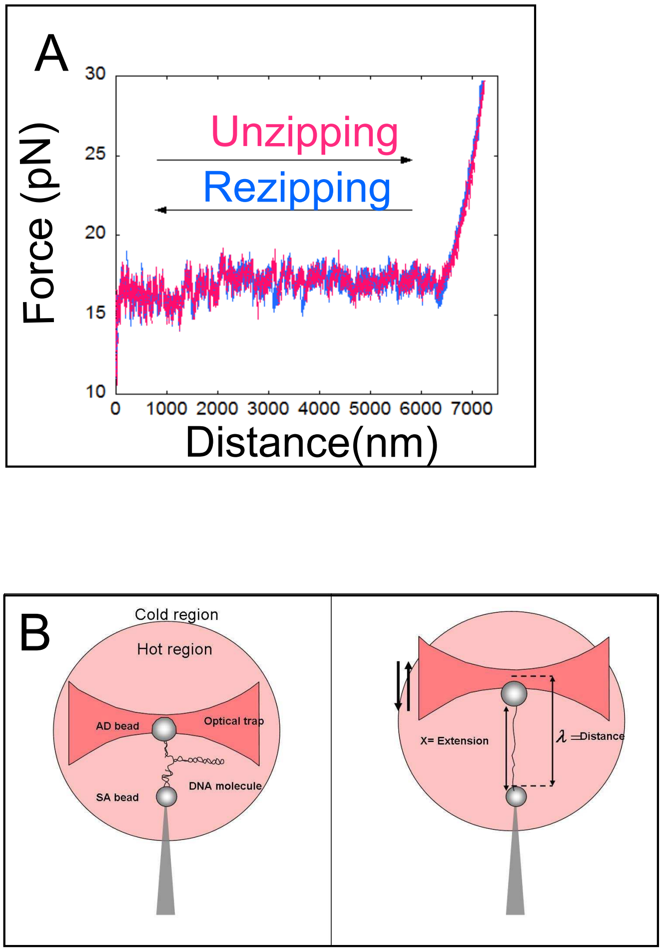

Figure 4.27: *A. Force-distance curves (FDC) at 1M NaCl + TE pH 7.5 measured at 25 C. Unzipping and rezipping traces are almost identical. B. Schematic representation of the unzipping experiments. The light red hot region corresponds to the region heated by the heating laser. The white cold region is the ambient temperature, inside or outside of the icebox.*

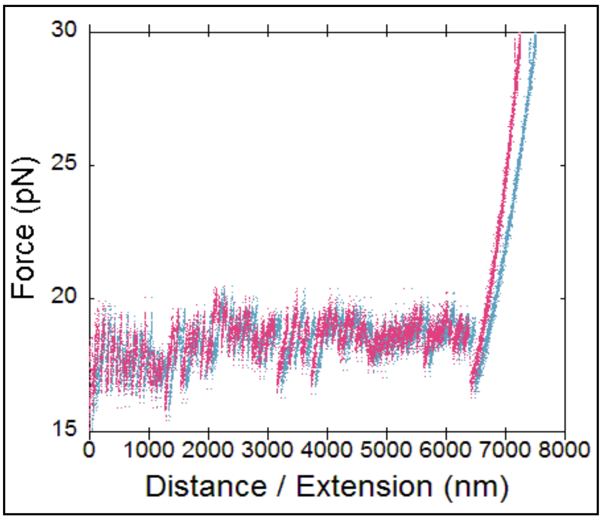

Figure 4.28: *Conversion of FDCs (blue lines) into FECs (pink lines) for a 6.8kbp dsDNA molecule at 13C.*

each trace is aligned by using the reference point (x,f) = (0,0) or at least forced to pass through the point where the two beads touch (Fig.4.28).

4.6.4 Single-Stranded DNA curve: oligonucleotide method

As a part of the experimental methodology, this section will explain how we create the ssDNA used in the unzipping experiments.

To study ssDNA at different temperatures, we have used the *oligonucleotide method* to obtain ssDNA. The *blocking oligo* is a oligonucleotide of 30 bp complementary with the loop which after binding to it prevents the formation of the secondary structure when the force in the hairpin is released. Bosco, et.al [40] carried out the study of the necessary oligonucleotide concentration to avoid non-specific binding of the oligonucleotide to the ssDNA. In our experiments we have used a concentration of 10 nM oligo blocking at high salt concentration (1 M NaCl).

Once the molecule is fully unzipped, a force of 40 pN is maintained on the molecule to prevent rezipping. Next, a fluidics system valve is opened and the buffer with the oligonucleotide is flowed into the central channel of the microchamber. Once the oligonucleotide binds to the loop, the molecule is prevented from rezipping again and the elastic response of ssDNA measured (Fig.4.29).

4.6.5 Theoretical models used to analyze ssDNA

The elasticity of DNA plays an important role in biological processes such as transcription when a particular segment of DNA is copied into RNA by the polymerase enzyme.

During the last two decades experiments exploring the elasticity of DNA have been done using various single molecule techniques [30, 31, 35, 74, ?]. During such time, several

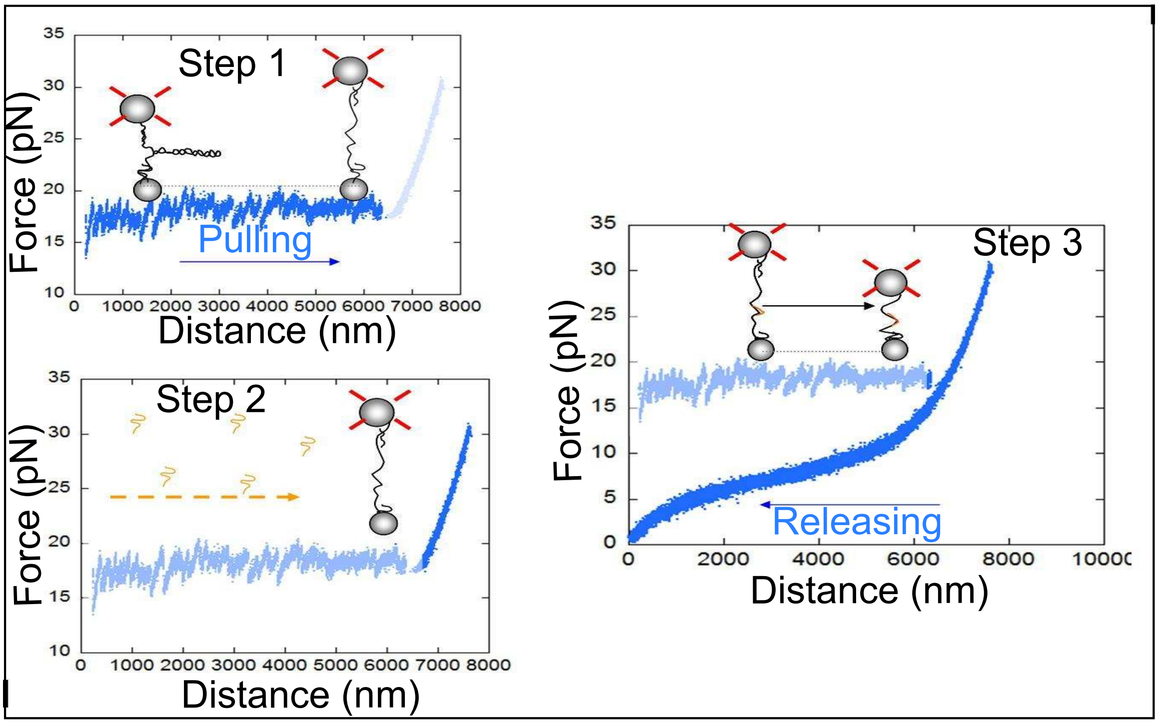

Figure 4.29: *Steps of the oligo protocol used in the experiments to obtain ssDNA.*

theoretical models have been developed to describe the elastic behavior of DNA. In this section a brief summary of some of these different models used to characterize the elasticity of the DNA and their limitations is provided.

A simple way to explore DNA elasticity is to stretch a single molecule from both ends, measuring the force f as a function of its end-to-end distance. Best known models are the Freely Jointed Chain (FJC) and the Worm Like Chain (WLC). These models were originally developed as general polymer theories and in recent years have been applied to the study of the elastic properties of single biomolecules.

The FJC model considers a biomolecule as a chain formed by N segments. Each segment, called Kuhn length, has a length l_K. In this model the direction of a segment is uncorrelated with the direction of adjacent segments. An important parameter in this model is the contour length L_0 defined by $L_0 = Na$, where a is the effective interphosphate distance. The FJC theory shows elastic behavior that is purely entropic. Entropic elasticity is observed at low forces, when the configuration of the molecule changes by the thermal fluctuations with almost no contribution by enthalpic stretching. The elastic response is given by:

$$x(f) = L_0 \cdot (coth(\frac{l_K f}{k_B T}) - \frac{k_B T}{l_K f}) \tag{4.20}$$

where x is the extension, f is the force applied to the end of the polymer, k_B is the Boltzmann constant and T the temperature.

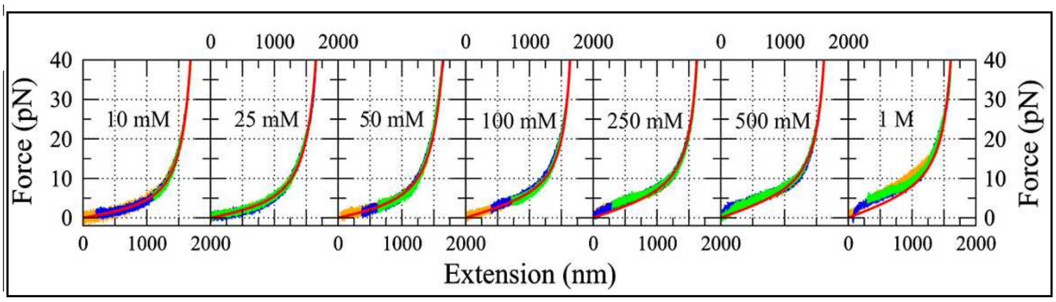

Figure 4.30: *Figure from the article by Huguet.et al, [14] demonstrating the elastic response of a 3 kb ssDNA molecule at various salts. Raw data of three molecules are shown (orange, green and blue curves). Red curve shows the best-fit to the elastic model.*

An alternative is the WLC model which provides a better representation of stiff polymers such as double-stranded DNA, actine fibers and microtubules. In the WLC model, the polymer is represented by a continuous flexible rod that can be described as a bending modulus of a persistence length l_p. The other important parameter is the Contour Length (L_0) that determines the length of the polymer chain. A force-extension interpolation can be derived as:

$$f(x) = \frac{k_B T}{4l_p}[(1-\frac{x}{L_0}) - 1 + 4\frac{x}{L_0}] \tag{4.21}$$

where f is the force applied to ends of the polymer, x is the molecular extension, k_B is the Boltzmann constant and T the temperature.

One might think that the elastic parameters of ssDNA are easily described, however this is not the case. As shown by Huguet et al [14], the elastic parameters depend on the buffer used. In his analysis from the unzipping experiments on the ssDNA the WLC model describes the elastic response of ssDNA at low salt concentration (<100 mM [NaCl]) better than the FJC model does. However at higher salt concentrations (>100 mM [NaCl]) the FJC model works better. At low forces (<10pN) both models fail because the ssDNA exhibits a force plateau which indicates that ssDNA produces non-specific secondary structures (self-hybridation).

Alternatively Smith et al [35] suggested that the FJC or the WLC are incomplete and proposes the possibility that DNA could be deformed under stress. The FJC and WLC models consider DNA inextensible. However, it has been demonstrated that the deformation of each subunit adds an observable change in the molecular extension [35]. This model is known as Extensible Freely Jointed Chain($Ex - FJC$).

$$x(f) = L_0 \cdot (coth(\frac{l_K f}{k_B T}) - \frac{k_B T}{l_K f}) \left(1 + \frac{f}{K}\right) \tag{4.22}$$

where l_K is the Kuhn length and K is the stretching modulus.

Studies suggest that the Ext-FJC is the best model to fit the parameters at different ionic concentrations. For this reason we have chosen this model for our analysis.

Chapter 5

Results

The mT with TC is used to carry out DNA unzipping experiments at different temperatures and to measure the free energy, entropy and enthalpy of formation of the DNA duplex. The first section of this chapter explains how the average unzipping force changes with temperature. Moreover the experimental results have been compared with previous studies carried out at room temperature.

Force melting experiments have been used, in combination with Monte-Carlo techniques, to derive the salt and sequence dependent base pairing free energies in DNA. Here we discuss a simpler model and derive homogeneous (i.e. sequence independent) base pairs free energies in a range of temperatures between 5°C and 50°C. The homogeneous model yields a single base pairing free energy, which is an average of the base paring free energies of the different motifs. The base-pairing enthalpies and entropies have been measured too.

In the next section we are interested to resolve some questions about how the temperature affects the extension of ssDNA under applied temperature. First we want to elucidate whether the distance between consecutive base pairs does increase or decrease with temperature at a given force and by how much. This information will allows us to use the number of base pairs between consecutive peaks as a rule to convert base-pairs into molecular extensions at a given force. From the experimental unzipping data we have found that the distance between consecutive peaks at a given force varies depending on temperature. In order to know the elasticity of ssDNA at different temperatures, a full analysis of the of the FECs of ssDNA at varying temperatures has been carried out.

5.1 DNA as a local thermometer.

To demonstrate the capabilities of the temperature jump instrument, we carried out unzipping experiments of single DNA molecules at different temperatures in the range between 3°C to 45°C at 1M NaCl. The molecular construct we pulled consists of 6.8kb hairpin flanked by 29bp handles at both sides. In Fig.5.1 we show the force-distance curves (hereafter referred to as FDC) obtained during the unzipping process at various temperatures. We measured the average unzipping and re-zipping forces along the FDC at different temperatures finding negligible differences among the unzipping and re-zipping pathways, showing that the hairpin was unzipped under quasi-static or reversible conditions.

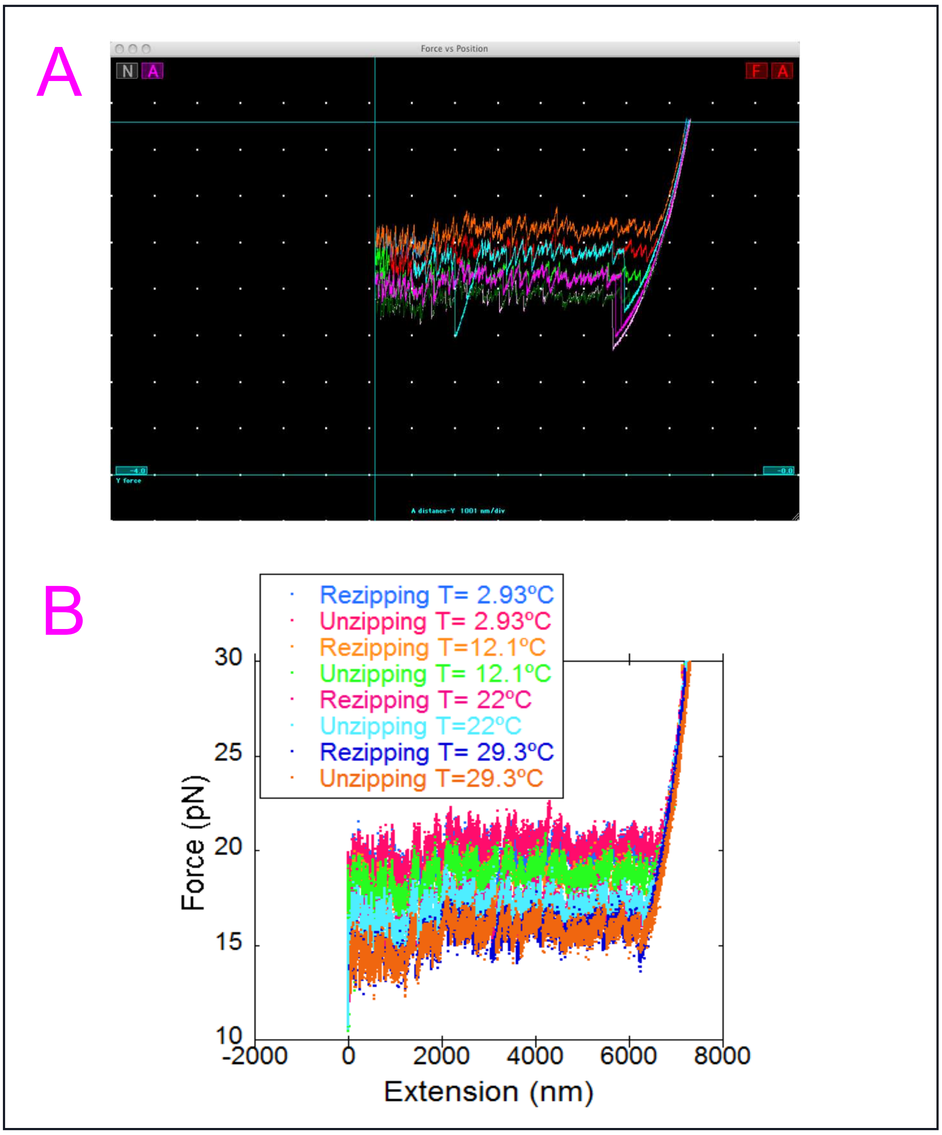

Figure 5.1: *Unzipping experiments at different temperatures. Force-distance curves (FDCs) at 1M NaCl + TE pH7.5 measured at 3° C, 12° C, 21° C and 29° C. A.Measurement in real time by using the lt program. B. Curves after the analysis. Unzipping and rezipping traces are almost identical.*

As it was explained in Williams et. al the stability of dsDNA with respect to ssDNA, set by the free energy difference $\Delta G(T)$, is strongly dependent on T. This happens because ssDNA is a highly flexible polymer and its entropy is higher than the entropy of a more rigid polymer like dsDNA. Increasing T reduces the stability of dsDNA and promotes the melting process. By measuring the mean unzipping/re-zipping force for different molecules and for different temperatures it has been observed that the average force decreases linearly with the temperature (See Fig.5.2). This is explained by the entropic contribution to the free energy of formation of the double helix which destabilizes the double helix upon increasing the temperature.

The slopes of the unzipping and re-zipping forces vs temperature are the same, suggesting that the system is in equilibrium. Moreover as it was described in section 4.2 there is a difference of 4% in force between cold and hot measurements, in this case the cold measurements have been aligned to the hot segments (where the PSDs operate at room temperature). For each molecule, the temperature has been measured and analyzed following the protocol described in Section 4.5.1. Moreover the zero force baseline has been corrected for each trace. Using a simulation program to reproduce the unzipping experiments (Appendix I), we predicted the change of the average unzipping/rezipping force versus temperature (Fig.5.2). This simulation uses the nearest-neighbor base pair free energy values (ΔH and ΔS) predicted in ref [6] (Unified Oligonucleotide UO- values) and those reported from unzipping experiments (HU values) in [14]. The parameters for the ideal freely jointed chain (FJC) model where taken from [14]. In Table 5.1 the mean forces for each condition at 6 different temperatures are shown. The experimental measurements of the forces are in agreement with the theoretical predictions at room temperature with a difference in the mean force of 2%. However below room temperature the discrepancy between the experimental results and the theoretical values predicted by HU is around 4%. This is not the case with the prediction of UO values that show a difference of approximately 1%. In contrast, at high temperatures, the discrepancy between the experimental results and the theoretical predictions is larger for the UO values by showing a discrepancy around 3%.

Experiments were conducted in different buffer solutions 1 M NaCl, 100 mM NaCl, 10 mM $MgCl_2$ and 1 mM $MgCl_2$ (Fig. 5.3). At 25°C the unzipping forces are almost the same at 1 M NaCl and 10 mM $MgCl_2$. The same effect is observed for the solutions 100 mM NaCl and 1 mM $MgCl_2$. This shows that the average unzipping force follows the rule 1:100 between monovalent and divalent salt as discussed in [76] for the RNA case. The mean unzipping force is expected to vary proportionally to the logarithm of salt concentration, however a hundred fold concentration of Na_+ is required to achieve the same unzipping force as compared the Mg_{2+} case indicating strong non-ideal effects in the binding affinity of counter-ions and co-ions to DNA in solution.

Figure 5.4 shows an unexpected effect: the re-zipping force extension curve follows a ssDNA trajectory below the unzipping force. The compaction of ssDNA is apparent in the force shoulder that extends over the range 5-10 pN. This shoulder indicates the formation of secondary structures stabilized by lowering the temperature and increasing the salt. This effect on the ssDNA has been observed in previous works [35, 77] and recently quantified for a wide range of monovalent and divalent ionic concentrations [40].

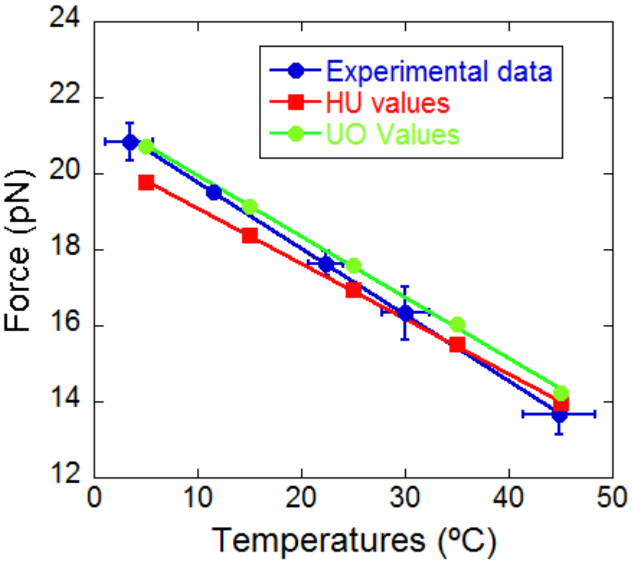

Figure 5.2: *Relation between the mean Unzipping/Rezipping Force and the temperature. Experimental data combined with two theoretical predictions in a range of temperatures between 5° C and 50° C. Experimental data (blue points) show the mean forces for 4 molecules in cold and hot measurements, measured at 1 M NaCl TE pH7.5. The error bars show the standard deviation between them. The red squares and green circles show the theoretical predictions from unzipping experiments (HU values, taken from Ref. [14]) and from melting experiments in bulk (UO values, taken from Ref. [6]), respectively, at five temperatures: 5° C, 15° C, 25° C, 35° C and 45° C.*

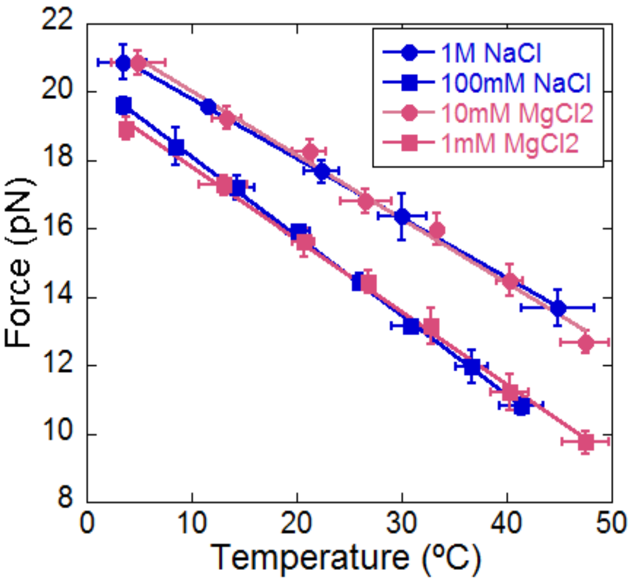

Figure 5.3: *Dependence of mean Unzipping/Rezipping Force with temperature in different ionic concentrations. Experimental data averaged over 8 molecules at 1M NaCl (blue circles), 100 mM NaCl (blue squares), 10 mM* $MgCl_2$ *(pink circles) and 1mM* $MgCl_2$ *(pink squares). These results follow the 1:100 rule between monovalent and divalent salt similar to what has been observed for RNA [76].*

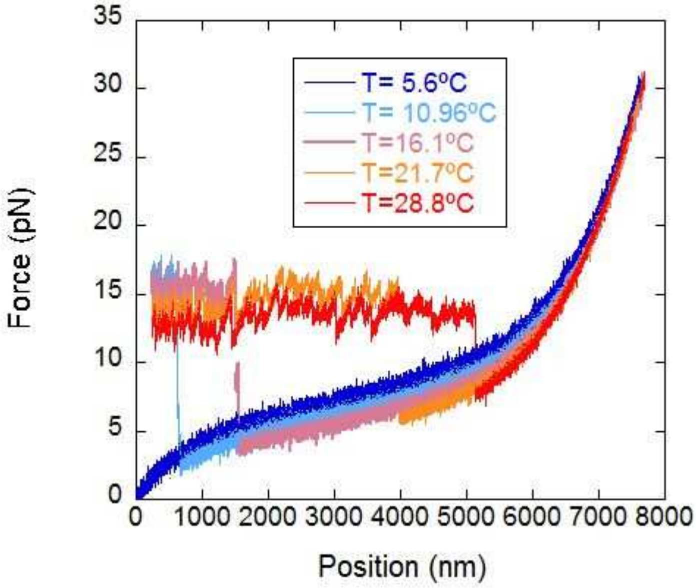

Figure 5.4: *Rezipping curves at 100mM NaCl + TE pH 7.5 at five temperatures:* 5° *C (Dark blue),* 11° *C (Light blue),* 16° *C (Purple),* 22° *C (Orange) and* 29° *C (Red). Rezipping traces show that low temperatures inhibit the formation of dsDNA kinetically trapping the single stranded form.*

Method	Temperature (°C)	Mean Force (pN)
Exp results	5	20.6
HU Prediction	5	19.8
UO Prediction	5	20.7
Exp results	15	18.9
HU Prediction	15	18.4
UO Prediction	15	19.1
Exp results	25	17.2
HU Prediction	25	16.9
UO Prediction	25	17.6
Exp results	35	15.4
HU Prediction	35	15.5
UO Prediction	35	15.9
Exp results	45	13.7
HU Prediction	45	14.0
UO Prediction	45	14.2

Table 5.1: *Relation between the mean Mean Force and the temperature. Experimental data combined with two theoretical predictions in a range of temperatures between* $5^{\circ}C$ *and* $50^{\circ}C$*. Exp results (Experimental results), HU Prediction (Prediction done by Huguet.et.al), UO Prediction (Unified Oligonucleotide done by Santa Lucia.et.al). The mean values of the experimental results were obtained after averaging over 8 molecules for 1M NaCl condition of salt.*

5.2 Average basepair free energies from force melting experiments.

Force melting experiments have been used, in combination with Monte-Carlo techniques, to derive the salt and sequence dependent base pairing free energies in DNA [14]. Here we discuss a simpler model and derive homogeneous (i.e. sequence independent) basepaire free energies at different temperatures to extract enthalpies and entropies. The average model yields a single basepair free energy number, which is the average of the basepair free energies of the 16 different NN motifs [14].

We approximate the typical sawtooth pattern of the FDC in unzipping experiments with a horizontal line corresponding to the mean unzipping force f_p (Fig.5.5). In the plateau region the extension of trap and molecular handles (x_T,x_h in Fig 5.5) is approximately constant so that the change in the trap-to-pipette distance when moving form λ_1 to λ_2 corresponds to the increase in ssDNA length (ΔX_{ss}) which is induced by the unfolding of n dsDNA basepairs, where $\lambda_2 - \lambda_1 = \Delta X_{ss} = n\Delta X_0$ is the length change induced by the unfolding of one basepair. The configuration of the experimental setup at two different distances is depicted in Fig. 5.5 (top, green circles). The area under the equilibrium FDC curve between the two distances is the reversible work, ($W = f_p\Delta\lambda$), necessary to bring the system from distance λ_1 to distance λ_2 (W corresponds to the area of the dashed

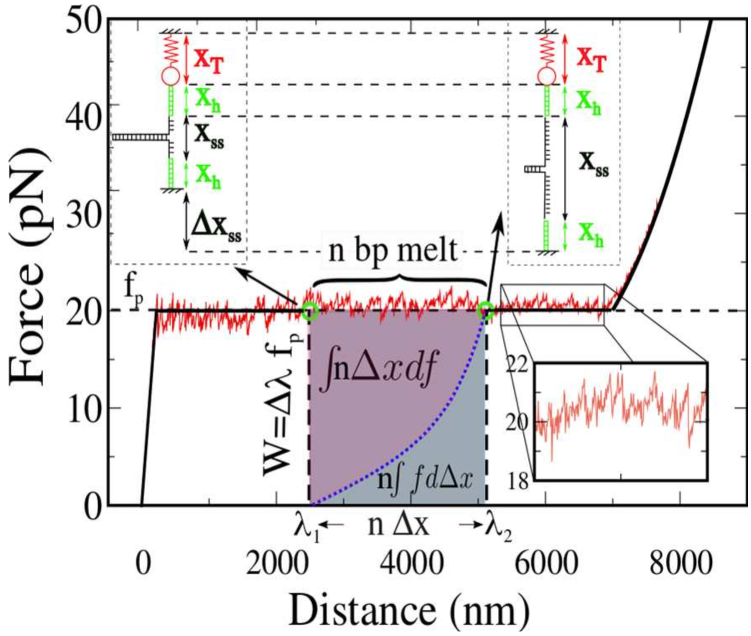

Figure 5.5: *Homogeneous base pairing free energies are obtained approximating the sawtooth pattern (inset) by a straight line corresponding to the mean unzipping force (f_p). The configuration of the experimental setup at two different distances (λ_1, λ_2) is shown above the FDC. The force is constant along the transition, so the extension of trap and molecular handles (x_T,x_h) does not change. Different distances correspond to different ssDNA extensions. The reversible work necessary to drive the system reversibly from λ_1 to λ_2 corresponds to the area enclosed in the dashed rectangle. In this transition n basepairs are unfolded, and the corresponding free energy change involves both the base pairing free energy and the free energy due to stretching 2n bases of ssDNA. The base pairing free energy can be recovered once the elastic contribution due to the stretching of such piece of ssDNA is subtracted from W (as detailed in the text).*

rectangle in Fig. 5.5).

This thermodynamic transformation will induce the unfolding of a given number, n, of basepairs. W equals the total free energy change ΔG, which is the sum of a contribution due to dissociating n basepairs $n\Delta G_0$ (ΔG_0 being the homogeneous base pairing free energy) and a contribution from stretching the ssDNA (this stretching free energy corresponds to the area below the dotted line in Fig.5.5, and corresponds to the FDC of 2n bases of ssDNA). Equating work and free energy change we get:

$$W = f_p \Delta\lambda = \Delta G = n\Delta G_0 + \int f dx \tag{5.1}$$

Integrating Eq.5.1 by parts and using the fact that $\Delta\lambda = n\Delta x$ (when $\Delta x(f)$ is the extension of one base at force f) gives:

$$n\Delta G_0 - \int_0^{f_p} \Delta x(f) df = 0 \tag{5.2}$$

or

$$n\Delta G_0 = \int_0^{f_p} \Delta x(f) df \tag{5.3}$$

This integration by parts can be understood geometrically as taking the difference between the area of the dashed rectangle and the area under the dotted curve in Fig.5.5. This is shown as a purple region in Fig. 5.5. According to Eq.5.3 the homogeneous base pairing free energy can be computed from the integral of the force-extension curve of a single unfolded basepair equal to that at 2 single bases. In order to measure ΔG_0 it is thus necessary, besides measuring the mean unzipping force, to parametrize the temperature and salt dependent elasticity of ssDNA.

5.3 Analyzing the change in molecular extension upon varying temperature

In the previous section it was shown how the elasticity of ssDNA is important in determining the stability of the duplex form over ssDNA in force melting experiments. Equation 4.3 makes it clear that the precision measurement of base stacking free energies via melting experiments requires a detailed knowledge of the influence of force, temperature and ionic conditions on the extension of ssDNA.

The elasticity of ssDNA can be measured from the unzipping pattern. In order to do this we took advantage of the simulation program (Appendix I) that gives the number of base pairs corresponding to the different force peaks observed along the sawtooth pattern (Fig.5.6). From the experimental unzipping data we can measure the distance between consecutive peaks at a given force and a given temperature. Just as in the analysis of the plateau, the distance between peaks at a given force is due to the difference in ssDNA extension. The ratio between the measured distance and the number of basepairs between peaks gives the extension of ssDNA per basepair (Δx). This is a differential extension measurement: it is based on the measurement of differences in trap position. As a consequence, it avoids the systematic error associated with the definition of the zero in absolute distance or molecular extension measurements. In single-trap setups the zero of extension measurement is difficult to determine precisely: a significant uncertainty is due to the fact that the molecule can be attached anywhere on the surface of the immobilized bead. Figure 4.7 shows unzipping traces for one molecule at two different temperatures (5°C and 29°C). After correcting the effect of experimental drift on the traces, we observe how the unzipping pattern shrinks as the temperature is raised (two horizontal black arrows in Fig.5.7) meaning that the ssDNA extension at the unzipping force changes with temperature. Repeating this measurement for different temperatures it is possible to determine the molecule's length change between the helix and the coil state (Δx) and how this parameter varies with temperature. Figure 5.8 shows the distance between base pairs plotted versus temperature. Experimental unzipping results show how Δx decreases by increasing temperature. It must be noted that, as it has been shown in the Fig.5.2, the average unzipping force does also decrease when increasing temperature. Consequently the change shown in Fig.5.8 is the combined effect of a change in force and temperature.

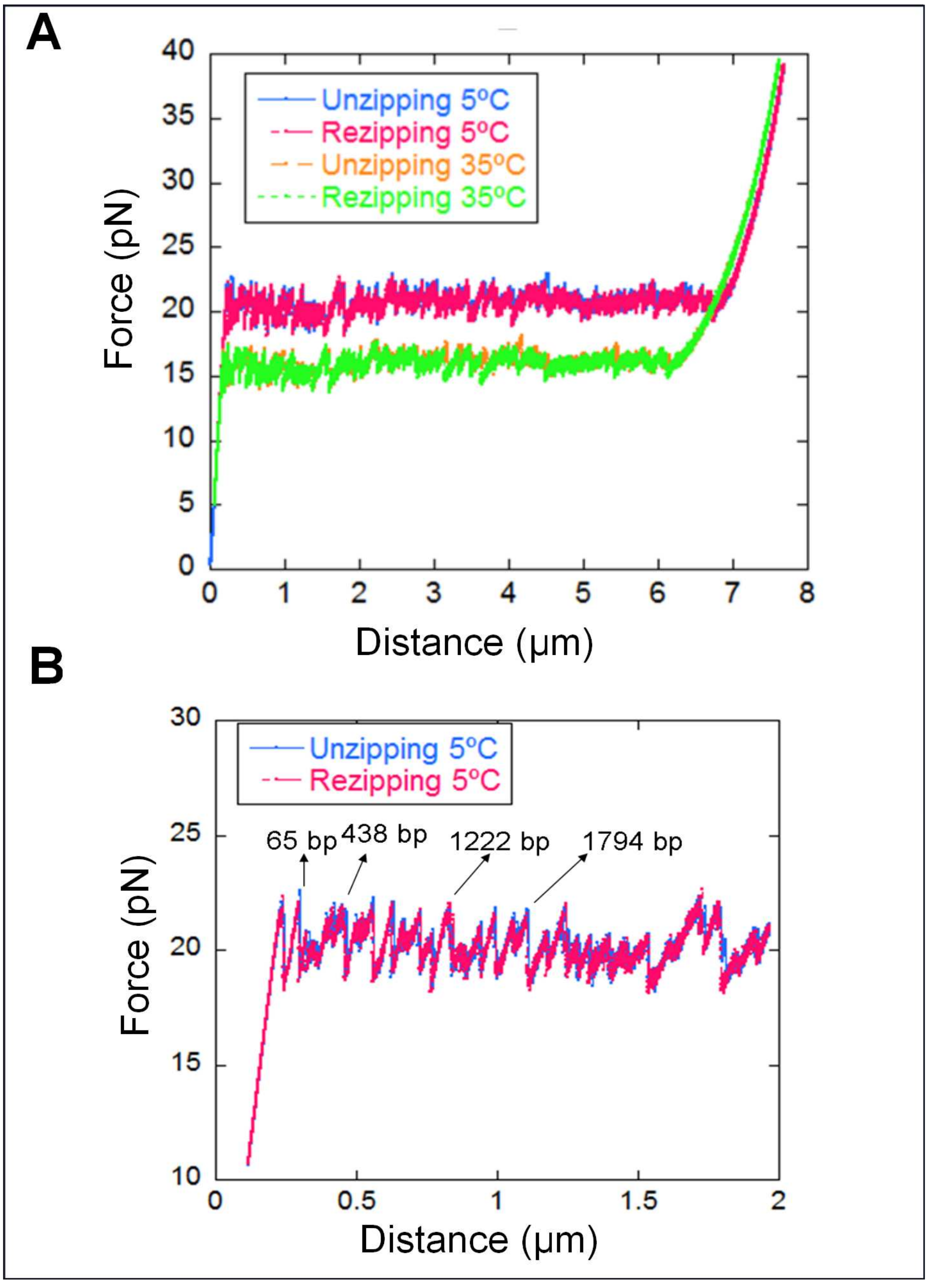

Figure 5.6: *Simulation of the unzipping experiments at different temperatures. A. This graph shows a full cycle of a unzipping/rezipping experiments of of λ-DNA (6.8 kbp) at two different temperatures. This simulation uses the nearest-neighbor base-pair free energy values (ΔH and ΔS) predicted in ref [6] (Unified Oligonucleotide UO- values). The parameters for the ideal freely jointed chain (FJC) model where taken from [14].B. Zoom for the first 2 μm of lambda DNA (6.8kb). The numbers in the different peaks correspond to the number of bases that are opened in each moment. If we are interested no know the number of bp we need to divide the number of bp by 2.*

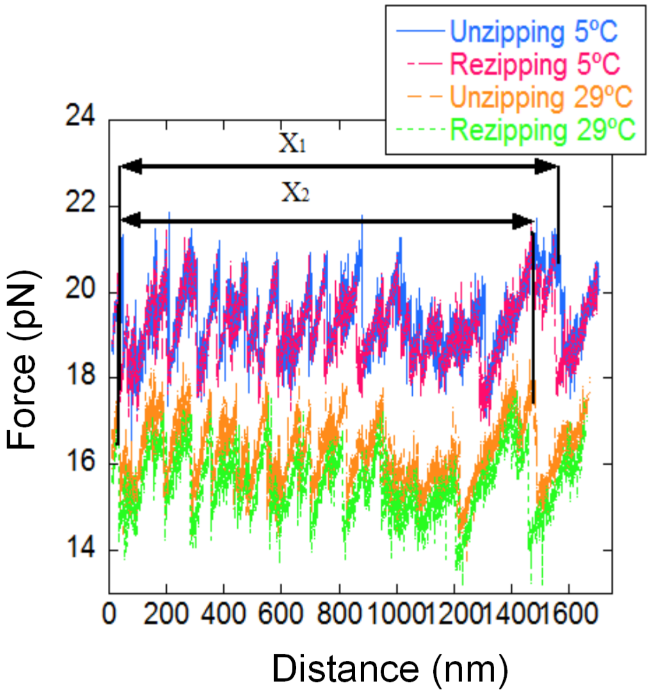

Figure 5.7: *Dependence of the molecular extension of ssDNA on temperature and force. This graph shows the first 2 μm of the unzipping/rezipping traces for a given molecule at 5° C and 29° C. By measuring how the distance between different peaks along the FDC changes with temperature we can determine how the molecular extension of the hairpin does change with temperature and force.*

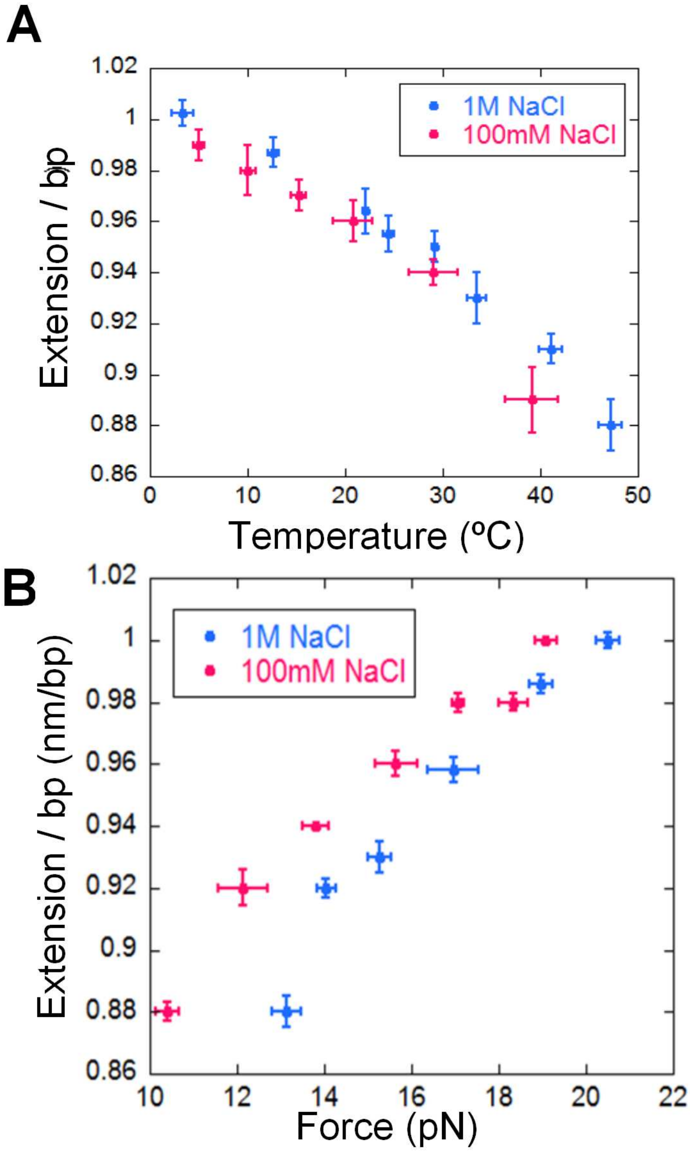

Figure 5.8: *Dependence of the molecular extension of ssDNA on temperature and force. A. Extension/bp vs Temperature. Results were averaged over 4 molecules in buffer solution of 1 M NaCl and 100 mM NaCl. Although the distance between base pairs does change with temperature, it does not appreciably change when varying salt concentration. B. Extension/bp vs Force. Results were averaged over 4 molecules in buffer solution of 1 M NaCl and 100 mM NaCl. The distance between bases changes with F in both conditions.*

In order to disentangle the effect of force from that of temperature in the previous measurements, we carried out a second set of measurements following the experimental methodology developed in [40]. After the DNA hairpin has been completely unzipped a 30 bases oligo that selectively binds to the loop region of the DNA hairpin is flowed in the fluidics chamber blocking the re-zipping. The oligo-bound molecule is kinetically trapped in the ssDNA form. This method allows us to measure the FDC of the ssDNA up to low forces, where the duplex form would otherwise be preferred. Fig.5.9 shows the FDC of one ssDNA molecule obtained with the method of the blocking oligo measured at various temperatures in the range $5-25°C$. A shoulder is observed at low forces (<10 pN) due to non-specific secondary structure formation. As it was described in [35, 14, 40] this plateau is observed at low forces (<10pN) and high salt (>100mM). The effect of temperature on this plateau is clearly distinguishable (Fig.5.9): the height of the plateau becomes higher at lower temperatures.

In order to parametrize the elasticity of ssDNA at different temperatures an elastic model must be adopted. As it has been explained in section 4.6.5, commonly used models to investigate the elastic properties of the ssDNA are the Extensible Freely-Jointed Chain (Ext-FJC) model where the Kuhn length (l_K) is the parameter to determine, or the Worm-Like Chain [31, 74] where the elasticity is governed by the persistence length (L_p). Earlier studies ([14, 77, ?]) suggest that the Ext-FJC is the best model to fit the parameters at different ionic concentrations, so that we chose this model for our analysis. The Ext-FJC model considers the molecule as a chain formed by N rigid segments each of length l_K. The force-extension curve of the Ext -FJC model follows the equation given in the section 4.6.5:

$$x = L_c \left[coth(\frac{f l_K}{k_B T}) - (\frac{k_B T}{f l_K}) \right] \left(1 + \frac{f}{K} \right) \tag{5.4}$$

where L_c is the contour length ,l_K is the Kuhn length and K is the stretching modulus. The value of L_c is known by fixing the contour length of the molecule to 0.57 nm/bp as in [40]. The total contour length is thus $L_c = N.a$=7857 nm where a is the crystallographic length for a hairpin of 13650 bases. Equation 5.4 was fitted to the experimental FDC obtained at different temperatures. The fits were constrained with the data obtained from the peak-to-peak distance analysis and were performed in the force range 15-40 pN to avoid secondary structure formation. The results of the fits are shown in Figure 5.10. The Kuhn Length shows a linear dependence on temperature while the stretch modulus is independent of temperature (Fig. 5.10). Remarkably the change in Kuhn length is apparently compensated by the change in temperature (Fig 5.10.A inset), so that the ratio k_BT/l_K is constant in the temperature range we explored.

5.4 Characterization of the thermodynamic potentials

The parametrization of the temperature dependent elastic properties of ssDNA obtained in the previous section can be used to compute the integral in Eq.5.3 to derive the homogeneous base pairing free energy. Experimental measurements enter in Eq.5.3 both through the mean unzipping force f_p and the elastic parameters, the uncertainty in the former being the main contribution to the error on ΔG_0.

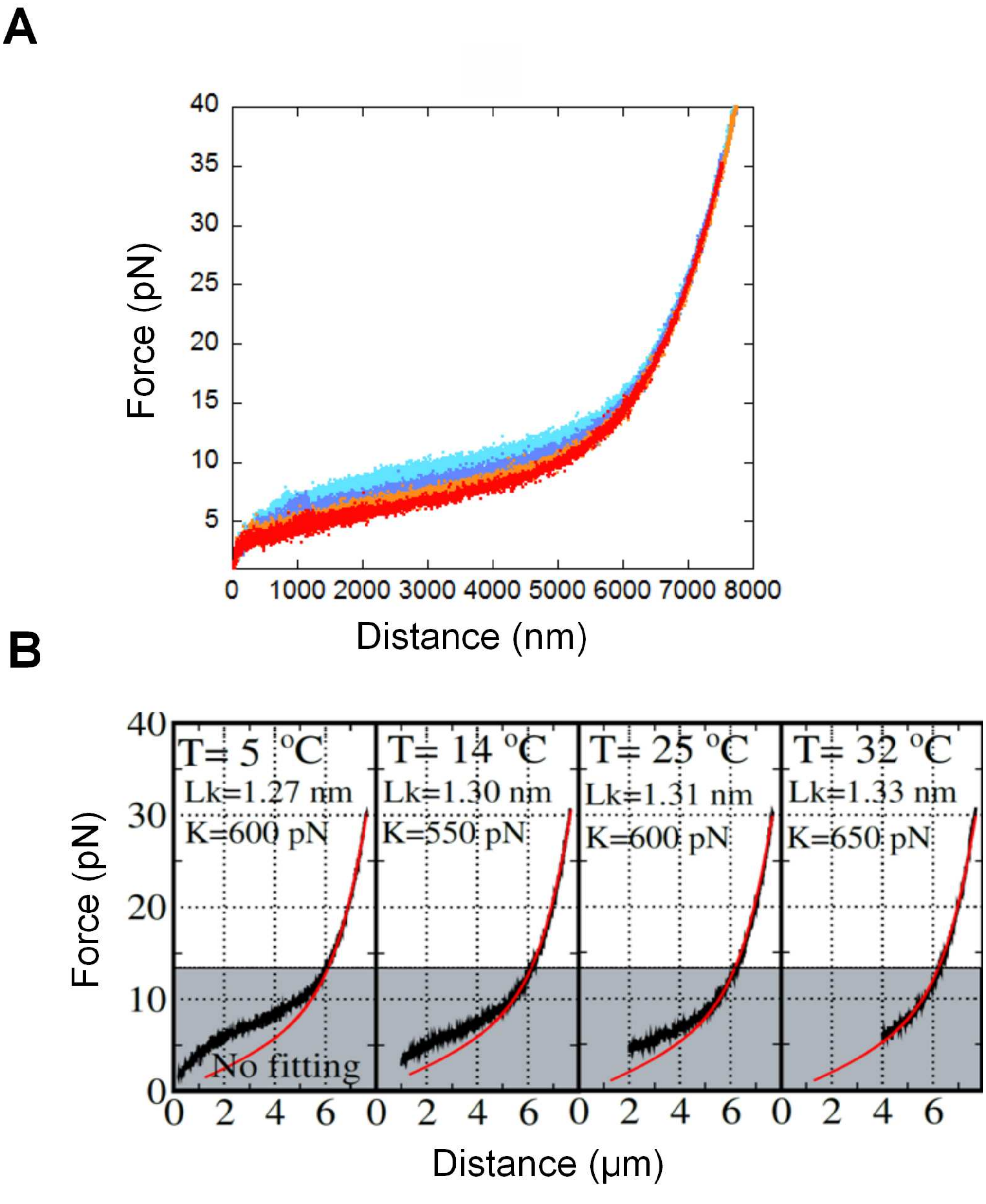

Figure 5.9: *Temperature dependence of the elastic response of ssDNA. A. Cycles of pulling and relaxing curves of ssDNA at four different temperatures (6° C, 16° C , 22° C, 26° C). The ssDNA was formed by using the oligo method [40]. B The theoretical fit has been done by using the Ext-FJC model. The experimental curves were taken at 1M NaCl, pH.7.5.*

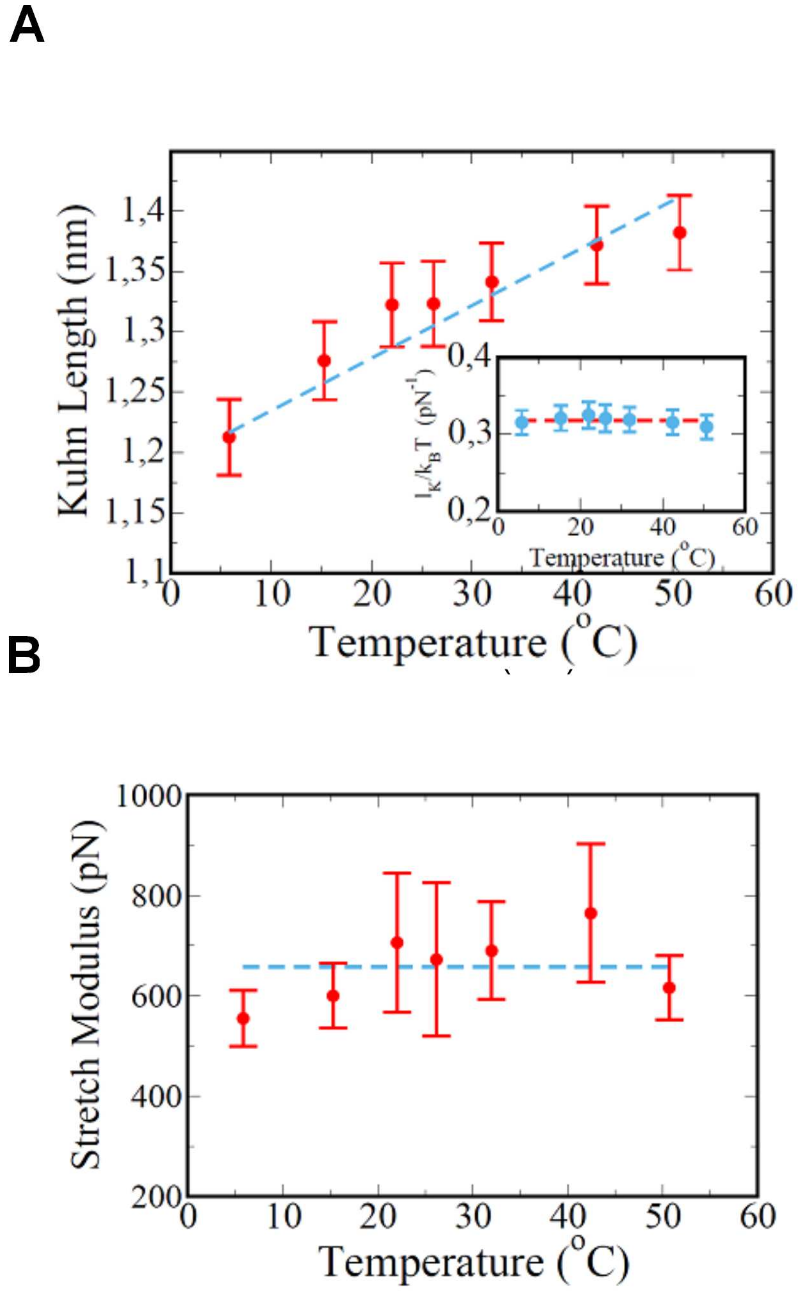

Figure 5.10: *Temperature dependence of single-stranded elastic response. A. Kuhn length values for ssDNA and different temperatures at 1 M NaCl. B. Stretching modulus values for ssDNA at different temperatures at 1 M NaCl. Blue points are the averages of measurements over 6 molecules at a given temperature.*

In Figure 5.11.A the ΔG_0 obtained from Eq.5.3 is compared to the average of the NN basepair free energies given by the UO and HU predictions. Interestingly, our results interpolate between the UO and HU values, being fully compatible with HU at room temperature. Similarly to what has been observed for the mean unzipping forces (Section 5.1) the measured free energies are in agreement with the UO values at low temperatures and with the HU values at high temperatures.

The thermodynamic stability of the DNA duplex is the result of a compensation of large and entropy (ΔS) and enthalpy (ΔH) terms:

$$\Delta G = \Delta H - T\Delta S \tag{5.5}$$

The TC setup allows for the experimental measurement of the entropy change (ΔS) and enthalpy change (ΔH) in the unfolding process. Along the transition line at constant force f_p, free energy change is zero:

$$\Delta G(f, T) = \Delta G_0(T) - \int_0^{f_p} \Delta x df = 0 \tag{5.6}$$

The entropy change, being the partial derivative of the free energy, gets a contribution from the basepair term, $\Delta S_0 = -\delta \Delta G_0 / \delta T$ and from the force dependent ssDNA stretching term $\Delta S_{elas} = \int -\delta \Delta x / \delta T df$.

$$\Delta S = \frac{-\delta \Delta G}{\delta T} = \Delta S_0 - \Delta S_{elas} \tag{5.7}$$

Calorimetric methods measure ΔS_0 so that, for a direct comparison of our unzipping measurements to bulk measurements, the total entropy change should be corrected to account for the force dependent term ΔS_{elas}. However, as discussed in the previous section, the ratio $k_B T / l_K$ being approximately constant (Fig.5.10.A, inset), the stretching contribution of ssDNA (as given by Eq.5.4 and the integral appearing in ΔS_{elas}) is slowly varying with temperature so that ΔS_{elas} can be neglected:$\Delta S \approx \Delta S_0$.

The entropy change ΔS can be derived directly from the Clausius-Clapeyron relation [31] (Appendix J). For the mechanical melting transition the Clausius-Clapeyron equation gives:

$$\frac{\delta f_p}{\delta T} = -\frac{\Delta S}{\Delta x}(f = f_p) \approx -\frac{\Delta S_0}{\Delta x}(f = f_p) \tag{5.8}$$

By neglecting S_{elas} this entropy change can be measured independently of the parametrization of the ssDNA elastic properties. Equation 5.8 combines the slope of the force versus temperature curve shown in Fig. 5.2, Fig. 5.3 with Δx measurements shown in Fig. 5.8. The force-temperature curves of Fig. 5.2 can then be used to compute predicted entropy changes also from the HU and UO values. Equation 5.8 implies that the difference in the measured entropy values is due to the different slopes of the lines shown in Fig. 5.3.

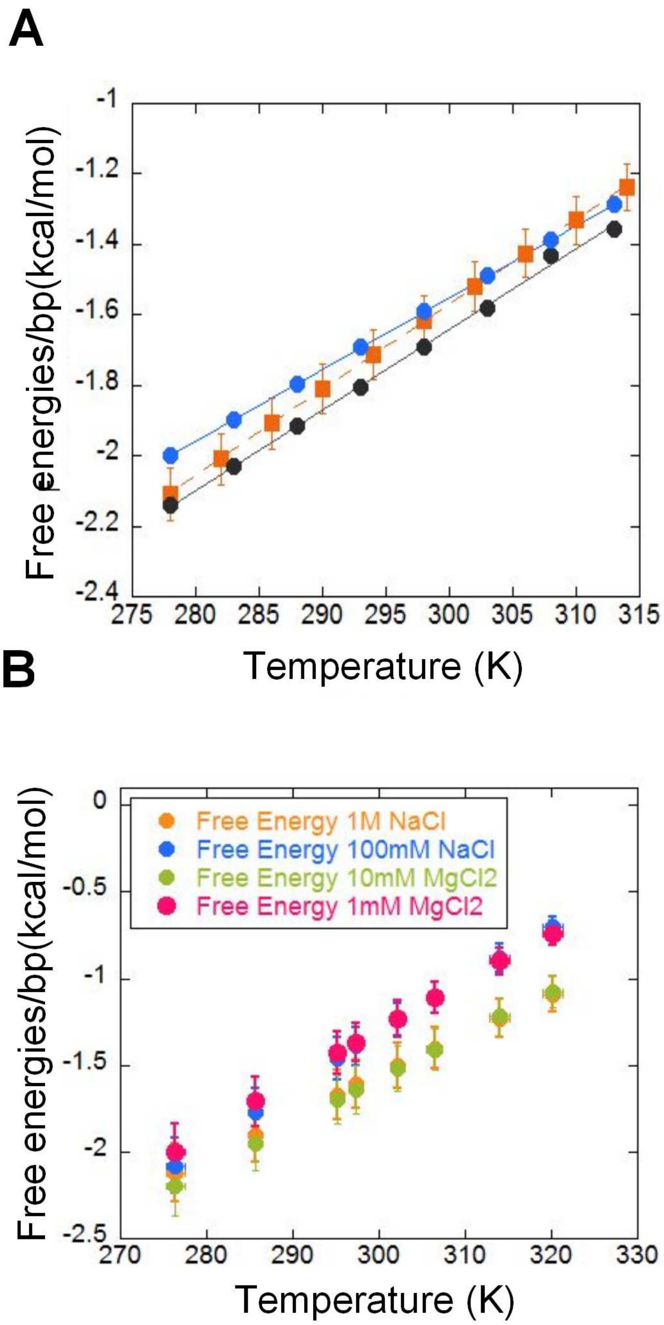

Figure 5.11: *Average base-pair free energy versus temperature derived from DNA unzipping experiments. A. Base-pair free energy and comparison with UO and HU predictions as a function of temperature at 1 M NaCl, pH 7.0. The orange squares show the experimental results calculated by fitting the elastic parameters. This was computed as described in Appendix J. The grey (blue) dots display the average UO (HU) values for the free energy/bp versus temperature. B. Base-pair free energies as a function of temperature at different salt conditions. Orange (1 M NaCl), Blue (100 mM NaCl), Green (10 mM $MgCl_2$), Pink (1mM $MgCl_2$).*

The measured free energy, entropy and enthalpy values are collected in Table.5.2 As far as free energy it is concerned, there is good agreement between our experimental values and those found in the literature [6, 14]. On the contrary measurements of entropy and enthalpy from [6, 14] do not agree with our results. It must be noted that in [6] the entropy was inferred from the free energy via melting temperatures measurements (always relying on the two-states assumption and inaccurate determination of the melting point) and the simulation developed by [14] use the melting temperature values too to extract the NNBP entropies and enthalpies. The development of the TC system give us the opportunity to obtain a direct measurement of the entropy and enthalpy change.

Mode	F(pN)	$\Delta x/bp$(nm)	$\Delta G/bp$(kcal/mol)	$\Delta S/bp$(kcal/(mol K))	$\Delta H/bp$(kcal/mol)
Exp Res(1M NaCl)	17.1(0.8)	0.95(0.06)	-1.61(0.15)	-23 (1.)	-8.5 (0.4)
HU Pred(1M NaCl)	16.9(0.8)	0.95(0.06)	-1.6(0.14)	-20(1.)	-7(0.4)
UO Pred(1M NaCl)	17.6(0.9)	0.95(0.06)	-1.7	-22	-8
Exp Res(100mM NaCl)	14.6(0.7)	0.94(0.04)	-1.38(0.11)	-31.(1.3)	-10.6(0.4)
HU Pred(100mM NaCl)	14.8(0.7)	0.94(0.04)	-1.3(0.14)	-20.(1.)	-8.(1.)
UO Pred(100mM NaCl)	-	0.94(0.04)	-1.42	-	-
Exp Res(10mM $MgCl_2$)	17.1(0.8)	0.95(0.06)	-1.6(0.14)	-26.(1.4)	-9.3(0.4)
HU Pred(10mM $MgCl_2$)	16.7(0.8)	0.95(0.06)	-	-	-
UO Pred(10mM $MgCl_2$)	-	0.95(0.06)	-	-	-
Exp Res(1mM $MgCl_2$)	14.6(0.7)	0.94(0.04)	-1.36(0.11)	-28.4(1.4)	-9.8(0.4)
HU Pred(1mM $MgCl_2$)	15.1(0.7)	0.94(0.04)	-	-	-
UO Pred(1mM $MgCl_2$)	-	0.94(0.04)	-	-	-

Table 5.2: *Table2. DNA thermodynamic potentials/bp. Comparison with theoretical predictions in different conditions (1 M NaCl, 100 mM NaCl, 10 mM $MgCl_2$ and 1 mM $MgCl_2$). Experimental data combined with two theoretical predictions in a range of temperatures between 276K (4° C) and 320K (47° C). Exp results (Experimental results), HU Prediction (Prediction done by Huguet.et.al [14]), UO Prediction (Unified Oligonucleotide done by Santa Lucia, et al [6]).*

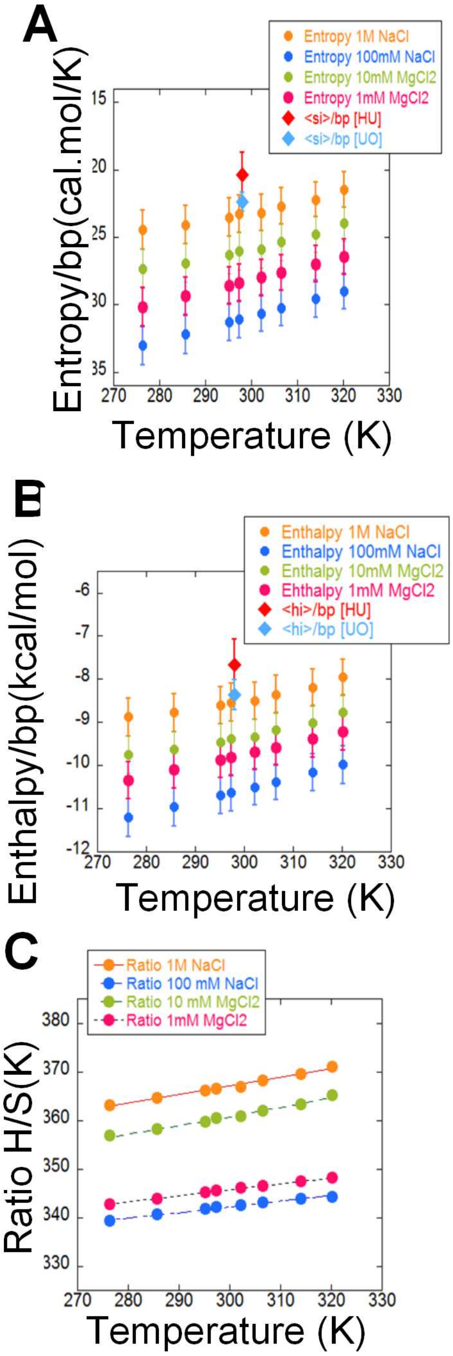

Figure 5.12: *Average base-pair entropy and enthalpy versus temperature derived from DNA unzipping experiments. A. Base-pair entropy as a function of temperature at different salt conditions. The analysis carried out using the Clausius-Clapeyron equation as described in the main text* $\frac{\delta F}{\delta T} = -\frac{\delta \Delta S}{\delta \Delta x}$ *where* ΔS *corresponds to the change in entropy accompanying to the change in extension* Δx*. In order to compare with the theoretical predictions we also show the average of the entropies of the 16 NN motifs at standard conditions (1M NaCl, 298 K for the UO (blue diamond) ([6]) and HU (red diamond) ([14]). B. Base-pair enthalpy as a function of temperature at different salt conditions. Same symbols as in B. In order to compare with the theoretical predictions we also show the average of the enthalpies of the 16 NN motifs at standard conditions (1M NaCl, 298K), for the UO (blue diamond) ([6]) and HU (red diamond) ([14]) C. Ratio between enthalpies and entropies as a function of temperature.*

Chapter 6

Conclusions

- In this thesis a high resolution optical tweezers instrument with temperature controller has been presented. The instrument covers a range of temperature between 5°C and 50°C. Following the strategy put forward in previous studies [43] we used a local heating laser to minimize the effects of instrumental drift. In this new instrument the wavelength of the heating laser has been chosen carefully to generate maximum heat in the bulk solution by infrared (IR) absorption and the focusing of the heating laser has been modified to avoid convection and to minimize the baseline shifts. With the improved instrument described in this thesis we have developed a temperature-jump optical tweezers with great thermal and mechanical stability. Four problems were identified for temperature control, that could not easily be solved with the laser method employed (a) they used 975nm light where water absorbs less so the temperature rise was only 6 degrees at full heating-laser power (b) localized heating made their buffer move upward by convection, at a rate of 8 μm/s in thick chamber and 2 μm/s in thin chamber (c) there is no way for a laser to make the buffer colder so all their work was done above room temperature (d) there were big baseline shifts because the heating laser was focused in a small spot to get maximum temperature rise. Following in the steps of Mao.et.al [43] we have tried to remediate these undesirable effects. In this thesis we have developed a temperature-jump optical tweezers with great thermal and mechanical stability.

- The viability of this temperature controller has been tested carrying out the thermodynamic characterization of the DNA helix formation by using Unzipping experiments at different temperatures. Several Force-Distance curves have been measured by changing the temperature, at different salt concentrations and at different ionic concentrations. According with the analysis, the mean unzipping/re-zipping force decreases with temperature. This observation can be explained by the entropic contribution to the free energy of formation of the double helix which is known to destabilize the double helix upon increasing the temperature.

- The instrument has been applied to measure the average basepair free energy $\Delta G/bp$ in a range of temperatures between 5°C and 50°C. This required the determination of the temperature dependent elastic properties of ssDNA, because the work of stretching ssDNA appears as a major contribution to the full reversible work measured along the unzipping FDC. Remarkably, we found that the persistence length of ssDNA does increase with temperature, at odds with the standard elastic rod model that predicts it should decrease inversely proportional to temperature. It is difficult to evaluate the full implications and generality of this result; however, it suggests that the elastic behavior of single-chain polymers (such as ssDNA, sRNA or polypeptide chains) is mostly determined by electrostatic effects.

- Throughout this paper we compared our experimental results with theoretical predictions given by the Unified Oligonucleotide (UO) energies [6] and unzipping (HU) values [14]. Our experimental results for the average basepair free energies agree with the theoretically predicted values (HU or UO) at room temperature. In contrast, the analysis of entropies and enthalpies has highlighted significant differences with respect to those predictions. This discrepancy should be attributed to systematic differences observed for the temperature dependent free energy above and below room temperature. In fact, below room temperature there is a discrepancy of around 4% between the experimental results and the theoretical values predicted by HU. This was not the case with the prediction of UO values that show a difference of approximately 1%. However, above room temperature the discrepancy between the experimental results and the theoretical predictions is larger for the UO values. These small but systematic discrepancies in free energy measurements translate into large discrepancies in the average entropy and enthalpy between our measurements and both UO and HU predictions.

- The temperature controller setup paves the way to a more detailed characterization of the thermodynamics of duplex formation in nucleic acids by deriving the ten unique nearest-neighbor basepair free energies, enthalpies and entropies at different temperatures from single molecule unzipping experiments. Until now this task has been only accomplished for basepair free energies by carrying out unzipping experiments at room temperature [14] but not for basepair dependent enthalpies and entropies which, in fact, could be derived only indirectly from existing melting data on short (10-50bp) oligos. However the possibility of controlling both force and temperature provided by this setup, makes it now possible to directly measure basepair dependent enthalpies and entropies at various temperatures. Additionally, our instrument may shed light on two long-standing issues in the field of nucleic acid thermodynamics: the measurement of the heat capacity change (and their temperature dependence) and a characterization of the entropy-enthalpy compensation across the melting transition.

Chapter 7

List of publications

- S. de Lorenzo, M. Ribezzi-Crivellari, S.B. Smith and F. Ritort.*A temperature-jump optical trap for single molecule manipulation.* Submitted for publication (2014).
- A.Alemany, N.Sanvicens, S. de Lorenzo, M.P Marco and F.Ritort. *Bond elasticity controls molecular recognition specificity in antibody antigen binding.* Nanoletters 13, 5197-5202 (2013).
- J.Camunas-Soler, S.Frutos, C.V.Bizarro, S. de Lorenzo, M.E. Fuentes-Perez, R.Ramsch, S.Vilchez, C.Solans,F.Moreno-Herrero,F.Albericio, R.Eritja, E.Giralt, S.B.Dev and F.Ritort. *Electrostatic Binding and Hydrophobic Collapse of Peptide-Nucleic Acid Aggregates Quatified using force spectroscopy.* ACS Nano 7, 5102-5113 (2013).
- K.Hayashi, S. de Lorenzo, M.Manosas, J.M.Huguet and F.Ritort. *Single molecule stochastic resonance.* Physical Review X, 2 031012 (2012).
- N.Forns, S. de Lorenzo, M.Manosas, K.Hayashi, J.M.Huguet and F.Ritort. *Improving signal-to-noise resolution in single molecule experiments using molecular constructs with short handles.*Biophysical Journal; 100, 1765-1774 (2011).
- A.Mossa, S. de Lorenzo, J.M.Huguet and F.Ritort. *Measurement of work in single-molecule pulling experiments.* Journal of chemical physics, 130, 234116 (2009).

Appendix A

Improving the temporal resolution

As was explained in Section 4.2, the signals of the PSD are sent to the boards in the electronic tower. The ADCs (Analogical Digital Converter) boards carry out the analogical-digital conversion between the computer and the instrument head. After that the data are sent to the PICs in the main board which work with an acquisition rate of 1kHz. The acquisition rate of 1kHz means a limited temporal resolution. This temporal limitation can produce loss of information such as the detection of intermediate states or details in the folding of the molecules. In order to achieve a high temporal resolution, it is necessary to implement a data acquisition (DAQ) system with a high acquisition rate.

Why is the acquisition rate important in achieving higher resolution? Let us consider an event with a given lifetime τ. The characteristic frequency at which this event can be detected, is inversely proportionate to τ. Using an acquisition system to measure a process with a lifetime τ, it is essential that our bandwidth (B) is sufficiently large to detect that event. For this reason, B must satisfy $1/B < \tau$. Therefore improving the temporal resolution implies developing an acquisition system that can record data at a bandwidth B as large as possible.

In the electronic tower there are two ADC boards, one per trap. These boards have many electronic components. The most significant component is the Analogical Digital converter (ADC) chip which enables the conversion of analog signals into digital signals. In our case the analog data are the signals coming from the PSDs. These signals arrive to the ADC in units of Volts and after being converted into bits, are sent to the host (Fig.A1.A).

Moreover each ADC board contains two connectors (jacks) in stereo configuration that work as an analog output. With these connectors we receive the signals (force and distance) from the PSDs before they have been processed by the ADC. These connectors are only used when we want to obtain analogical data from the instrument (Fig.A1.B).

Each jack connector gives us two different signals: the force and the distance of each trap along the x and y directions. The data acquisition is carried out using a Data Acquisition (DAQ) board (National Instrument PXI-1033). This board works with a maximum sampling rate of 100kHz. The DAQ board is controlled by a program made in Labview. This program enables the control of different parameters of the DAQ board (such as the acquisition rate or the total acquisition time) as well as the collection and recording of data (Fig. A2).

A.0.1 Sampling and reconstruction of analogical signals

A signal is the variation of a quantity by which information is transmitted. Suppose that we are interested in the reconstruction of a signal, h(t). To this end, a DAQ system is used, and the process is called *sampling*. When the sampling process is performed at sufficiently high rate, the DAQ system can capture the fastest fluctuations of the signal which contain useful information about the fast process.

An important parameter in data acquisition is the *sampling rate*. This parameter is the number of samples recorded per second. For a given value of the sampling rate (f_s), there is a time interval (Δ) between consecutive recordings, f_s=1/Δ. According to the *Nyquist theorem*, the Nyquist rate f_{Nyq} is the minimum sampling rate required to avoid *aliasing*, and is equal to twice the value of B:

$$f_{Nyq} = \frac{1}{2\Delta} = 2B \tag{A.1}$$

The meaning of aliasing is illustrated in Fig.A3. Aliasing is an effect produced when data is sampled using an acquisition rate f_s lower than f_{Nyq}(i.e $f_s < 2.B$). When the acquisition rate is low, the reconstruction of the original signal maybe lost under an aliasing signal.

A.0.2 The limitation in the timescales

The temporal resolution in a data acquisition system is limited by the bandwidth of the system, B. In the kinetic analysis of a hopping experiment it is necessary to consider all the characteristic time scales of the system such as the relaxation time of the trapped bead or the relaxation time associated with the biological components of the system (handles and hairpin of DNA)[78].

We must take into account the relaxation time of the bead in the optical trap. As has been shown in [78], the relaxation time of the bead defines the rate limiting step for detecting the fastest conformational events. The trapped bead has a relaxation time that is given by:

$$\tau_b = \frac{\gamma}{\kappa_b + \kappa_h}, \tag{A.2}$$

where γ is the drag coefficient ($\gamma = 6\pi r\eta$), r is the radius of the bead and η is the viscosity of the medium, κ_b is the stiffness of the optical trap and κ_h is the stiffness of the handles. The experimental values of these parameters are $\kappa_b\simeq 0.05pN/nmand\kappa_h\simeq 0.2pN/nm.Thecornerfrequencyofthetrappedbeadistheinverseof\tau_b$ and has a typical value around 10kHz. For this reason, changes in force and distance that have happened faster than the inverse of the corner frequency, cannot be detected by the instrument (B=1kHz).

The limit of the instrumental time is imposed by the acquisition rate of the original setup. The bandwidth of the DAQ system in the original setup is around 1kHz, so the data are collected every $1ms$. However by using the new methodology of data acquisition, it is possible to record events up to 100kHz of bandwidth.

A.0.3 Calibration using the Brownian motion

The calibration of the trap stiffness is usually made by measuring the force acting on a immobilized bead when the trap position is changed. Force measurements in the mT are commonly calibrated using Stokes's law. However, with the new DAQ system it is possible to calibrate the force and the stiffness of the optical trap by means of the thermal Brownian method.

The motion of a Brownian particle in an harmonic potential can be used to measure the stiffness of the optical trap (κ). The Brownian motion corresponds to the random movement of the trapped bead suspended in a liquid with viscosity η at a temperature. This method requires knowledge of the bead diameter.

To calibrate the optical trap using the Brownian motion method we need to do a power spectrum analysis. Measuring the power spectrum is a useful tool which supplies us with valuable information about random signals [79]. In that case the random signals are the fluctuations in position x (relative to the center of the trap) and force for a particle trapped in an harmonic potential, where the relation between them is $f = \kappa_B x$.

The amplitude of the fluctuations in position x and force f in Fourier space are defined by their corresponding power spectrum which are shown as:

$$< \Delta x^2(w) >= \frac{2k_BT}{\gamma(w_c^2 + w^2)} \tag{A.3}$$

$$\langle \Delta f^2(w) \rangle = \frac{2k_BT\gamma w_c^2}{(w_c^2 + w^2)} \tag{A.4}$$

where w_c is the corner frequency of the bead and where γ denotes the drag coefficient. To calibrate the trap using this method we must determine the corner frequency (w_c) of the power spectrum which is expressed as:

$$w_c = \kappa/\gamma \tag{A.5}$$

For ν_c=600Hz ($w_c = 2\pi\nu_c$), we get κ_b=94.2pN.μm

Position and force fluctuations represent measurements of noise and their acquisition depend on the bandwidth of the DAQ system.

With the original acquisition system we can get a maximum bandwidth of 1kHz and the corner frequency of the bead falls in the same frequency range (ν_c=600Hz). Consequently, in order to calibrate the stiffness of the optical trap by means of the power spectrum, we need a DAQ system with a larger bandwidth. [1]

In Fig.A4 we show the results of the power spectrum obtained with the DAQ system at high bandwidth. Data obtained with the DAQ board is analyzed with a program written in MATLAB. In order to avoid unwanted noise it is convenient to average the data. The result of this processing is the smoothing of the spectrum. This process is called Data Windowing.

In the graphs two regions are distinguishable. For frequencies lower than the corner frequency ($w < w_c$),the fluctuations in force are approximately constant.

$$\langle \Delta f^2(w) \rangle \simeq 2k_B T\gamma \tag{A.6}$$

This approximation will be used to calculate the conversion factor between Volts and pN^2/Hz (Unit of Power spectral density).

In fact the DAQ board receives the signals in Volts, so it is necessary to do the conversion of data to force. Both signals are proportional. The conversion factor is given using the following relation:

$$Force(pN) = m.Voltage(V) \tag{A.7}$$

where m is the conversion factor. Using eq.(A.7) and by doing a Lorentzian fit to the experimental data, we get the conversion factor (m = 6.2.10^{-8} pN/V).

---

[1] It is important to distinguish between ν_c and w_c. The power spectrum represents the power spectral density versus frequency in units of Hz (ν). However the corner frequency (w_c)(See Eq.2) has units of rad/s. The relation between them is given by w_c=2 π ν_c.

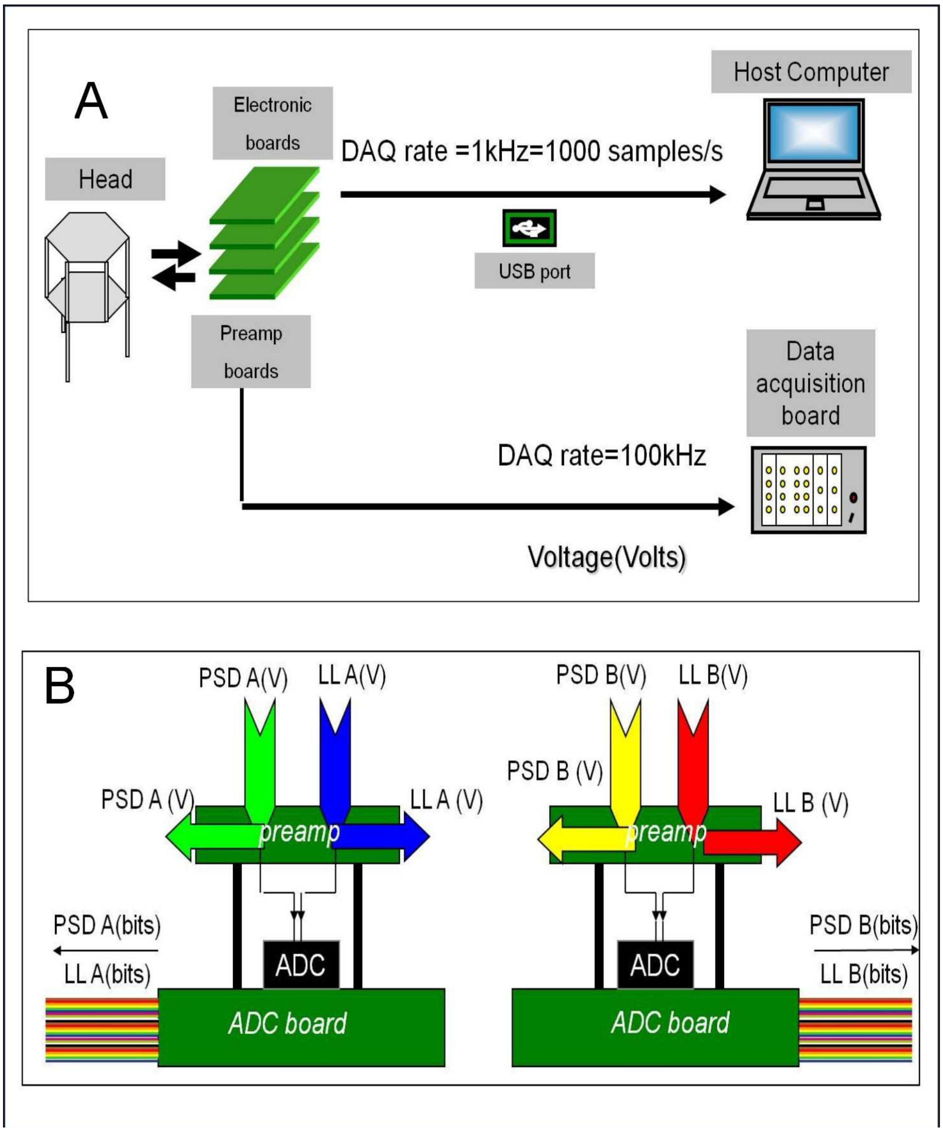

Figure A.1: *A. Sketch of the connections between Electronic boards and: the Host computer and the Data Acquisition board. B. Sketch of the ADC boards. Here we show the path of the signals from the PSDs to the ADC boards. The connections between the ADC board and the DAQ board are made through coaxial cable.*

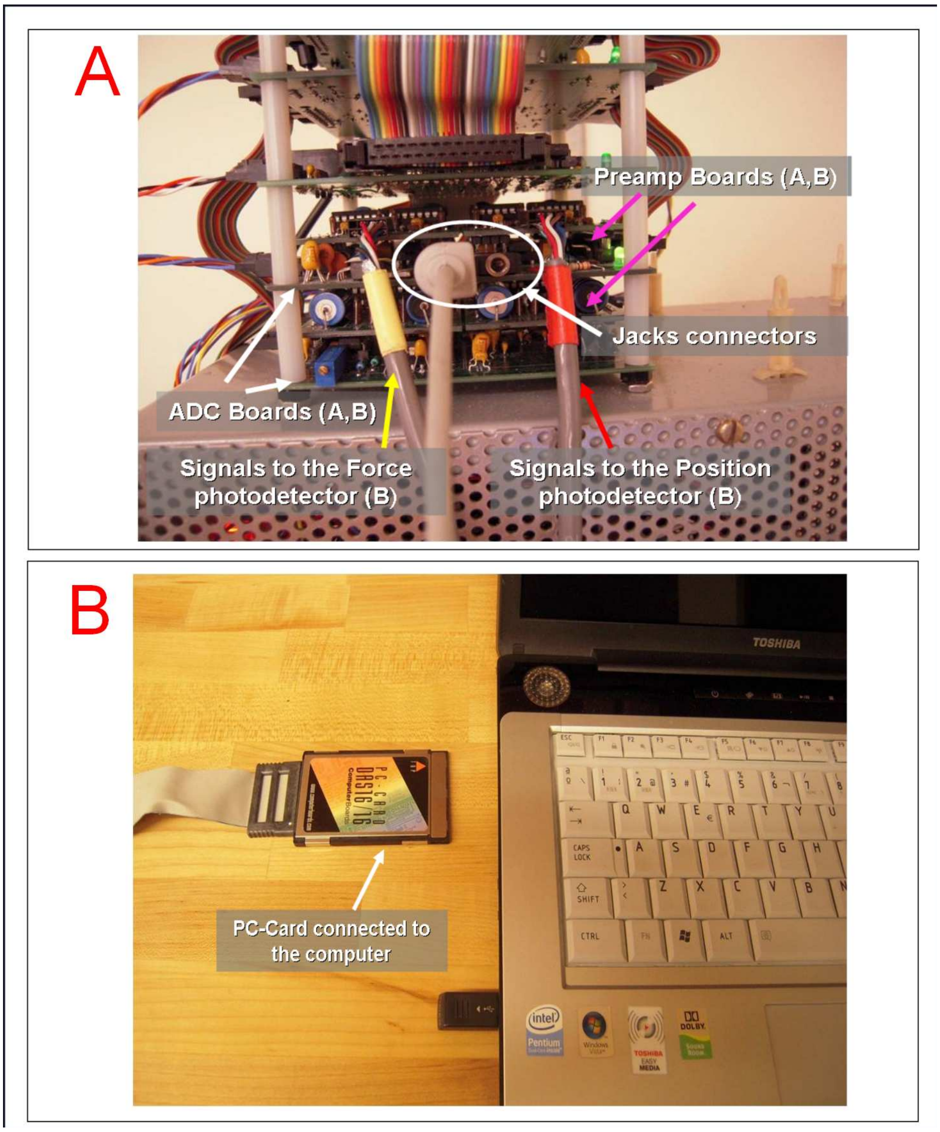

Figure A.2: *Pictures of the setup to measure at high resolution. A. ADC boards and Preamp boards. In the ADC boards are the stereo jacks connectors which work as the analog output. The coaxial wires (only one is shown in the picture) are connected to the DAQ board. B. The connection between the DAQ board and the computer.*

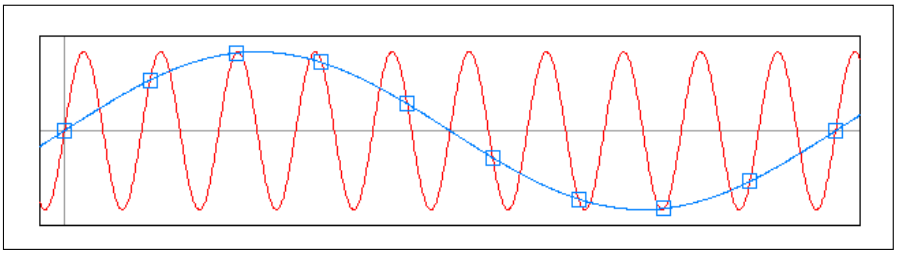

Figure A.3: Aliasing. In this graph it is possible to observe the aliasing phenomenon. The red signal represents the original signal and the blue signal shows the signal recorded by the DAQ device operating at very low sampling rate.

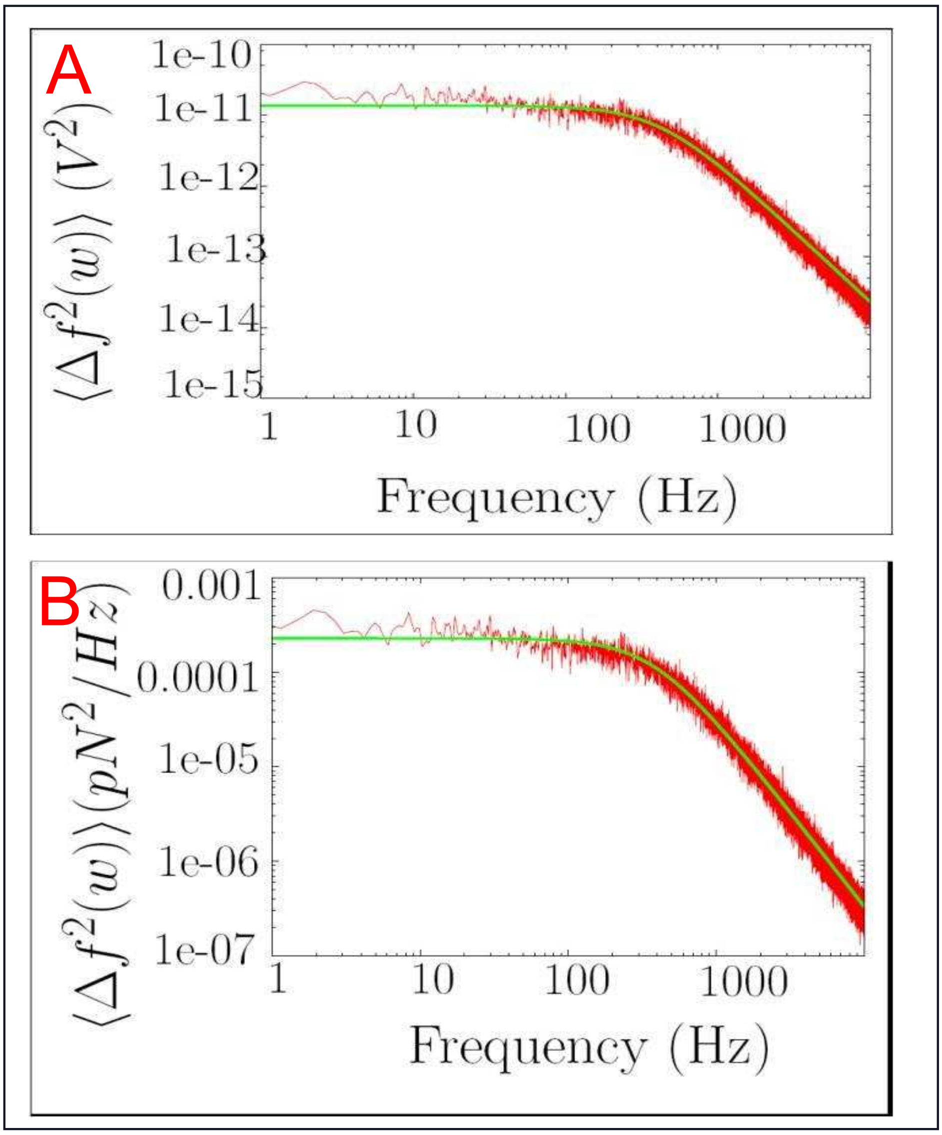

Figure A.4: Power spectral density of the PSD (laser B coordinate y). The signal is received with the DAQ board. Fitting the data to a Lorentzian curve with a ν_c of 365Hz. The data are received at 100 kHz in 5s. Power spectral density in units of Volts. B. Power spectral density in units of force

Appendix B

Switch settings for the heating laser

The current of the heating laser is controlled by a power supply specifically designed for this. The power supply incorporates 4 different switches. Each switch is related with a specific current of the laser and are labeled 1,2,4 and 8. Each switch has the option to be in 1 or 0 (on or off), by increasing the number of switches in the 1 position the laser power will increase. The combination of the 4 switches and their placement in binary form give us 16 sets of options. By starting with (0,0,0,0) where the current of the heating laser is 0mA and going to (1,1,1,1) where the maximum current is (695 mA) we can achieve a temperature increase of 25°C in 14 steps (Fig. B.1).

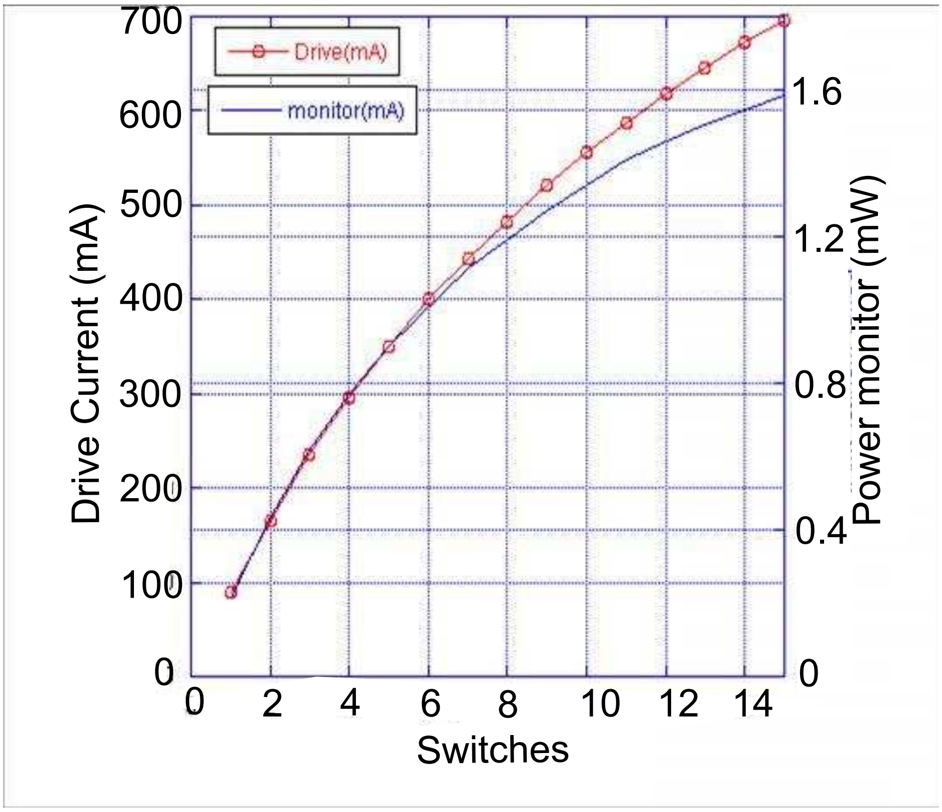

Figure B.1: *Switch position vs. Drive current (mA) and Power-monitor photodiode (mW).*

Appendix C

Power adsorption along the optical path

In this Appendix we will answer the following question of: How much of the 1435nm wavelength light is lost in transmission through the different components along the optical path? The optical absorption rate of the different components found along the optical path has been determined by measuring the transmitted intensity of the laser passing through each component (Fig.C.1). The following table shows the optical absorption rate of each component found in the optical path of the heating laser.

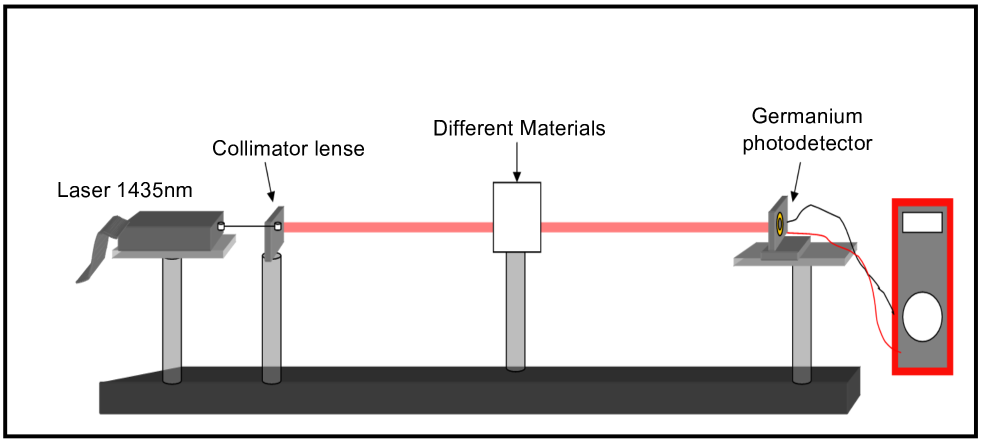

Figure C.1: *Setup of the optical adsorption rate test platform. The absorption rate has been analyzed in the following components: 1 filter of 1435 nm to check that the setup is working, 1 coverslip (Ref: 24mm x 60mm N.2 VWR), 1 polarized beam splitter (Ref:PBS-810-050 CVI-Melles Griot), an empty microchamber, a microchamber full of water and a microchamber full of Cargille fluid. Laser light was sent through the component using a collimator lense (Thorlabs, Ref: 50-1550-FC) and the transmitted light intensity was measured with a germanium photodetector (Thorlabs, Ref: FDG03)*

Sample	**Current (IN) (mA)**	**Current (OUT) (mA)**
Empty	90	12.4
Coverslip	90	11.4 - 11.7
Filter	90	0.6
Polarized beam splitter	90	11.4
chamber without water	90	11.0
chamber with water	90	6.1
chamber with Cargille	90	11.7

The transmission of the light is very good in most of the components (coverslip, polarized beam splitter and chamber without water). An interesting observation is that the optical absorption rate of water is twice that of Cargille fluid (Appendix F). In fact Cargille fluid is a perfect conductor for this wavelength and can work perfectly as an insulator for our experiments.

Appendix D

Measurement of the adsorption coefficient

To measure the adsorption coefficient it has been measured the optical power delivered into the water of the chamber by using Sumitomo laser @ 1435nm and FDG03 photodiode power sensor of germanium with an OD=1.3 neutral-density filter in front of it. In this test has been used a thick microchamber of 1.08 mm of thicknessess. This new microchamber is 10 times deeper than a thin microchamber. The reasons to use this kind of microchamber to measure the absorbance of the water are : partial reflections off glass can interfere constructively or destructively, narrow beam, high power heats water and de-focuses beam (increases ray angles), germanium power meters sensitive to power concentration (focused spots). Next results are obtained:

Current for empty chamber+air = 1.325 mA Current for chamber+Cargille = 1.440 mA Current for chamber+water = 0.0499 mA Water transmission = α = 0.0499 / 1.440 = 0.03465 So the absorbance of water is ln(0.03465) / 0.108 cm = 31.1/cm which agrees well with literature values.

Appendix E

Alignment of focal point vs temperature

The change in the temperature causes a change in optical alignment each time that the temperature is modified due to the dilatation/contraction of the aluminum and brass supports that hold the objective lenses.

How much does the focal point change the temperature?

To answer this question has been developed a *refrigerating/heating assembly* where is possible to know how much the lenses move and if they are closer or farther between them. To build up this assembly we used: (1) Diode laser, (2) insulated box, (3) Refrigerating/heating circulators, (4) photodetector, (5) Electronic boards, (6) host computer and (7) optical breadboard and components. The diode laser (1) used is the same as it is used in the mT. The laser is placed in a large area translation stage (Ref. Thorlabs: AC080-020-B) to improve the stability and to move the laser with more precision, 4 optical post (Ref: PH1/M) and 4 units of Stainless Steel Optical post (Ref:TR20/M). To collimate the laser it has been used the collimating lens (Ref: AC080-020-B; Thorlabs) and the collimated laser beam diameter is about 5mm. Assuming the laser optical fiber has NA=0.125 and the collimating lens has 18.4mm, the collimated laser beam diameter should be around 5mm. The insulated aluminum box is the device where the optical rail of the mT with the objective lenses included will be installed. This box is a prototype of temperature controller cubicle where it is possible to change the temperature by using a water circuit (Fig.E.1). The optical rail prototype is made by a sheet of aluminum. This base simulates the mT optical rail assembly and they have the same thickness. By following the same setup of the mT, one of the objective lenses is placed in a DS40 linear stage which allow to move the objective lenses with a sensitivity of 1 μm. This device is used to move the objective lense in the z-axis direction which means to change the focus of the beam. The DS40 linear stage moves the objective lense by using an Allen wrench which is controlled from a small hole in one of the lateral walls of the box. Both objective lenses are screwed on the pieces of brass that are used in the mT setup. It has been placed a filter ND absorption (NT48-531), in the exit's hole of the temperature controller box to avoid that the detectors were saturated.

The water circuit runs though three of the walls (two of them are parallel to the optical rail axis and the third one is the bottom wall) to generate a homogenous thermal atmo-

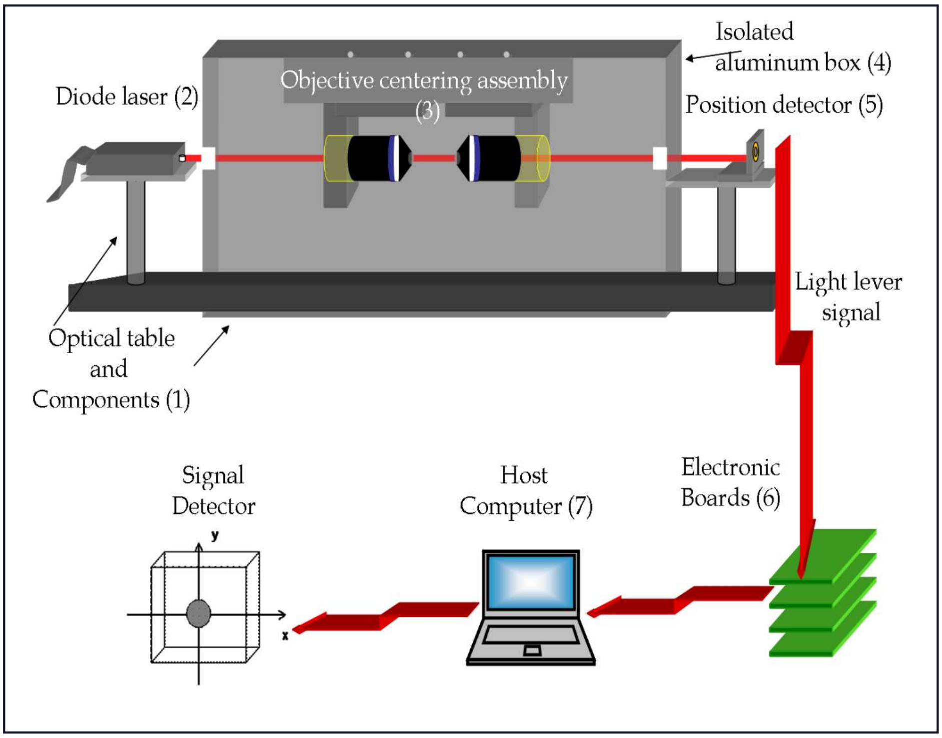

Figure E.1: Setup design of the *refrigerating/heating assembly* used to analyze the relation between the focal point of the objective lenses with temperature.

sphere inside the aluminum box. In the top wall two thermometers are placed to know the temperature inside of the box. In the other two walls are done two holes for the IN/OUT of the laser beam. These holes are around 1cm of diameter and they are placed at the same height as the objectives. To change the temperature of the water it has been used a *refrigerating/heating circulators* (Ref. Polyscience 9100). This kind of water-chiller works between -20°C and 100°C . Fig.E.2 shows the insulated aluminum box and the water circuit.

The photodetector (Fig.E1. element 5) used has been the (Ref: 10-DI photodiode). The holder of the photodetector contains a hybrid beam splitter cube and a bulleyes filter. This component (described in the Methodology chapter) is used to know the power concentration change of the light beam in the focal point. By using this signal, known by IRIS, we are able to know how much the power concentration in the focal point does change when the temperature changes. It also allow us to know in which direction the objectives have been displaced or how far are from the original focal point. The electronic boards (Fig.E1. element 6) receive the analogical signal from the photodiode and transform it in digital signal. The host computer (Fig.E1. element 7) allows us to register the signal of IRIS along the time.

When the setup is ready, the alignment of the laser must be done. The collimated laser enters and exits the objective lenses with the same shape and size. By working at 180mA of current laser, the Power In in the enter of the objective lenses is 63mW, and the Power Out in the exit of the objective lenses is 33mW. After the second objective lens the light passes though the hole of exit of the box reaching to the photo-detector.

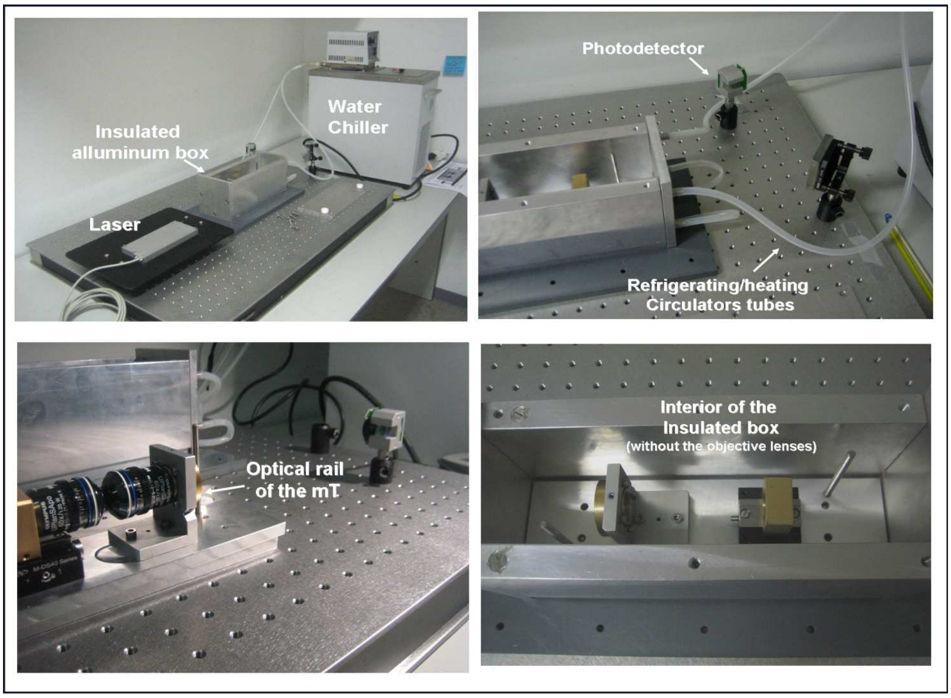

Figure E.2: Pictures of *refrigerating/heating assembly*.

To know the differential thermal expansion rate between the objective lenses and the aluminum base we measured IRIS/SUM vs time at different temperatures. To carry out this analysis we used 4 variables: Temperature (in a range between 5°C and 50°C), Iris/sum Value measured by the photo-detector and registered in the host computer, number of turns necessaries to obtain the IRIS/SUM value of reference at temperature of 25°C, and whether these are clockwise (CW) or counterclockwise (CCW) turns to know if the objective lenses are closer together or farther apart (Figure. E.4). Next steps have been followed:

- Phase1. Base line $T=$ 25°C. Measure the value of IRIS/SUM at 25°C and by taking this as a reference in each experiment.
- Phase2. T_i = 25°C , $T_f=$ final temperature To change the temperature inside the insulated box, the "heater/cooler" circulator water system starts to run. All the experiments start at 25°C and reach the final temperature of interest. By measuring the IRIS/SUM values versus time is possible to observe how this values changes along with temperature.
- Phase3. Value of IRIS/SUM stabilizes at T=final temperature.The temperature takes time to get stabilized, for example from 25°C to 50°C around 30 minutes are needed and from 25°C to 4°C the time goes up to 55 minutes. When the IRIS/Sum value does not change with the time, it is considered such value to be stable.
- Phase4. Moving the screw to obtain the reference IRIS/Sum value: By considering the stable Iris/sum value, the Allen wrench is moved CW or CW until the reference Iris/Sum value is obtained.

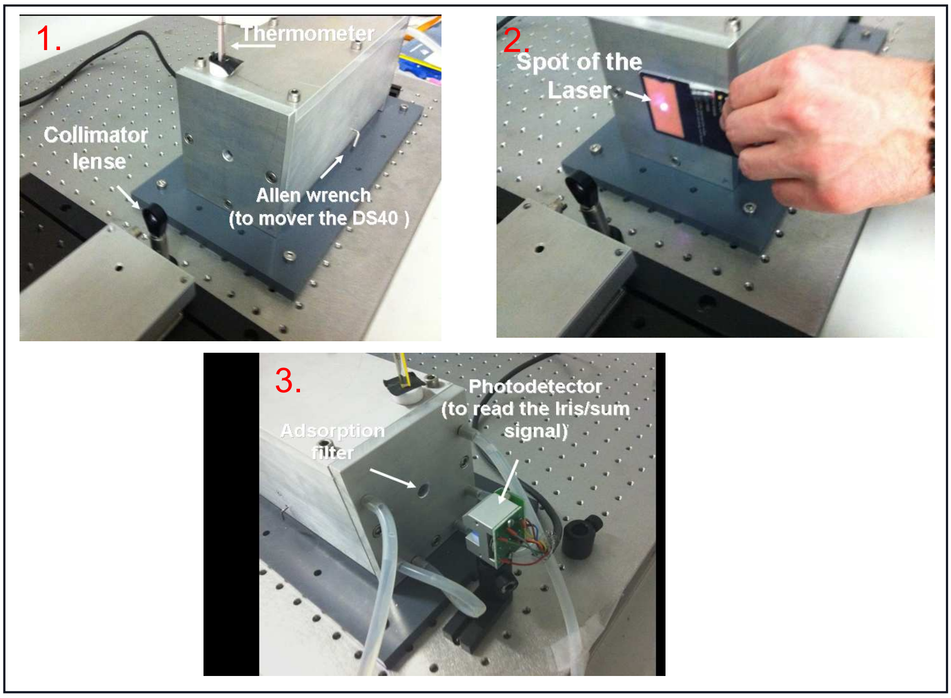

Figure E.3: Methodology used to measure the variation of the Iris/Sum value with temperature.It is important that inside of the insulated box the ambient temperature is constant and stable.For that reason in Step 0 consists the water-chiller is programmed for the water to reach to the desired temperature. After that, the refrigerating/heating circulators start to work and the (cold/hot) water starts to run through the walls of the insulated box. Two thermometers work as temperature sensors. They are placed close to the objective lenses to measure the *ambient* temperature. To read the temperature, half of the thermometer is visibly placed outside of the box. When the temperature is stable inside of the insulated box, we start to measure by following these steps. Step1: The diode laser is turned on and the collimator lens, placed at a specific distance, producing an aligned and narrow laser beam in a specific direction. Step2. The laser enters collimated to the insulated aluminum box and cross the objective lenses. Step3. The laser leaves the insulated box through an adsorption filter. The signal arrives to the photodetector and it is received by the electronic boards and the host computer.

The variation of IRIS/Sum versus temperature is reversible. Fig.E.5 shows the IRIS/Sum values versus temperature and the screw turns versus temperature change where by doing a lineal fitting of the points is possible to conclude that an increase of 1°C requires a compensation of 0.24 CW turns of the focus screw.

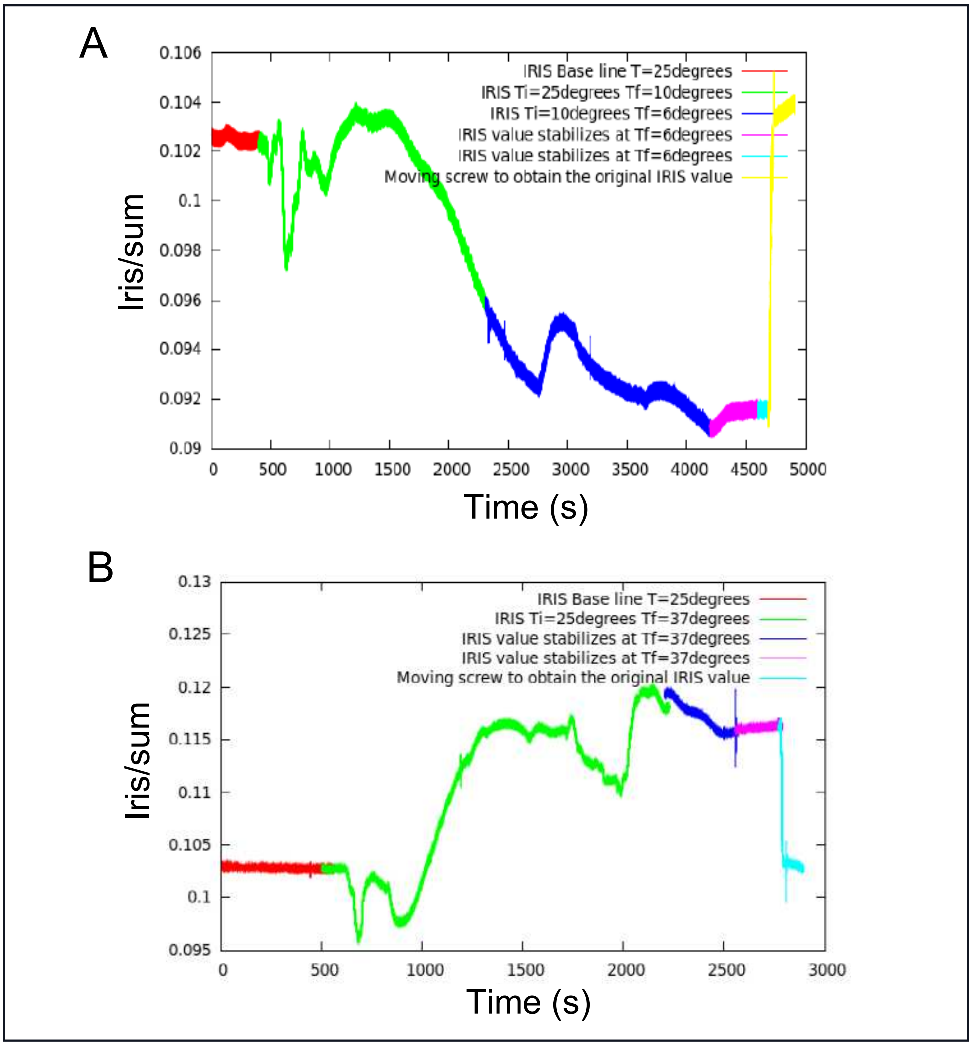

Figure E.4: Signals of the Iris/sum vs time obtained with the *refrigerating/heating assembly* measured at different temperatures. A. T_0=25°C and T_f=6°C. When the setup is stable at 6°C it has been necessary to move almost 2 turns counterclockwise to arrive to the original value of Iris/sum. B. T_0=25°C and T_f=37°C. In that case, when the setup is stable at 25°C it has been necessary to move almost 1 turn and 1/2 clockwise to arrive to the original value of Iris/sum.

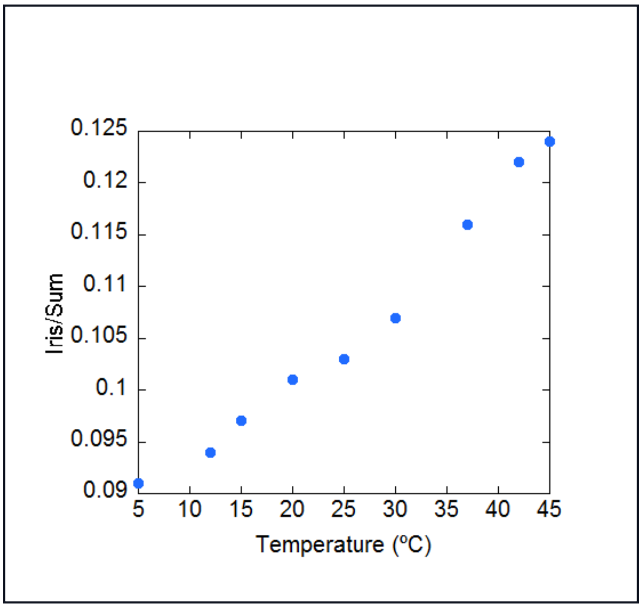

Figure E.5: IRIS/Sum versus T.

Appendix F

Description of the Cargille fluid

The advantages of using Cargille Labs Refractive Index Matching Liquid, Series AAA, n=1.330 are: (1) it evaporates slower than water, (2) evaporation does not cool the chamber so the external ambient temperature probe accurately reports the temperature at the chamber interior, (3) no IR absorption between lens and chamber occurs at 1.4 μm heating laser wavelength and; (4) it has lower thermal conductivity than water (Fig.F.1)

The thermal conductivity (κ) is inversely related to the increase in temperature produced by a heating source. In particular, the increase in temperature upon heating (δT) depends linearly with the power delivered by the heating laser (Q) being inversely proportional to the thermal conductivity of the medium [43], [62], $\delta\mathrm{T} \propto Q/\kappa$. The thermal conductivity of the Cargille fluid is 0.1 W/K to be compared with the thermal conductivity of water (0.6 W/K) and glass (1.4 W/K). The low thermal conductivity of Cargille contributes to minimize heat currents between the fluidics chamber and the objectives, keeping them isolated from potentially harmful heating effects.

Unfortunately Cargille fluid has lower surface tension than water being difficult to keep over long times between the objective lens and the coverglass due to gravity forces. To resolve this problem we used thicker coverglasses for the new fluidics chamber. In this way the distance between coverglasses and objective lenses is reduced and the Cargille fluid stabilized over longer times.

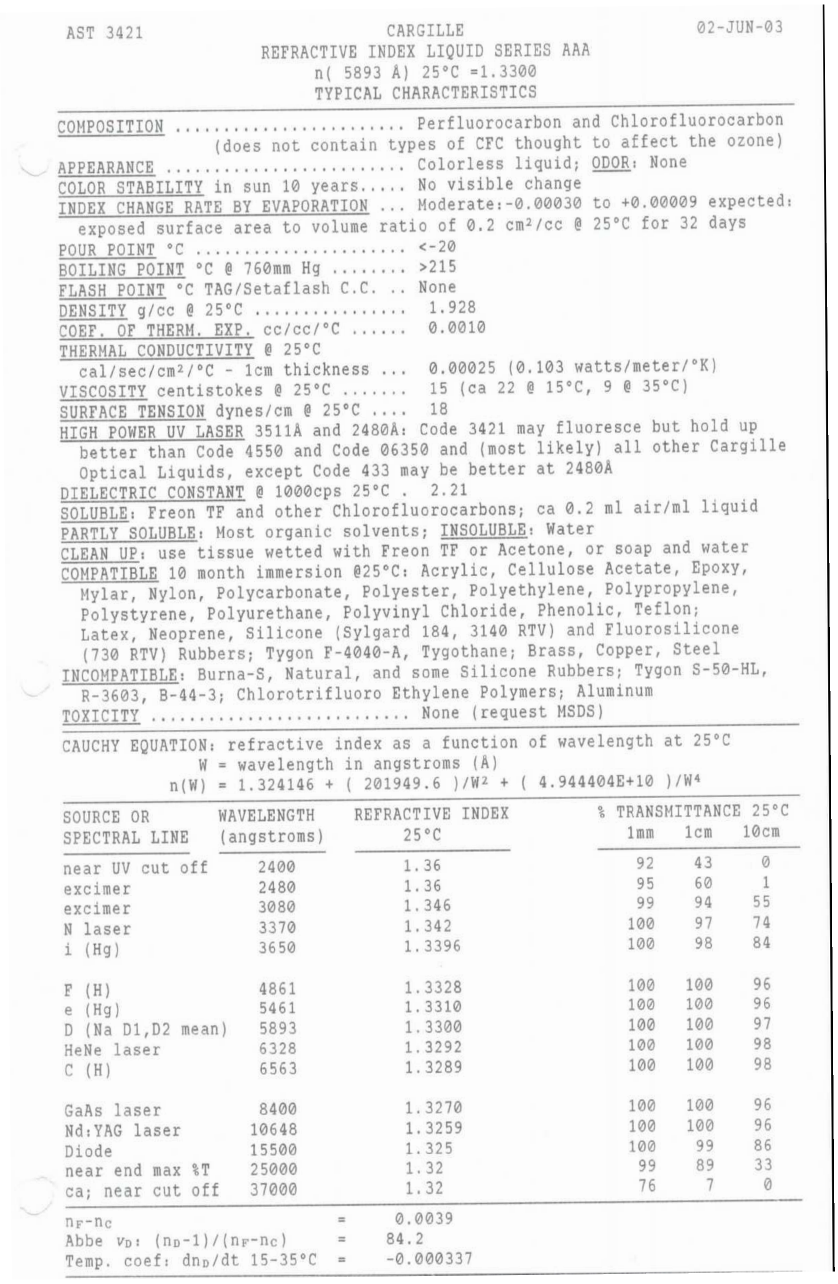

AST 3421 CARGILLE 02-JUN-03

REFRACTIVE INDEX LIQUID SERIES AAA

n(5893 Å) 25°C =1.3300

TYPICAL CHARACTERISTICS

COMPOSITION .... Perfluorocarbon and Chlorofluorocarbon (does not contain types of CFC thought to affect the ozone)

APPEARANCE .... Colorless liquid; ODOR: None

COLOR STABILITY in sun 10 years..... No visible change

INDEX CHANGE RATE BY EVAPORATION ... Moderate: -0.00030 to +0.00009 expected: exposed surface area to volume ratio of 0.2 cm^2/cc @ 25°C for 32 days

POUR POINT °C .... <-20

BOILING POINT °C @ 760mm Hg .... >215

FLASH POINT °C TAG/Setaflash C.C. .. None

DENSITY g/cc @ 25°C 1.928

COEF. OF THERM. EXP. cc/cc/°C 0.0010

THERMAL CONDUCTIVITY @ 25°C cal/sec/cm^2/°C - 1cm thickness ... 0.00025 (0.103 watts/meter/°K)

VISCOSITY centistokes @ 25°C .... 15 (ca 22 @ 15°C, 9 @ 35°C)

SURFACE TENSION dynes/cm @ 25°C 18

HIGH POWER UV LASER 3511Å and 2480Å: Code 3421 may fluoresce but hold up better than Code 4550 and Code 06350 and (most likely) all other Cargille Optical Liquids, except Code 433 may be better at 2480Å

DIELECTRIC CONSTANT @ 1000cps 25°C . 2.21

SOLUBLE: Freon TF and other Chlorofluorocarbons; ca 0.2 ml air/ml liquid

PARTLY SOLUBLE: Most organic solvents; INSOLUBLE: Water

CLEAN UP: use tissue wetted with Freon TF or Acetone, or soap and water

COMPATIBLE 10 month immersion @25°C: Acrylic, Cellulose Acetate, Epoxy, Mylar, Nylon, Polycarbonate, Polyester, Polyethylene, Polypropylene, Polystyrene, Polyurethane, Polyvinyl Chloride, Phenolic, Teflon; Latex, Neoprene, Silicone (Sylgard 184, 3140 RTV) and Fluorosilicone (730 RTV) Rubbers; Tygon F-4040-A, Tygothane; Brass, Copper, Steel

INCOMPATIBLE: Burna-S, Natural, and some Silicone Rubbers; Tygon S-50-HL, R-3603, B-44-3; Chlorotrifluoro Ethylene Polymers; Aluminum

TOXICITY .... None (request MSDS)

CAUCHY EQUATION: refractive index as a function of wavelength at 25°C

W = wavelength in angstroms (Å)

$$n(W) = 1.324146 + (201949.6)/W^2 + (4.944404E+10)/W^4$$

SOURCE OR SPECTRAL LINE	WAVELENGTH (angstroms)	REFRACTIVE INDEX 25°C	% TRANSMITTANCE 25°C 1mm	1cm	10cm
near UV cut off	2400	1.36	92	43	0
excimer	2480	1.36	95	60	1
excimer	3080	1.346	99	94	55
N laser	3370	1.342	100	97	74
i (Hg)	3650	1.3396	100	98	84
F (H)	4861	1.3328	100	100	96
e (Hg)	5461	1.3310	100	100	96
D (Na D1,D2 mean)	5893	1.3300	100	100	97
HeNe laser	6328	1.3292	100	100	98
C (H)	6563	1.3289	100	100	98
GaAs laser	8400	1.3270	100	100	96
Nd:YAG laser	10648	1.3259	100	100	96
Diode	15500	1.325	100	99	86
near end max %T	25000	1.32	99	89	33
ca; near cut off	37000	1.32	76	7	0

n_F-n_C = 0.0039

Abbe ν_D: $(n_D-1)/(n_F-n_C)$ = 84.2

Temp. coef: dn_D/dt 15-35°C = -0.000337

Figure F.1: *Cargille fluid* specification sheets. This document has been provided by *Cargille Laboratories INC*.

Appendix G

Measurement of the heating laser size

To determine the size of the Kohler illumination cylinder, we examine the path of the heating laser beam just prior to entering the coverglass of the microfluidic chamber (Fig.G.1.)

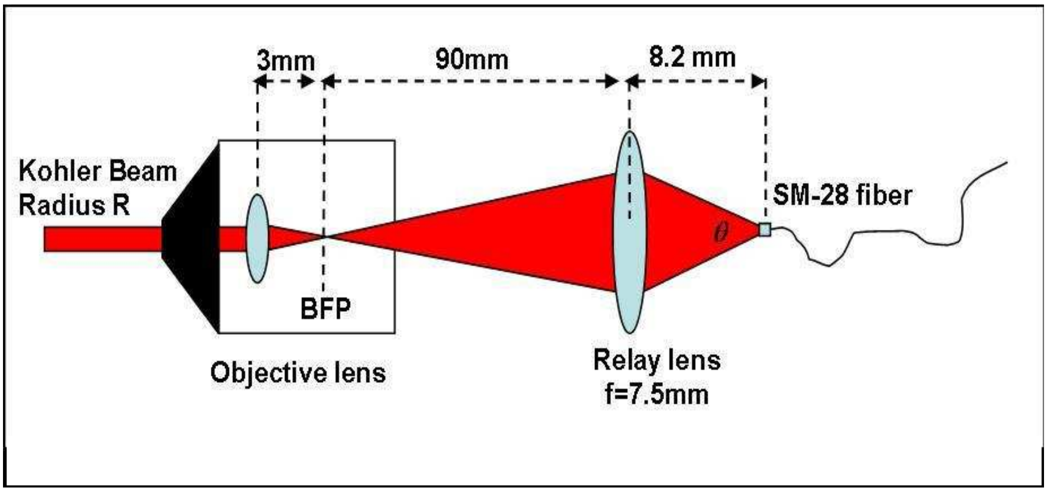

Figure G.1: *Optical path followed by the heating laser. The beam expands from a single-mode optical fiber (SM-28) with a numerical aperture (NA) of 0.14 until it reaches the relay lens. There it is refocused (distance 90 mm) onto the BFP of the first objective lens. Then the narrow beam (NA=0.011) expands in a cone until it hits the 60X objective lens with effective focal length = 3 mm. There it is collimated into a cylinder with radius R=33* μm.

As depicted in Fig.G1, the heating laser light is carried out through an SM-28 optical fiber which has an NA of 0.14. Therefore light exits from the fiber in a cone with vertex angle θ where NA=$sin(\theta/2)$=0.14. That cone expands and travels 8.2 mm until it arrives at the adjustable relay lens (Thorlabs CFC-8X). Then the light is refracted and enters a slightly convergent cone with initial radius of 1 mm. The relay lens (originally sold as an adjustable collimator) is fitted with an extra 0.7 mm spacer ring that allows the conjugate focus to form at 90 mm which is also the distance to the back-focal plane (BFP) of the first objective. The NA of the converging light cone is determined by the next equation,

$NA_{beam} = r_{beam}/f = 0.011$. To get the diameter of the Kohler beam, we must use the focal length of the objective lens which is 3mm and multiply it by NA_{beam}. The radius of the Kohler illumination cylinder is given by $R = 0.011 * 3mm = 33\mu m$. Therefore the diameter of the heating cylinder should be 66μm.

Heat flow model

The total light power absorbed by water inside this Kohler cylinder is called P. By supposing that the heat flows radially outward from the cylinder, it is possible to make an approximation to resolve the heat-flow equations.

By producing a cylindrical light shell of radius r, length L and a thickness dr centered on the laser beam axis, the heat-energy flux conducted through the water will be outward and perpendicular to the laser beam axis.

The heat power transferred across two concentric cylindrical surfaces with radii R and R+dr is:

$$P = -\kappa A \frac{dT}{dr} \tag{G.1}$$

Where P is the light power absorbed by water, κ is the thermal conductivity of water, A is the surface area of the cylinder ($A = 2\pi r L$) and dT is the gradient of temperature between the 2 cylindrical surfaces.

The heat flux density (power per unit area) through the shell surface will equal the total light power absorbed inside the shell divided by the surface area of the shell. By rewriting eq. G1 in function of the heat flux density we obtain eq.G2

$$dT = -(heatfluxdensity/\kappa)dr \tag{G.2}$$

Where the heat flux density is :

$$heatfluxdensity = \frac{Pr}{2\pi R^2 L}(r \leq R) \tag{G.3}$$

$$heatfluxdensity = \frac{P}{2\pi r L}(rR) \tag{G.4}$$

By rearranging eq.G2 and integrating dr can be obtained eq.G4 and eq.G5:

$$T(r) = T(0) - (P/4\pi L\kappa) * (r^2/R^2)(r \leq R) \tag{G.5}$$

$$T(r) = T(R) - (P/2\pi L\kappa) * log(r)(rR) \tag{G.6}$$

Therefore if we know that P=0.0057W (Appendix D), L the distance between the chamber walls 110 μm, the radius of the heating cylinder should be 33μm and $\kappa$for water is 0.58W/meter-Kelvin. Unfortunately integrating dT outside the radius R to a distance r=infinity gives an infinity temperature drop. The usual choice in such problems is to cut off the integration at r=L, the length of the cylinder. Calculating the definite integrals with a cutoff distance L it is possible to say that T(L)=0 (zero degrees above ambient) and:

$$T(R) = 0 + (\frac{P}{2\pi L\kappa} log(L/R) \tag{G.7}$$

(integrating dT outside the light beam)

$$T(0) = 0 + \frac{P}{2\pi L\kappa} log(L/R) + \frac{P}{4\pi L\kappa} \tag{G.8}$$

(plus integrating dT inside) By considering maximum power,T(0)=25°C above the ambient temperature of 25°C. This result is in agreement with the measurements of temperature measured by changes in water viscosity.

A complete temperature profile is shown below (Fig G.2) for a specific power and beam radius. There the vertical axis is degrees rise above ambient temperature.

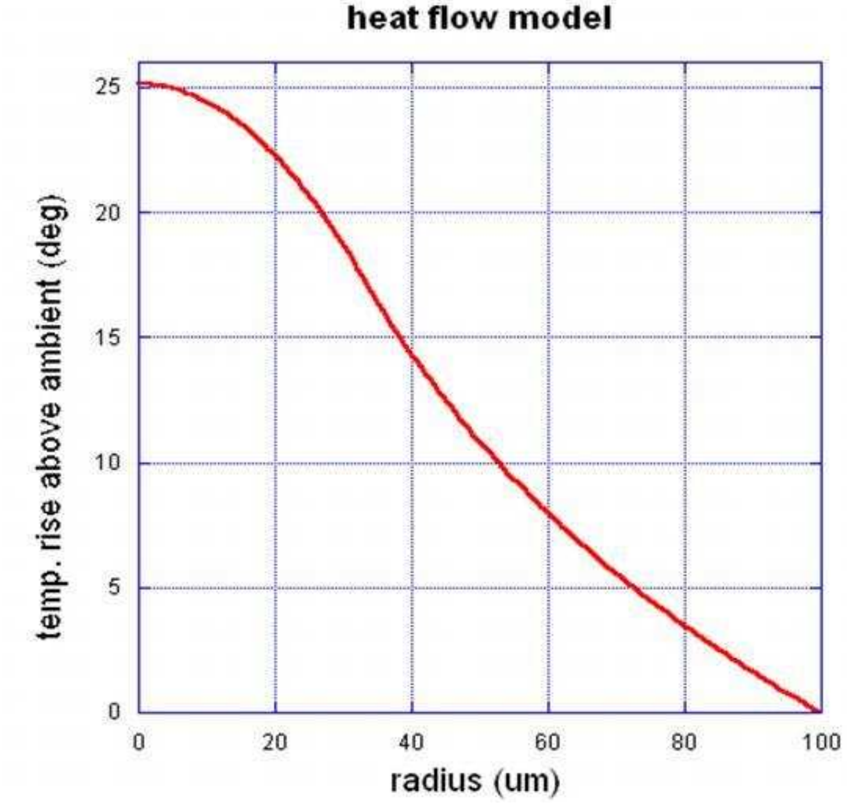

Figure G.2: *Results of heat-flow model for beamRadius = 33μm, absorbedPower = 5.7 mW, cutoffRadius = 90 μm. Vertical axis is temperature rise (degrees) above ambient.*

Appendix H

Experiments to measure the heating profile

Measuring temperature by using Stokes Law:

In order to know the size of the heated region, we measured temperatures in the focal plane at different distances from the center of the heating-laser beam. These temperatures were measured with a trapped bead using the Stokes-drag water viscosity method and also using a thermal-fluctuation method described below. Experiments were carried out in distilled water with polystyrene calibration beads of $3.00 \pm 0.226\mu$m (PolySciences). Bead positions were observed by the CCD camera (Watec 902H3) and the TV monitor (Provideo 901B). We chose 5 positions around the TV screen for our measurements. The position 0 corresponds to the center of the screen and the other 4 around the center as shown in Fig.H1.A.

By knowing that the width of the image on the screen is around 50 μm and the height of the image is around 38 μm, it is possible to deduce the size of the heating spot from the center of the screen. The distance from positions a and b to the center of the screen is around 13.2 μm. And the distances from positions number c and d are around 31 μm from the center of the screen. Figure H1.B plots temperatures (measured by viscous-drag method) versus distance from heating beam center. A linear fit to those data suggests that the heated region extends to a radius around 33 μM.

Measuring temperature by analysis of thermal fluctuations

The measurements of the thermal fluctuations of the trapped bead were performed with an acquisition rate of 100 kHz using a Data Acquisition (DAQ) board (National Instruments PXI-1033). The analysis of the data has been carried out using the power spectrum density method (Fig.H2). This figure shows the power spectrum obtained by the Fourier transform of the thermal fluctuations which has been fitted to a Lorentzian function:

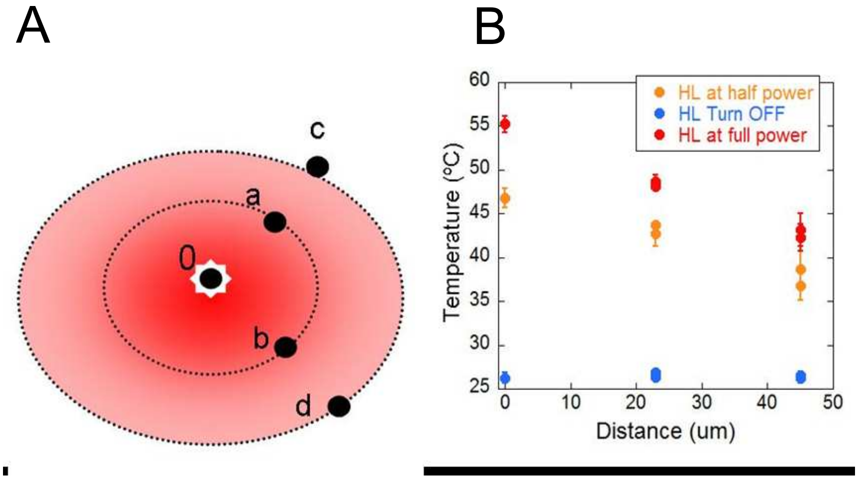

Figure H.1: *A. Schematic drawing of the heating laser around the optical trap (position 0). The points a,b,c and d show the positions where we have analyzed the temperature. B. Analysis of Temperature vs Distance from the center of the screen. Temperatures have been measured at 5 different points on the screen. The distance from positions a and b to the center of the screen is around 13.2 μm. And the distances from positions number c and d are around 31 μm from the center of the screen. The blue points show the results with the heating laser turn off. The orange points show the temperature with the heating laser at half of the power (80 mW). And the red points show the temperature with the heating laser at full power (160mW). The linear fit has been calculated for the three sets of points.*

$$\left\langle f^2(\nu)\right\rangle = S(\nu) = \frac{2\gamma k_B T \nu^2}{(\nu_c^2 + \nu^2)} \tag{H.1}$$

where ν is the frequency in Hz, ν_c is the corner frequency, γ is the drag coefficient and k is the stiffness of the trap. The stiffness at Switch 0 is

$$k = 0.0874 \pm 0.004 pN/nm \tag{H.2}$$

If we assume the stiffness does not depend on the temperature, we can measure the viscosity from the corner frequency:

$$\gamma = \frac{k}{w_c} = \frac{k}{2\pi\nu_c} \tag{H.3}$$

where ν_c is in units of Hz and w_c is in rad/s. To get the temperature, we must measure the viscosity, where the drag coefficient is :

$\gamma = 6\pi\eta r_{eff}$

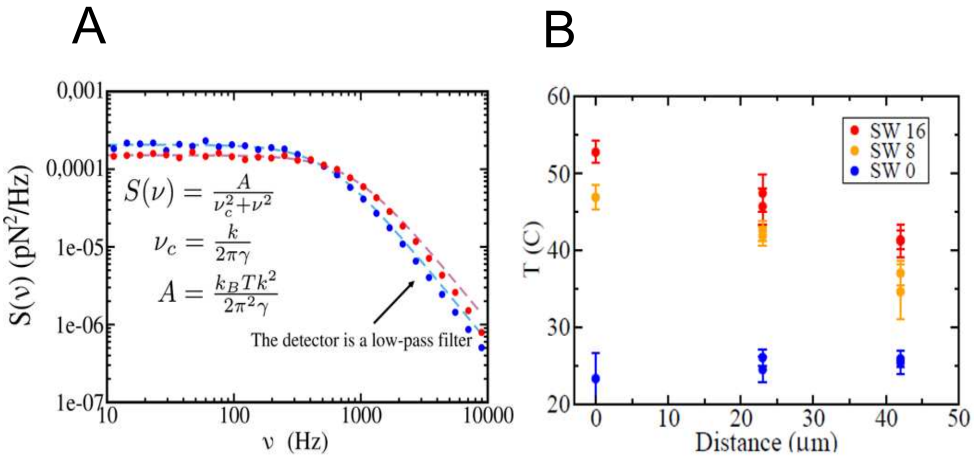

Figure H.2: *A.Noise power density and Lorentzian fits for the previous recording. Red spectrum shows the power spectrum density and the Lorentzian fit calculated by the fluctuations of Brownian motion of a bead in the optical trap. B. Results of Temperature vs Distance from the center of the heating laser spot*

r_{eff} is an effective radius taking into consideration the proximity of the chamber walls. This can be measured at Switch 0, as we know the value of water viscosity at room temperature. Such measurement yields:

$$r_{eff} = 1.77 \pm 0.04 \mu m \tag{H.4}$$

Now we can measure η and thus the temperature using the Vogel formula [**?**]:

$$T(\eta) = (B/(log(\eta) - A)) - C \tag{H.5}$$

where A=-3.72, B=579, C=-137.5, T expressed in Kelvin and η in mPa.s. Now that we have measured the temperature we can check self-consistently our assumption that the stiffness stays constant with temperature. We will use the relation:

$$k = \pi A/(\nu_c k_B T) \tag{H.6}$$

The Fig. H3A. show that our data are compatible with a constant stiffness, i.e. no systematic effect of the temperature or of the position can be detected.

Now the question is: Can we avoid using the Vogel formula?

In principle the temperature could be measured from the variance of the force signal, which should vary linearly with the bath temperature. In terms of the fitting parameters discussed in the last section this would be:

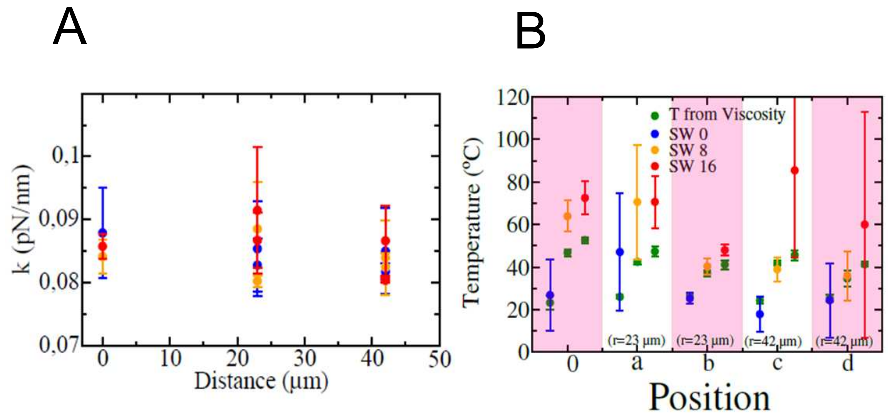

Figure H.3: *A.Stiffness of the trap versus temperature. B. Results of Temperature vs Distance from the center of the heating laser spot and comparison with the Vogel results*

$$T = \pi A/(\nu_c k_B k) \tag{H.7}$$

where the stiffness is again considered constant with temperature and measured at room temperature. This thermometer method does not require a model for how the viscosity depends on temperature. However we now need to measure the variance of the force signal, which is prone both to calibration errors distortions by low frequency noises.

The results of this analysis are shown in Fig.H2B. With the statistics obtained in these measurements, we cannot obtain a reliable temperature measurement from the variance of the force signal. Nevertheless the measured temperature agrees qualitatively with what it was obtained in the last section. It is to be expected that with larger statistics the agreement could be largely improved.

Appendix I

Simulation program for unzipping/rezipping curves

Program Tweez13D is a Brownian dynamics simulation for the mechanical zipping of a DNA hairpin molecule attached to a bead in an optical-trap. It is output is a Force-Distance Curve (FDC) characteristic of the simulated base sequence and temperature. Different pull/relax cycles will exhibit slightly different FDCs due to randomly generated thermal forces. Pull / relax cycles also display force hysteresis which increases with pulling speed. Below is a simplified code example from the main loop:

- repeat
- time:=time+dt ; dt = 1e-7 sec
- getMoleculeTension; bead position, chain length, WLC model
- zipHairpin(tension); move fork position up or down 1 basepair
- sumForcesOnBead; molecule tension + Brownian + optical
- moveBeadInTrap; Langevin Eqn for overdamped particle
- trackLightForce; assumes linear trap, stiffness = kSpring
- moveTraps; to scan through length of molecule
- until scan=finished

The entire program can be downloaded from http://tweezerslab.unipr.it/cgi-bin/mt/software.pl/Se
It was written and compiled with Borland Turbo Pascal 7 and it will run on most 32-bit PC computers with an XP operating system.

Appendix J

Experimental error on thermodynamic potentials

In the main text the homogeneous base-pairing free energy was determined from the integral of the ssDNA FDC:

$$\Delta G_0 = \int \Delta x/bpdf = l_0 \int \left(coth\, \frac{l_k f}{k_B T} \right) - \left(\frac{k_B T}{l_k f} \right) \Big) \left(1 + \frac{f}{K} \right) \tag{J.1}$$

The four parameters entering in this measurement are the mean unzipping force f, the Kuhn length l_k , the contour length l_0 and the stretch modulus K. The errors on these parameters set the uncertainty of our free energy measurements. In Fig. J.1 we show the different contributions to error on the free energy as a function of f, assuming a 5% relative error of the different parameters. These contributions to the error are computed as:

$$d\Delta G_0 = \frac{d\Delta G_0}{d\alpha_i} d\alpha_i \tag{J.2}$$

By using α_i=f,l_k,l_0,K. The error on force measurements is clearly the dominant term, with the other terms having a small influence on the error.

A similar approach can be used to estimate the relevance of the force dependent elastic contribution to the entropy change:

$$\Delta S_{elas} = \int -delta(\Delta x/bp)/\delta T df \tag{J.3}$$

This entropy contribution can be rewritten as:

$$\Delta S_{elas} = \frac{\delta \Delta G_0}{\delta l_k} \frac{\delta l_k / k_B T}{\delta T} + \frac{\delta \Delta G_0}{\delta K} \frac{\delta K}{\delta T} \tag{J.4}$$

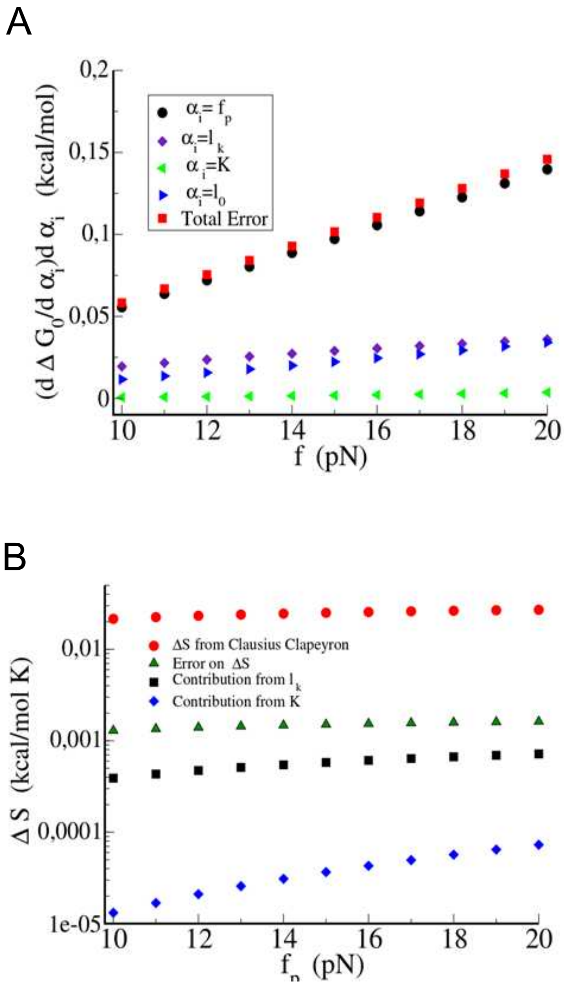

Figure J.1: A.Contributions to error on the free energy as a function of f, B. Contributions on the entropic change as a function of f.

From Fig.4.10 in the main text we can conclude that l_k/k_BT and K do not vary more than 10% over the temperature range we explored so we can estimate $\frac{\delta K}{\delta T} < 2$ pN/K and $\frac{\delta l_k/k_BT}{\delta T}$=0.0003 $(pN.K)_{-1}$. With these estimations we can give upper bounds to the elastic contributions to the entropy and justify the fact we neglected these contributions in the main text. In Fig.J.1 we show the two different contributions to ΔS_{elas} (one for l_k/k_BT and one for K). Clearly the elastic contribution to the entropy change is below the experimental error on the total entropy change measured via the Clausius-Clapeyron equation and can be neglected in our measurements of ΔS_0.

Bibliography

[1] Online etymology dictionary. www.etymonline.com. 2001-2014 by Douglas Harper.

[2] Molecular Biology of the Cell fourth edition, edited by Bruce Alberts (2002); published by Garland Science.

[3] Molecular structure of nucleic acids. Nature, vol 421 (2003)

[4] "Base-stacking and base-pairing contributions into thermal stability of the DNA double helix". P. Yakovchuk, E. Protozanova ,MD. Frank-Kamenetskii .Nucleic Acids Res. 2006 Jan 31;34(2):564-74 (2006)

[5] "Stacking energies in DNA". SG. Delcourt, RD. Blake . J Biol Chem; 266(23):15160-9 (1991)

[6] "A unified view of polymer, dumbbell, and oligonucleotide DNA nearest-neighbor thermodynamics". J.SantaLucia. PNAS, vol. 95 no. 4; 14601465 (1997)

[7] "Sequence dependent rigidity of single stranded DNA". Goddard. N, Bonnet. G, Krichevsky. O and Libchaber.A. Phys. Rev. Lett., 85(11):24002403, (2000).

[8] "Use of Ultraviolet Absorbance-Temperature Profile for Determining the Guanine plus Cytosine Content of DNA". M. Mandel, J. Marmur. Methods in Enzymology 12 (2): 198206(1968)

[9] "Predicting DNA duplex stability from the base sequence". K.J. Breslauer, R.Frank, H.Blocker, L.A. Marky. PNAS 83: 3746-3750 (1986)

[10] "Improved thermodynamic parameters and helix initiation factor to predict stability of DNA duplexes". N.Sugimoto, S.Nakano, M.Yoneyama, K.Honda. Nucleic acid research. Vol:24,No.22, 4501-4505 (1996)

[11] "Optimization of the annealing temperature for DNA amplification in vitro". W.Rychlik, W.J.Spencer, R.E.Rhoads. Nucleic acid research. Vol:18,No.1, 6409-6412 (1990)

[12] "Impacts of magnesium ions on the unzipping of lambda-phage DNA ". C.H.Lee, C.Danilowicz, R.S.Conroy, V.W.Coljee, M.Prentiss.Journal of Physics: Condensed Matter Vol:18 S205-S213 (2006)

[13] "Improved Nearest-Neighbor Parameters for Predicting DNA Duplex Stability". J.SantaLucia, H. T. Allawi, P. A. Seneviratne.Biochemistry 35, 3555-3562(1996)

[14] "Single-molecule derivation of salt dependent base-pair free energies in DNA". JM. Huguet,CV. Bizarro, N.Forns, S.B.Smith, C.Bustamante, F.Ritort.PNAS vol. 107 no. 35, 1543115436 (2010)

[15] "Effects of Sodium Ions on DNA Duplex Oligomers: Improved Predictions of Melting Temperature". R.Owczarzy, Y.You, B.G.Moreira, J.A.Manthey, L.Huang, M.A.Behlke, J.A.Walder. Biochemistry Vol:43, 3537-3554 (2004)

[16] Effect of pH on the Overstretching Transition of Double-Stranded DNA: Evidence of Force-Induced DNA Melting; MC. Williams, JR. Wenner, I Rouzina, VA. Bloomfield. Biophysical Journal Volume 80, Issue 2, Pages 874881 (2001)

[17] "The stability of helical polynucleotides: base contributions". H. Devoe, I.J.Tinoco. Journal of Molecular Biology. Vol:4, 500517 (1962).

[18] "Theory of the melting transition of synthetic polynucleotides: evaluation of the stacking free energy". D.M.Crothers, B.H.Zimm. Journal of Molecular Biology.Vol:9, 19 (1964).

[19] "Thermodynamic characterization of the stability and the melting behavior of a DNA triplex: A spectroscopic and calorimetry study". GE.Plum ,YW. Park, SF. Singleton,PB. Dervan, KJ. Breslauer. PNAS, vol.87, 9436-9440 (1990).

[20] "Base-base mismatches. Thermodynamics of double helix formation for dCA3XA3G+dCT3YT3G". F.Aboul-ela, D.Koh, I Jr. Ticoco, FH.Martin. Nucl.Acids Res. 13 (13): 4811-4824 (1985)

[21] "Differential scanning calorimetry in life science: thermodynamics, stability, molecular recognition and application in drug design". G.Bruylants, J.Wouters, C.Michaux. Current Medicinal Chemistry. Vol:12 : 2011-2020 (2005).

[22] "Statistical and thermodynamic properties of DNA unzipping experiments with optical tweezers". Thesis of Josep Maria Huguet. Universitat de Barcelona (2010)

[23] "Single molecule experiments in biological physics: methods and applications". F.Ritort. J. Phys.: Condens. Matter 18; R531R583 (2006)

[24] "Radiation Pressure on a Free Liquid Surface". A.Ashkin and J.M. Dziedzic. Phys. Rev. Lett. 30, 139 (1973)

[25] "Trapping of atoms by resonance radiation pressure". A.Ashkin. Phys. Rev. Lett. 40, 729 (1978)

[26] "Observation of a single-beam gradient force optical trap for dielectric particles". A. Ashkin, J. M. Dziedzic, J. E. Bjorkholm, S. Chu. Optics Letters, Vol. 11, Issue 5, pp. 288-290 (1986)

[27] "Optical trapping and manipulation of viruses and bacteria". A. Ashkin, JM. Dziedzic. Science 20 Vol. 235 no. 4795 pp. 1517-1520 (1987)

[28] "Optical trapping and manipulation of single cells using infrared laser beams". A. Ashkin, J. M. Dziedzic,T. Yamane. Nature 330, 769 - 771 (1987)

[29] "Grabbing the cat by the tail:manipulating molecules one by one." C. Bustamante, J.C Macosko, and J.L. Wuite. Nature Reviews, 1:130136, 2000.

[30] Direct mechanical measurements of the elasticity of single DNA molecules by using magnetic beads. S.B.Smith, L.Finzi, C.Bustamante. Science, 258 (5085):1122-1126 (1992)

[31] Entropic elasticity of lamda-phage DNA. C.Bustamante, J.F.Marko, E.D.Siggia, S.B.Smith. Science, 265 (5178):1599-1600 (1994)

[32] Bead movement by single kinesin molecules studied with optical tweezers. S.M.Block, L.S.B. Goldstein, B.J.Schnapp. Nature, 348 (348-352) (1990)

[33] Single myosin molecule mechanics: piconewton forces an nanometre steps. J.TFiner, R.M Simmons, J.A Spudich. Nature, 368:113-119 (1994)

[34] DNA molecular handles for single-molecule protein-folding studies by optical tweezers. C.Cecconi, EA.Shank, S.Marqusee, C.Bustamante.Methods Mol Biol. 2011;749:255-71. (2011)

[35] "Overstretching B-DNA: the elastic response of individual double-stranded and single-stranded DNA molecules". S.B.Smith, Y. Cui, and C. Bustamante. Science. 271:795799 (1996)

[36] "Ionic effects on the elasticity of single DNA molecules". C.G.BAUMANN, S.B. SMITH, V.A. Bloomfield, C. Bustamante. Proc. Natl. Acad. Sci. USA; Vol. 94, pp. 61856190 (1997)

[37] Entropy and Heat Capacity of DNA Melting from Temperature Dependence of Single Molecule Stretching; MC. Williams, JR. Wenner, I. Rouzina, VA. Bloomfield. Biophysical Journal Volume 80, Issue 4, Pages 19321939 (2001)

[38] "Direct observation of kinesin stepping by optical trapping interferometry".K. Svoboda, C.F. Schmidt, B.J. Schnapp, S.M. Block. Nature 365, 721 - 727 (1993)

[39] Fluctuation analysis of kinesin movement. K.Svoboda, P.Mitra, S.M. Block. Biophys. J. 68: 69s (1995)

[40] "Elastic properties and secondary structure formation of single-stranded DNA at monovalent and divalent salt conditions". A. Bosco, J. Camunas-Soler, F. Ritort; Nucleic Acids Research, vol: 44 2064-2074 (2014)

[41] "Stochastic thermodynamics, fluctuation theorems and molecular machines". U. Seifert. Reports on progress in physics. vol.75.No.12 (2012)

[42] "The nonequilibrium thermodynamics of small systems".C.Bustamante, J.Liphardt, F.Ritort. Physics Today, vol.58, 43-48 (2005)

[43] "Temperature Control Methods in a Laser Tweezers System". H. Mao, J.R. Arias-Gonzalez, S.B. Smith, I. Jr. Tinoco, C. Bustamante. Biophysical Journal Volume 89, Issue 2, Pages 13081316 (2005)

[44] "Improving signal-to-noise resolution in single molecule experiments using molecular constructs with short handles". N. Forns, S. de Lorenzo, M. Manosas, K. Hayashi, J.M Huguet, F. Ritort. Biophysical Journal, 100; page: 1765-1774 (2011))

[45] "Reversible Unfolding of Single RNA Molecules Using Mechanical Force". J. Liphardt, B. Onoa, SB. Smith, I. Tinoco, Jr., and CJ. Bustamante, Science 292, 733-737 (2001)

[46] "Nanomechanical measurements of the sequence-dependent folding landscapes of single nucleic acid hairpins". M.T. Woodside, W.M. Behnke-Parks, K. Larizadeh, K. Travers, D. Herschlag and S.M. Block. PNAS 103, vol.16 (2006)

[47] "Passive all-optical force clamp for high-resolution laser trapping". W. J. Greenleaf, M. T. Woodside, E. A. Abbondanzieri and S. M. Block. Phys. Rev. Lett. 95(20): 208102, 2005.

[48] "Force unfolding kinetics of RNA using optical tweezers". J.-D. Wen , M. Manosas, P.T.X. Li, S.B.Smith, C.Bustamant F.Ritort, and I. Tinoco, Jr.Phys.Rev.Letter, 78, 2690 (1997)

[49] "Force unfolding kinetics of RNA using optical tweezers. II. Modeling experiments". M. Manosas, J.-D. Wen, P. T. X. Li, S. B. Smith, C. Bustamante, I. Tinoco, Jr., and F. Ritort. Biophys. J.92:3010-3021 (2007).

[50] "Single molecule stochastic resonance". N.Forns, S. de Lorenzo, M.Manosas, K.Hayashi, J.M.Huguet and F.Ritort. Physical Review X, 2 031012 (2012)

[51] "Measurement of work in single-molecule pulling experiments".A.Mossa, S.de Lorenzo, J.M.Huguet and F.Ritort. Journal of chemical physics, 130, 234116 (2009)

[52] "A treatise on electricity and magnetism". J.C. Maxwell VolII Clarendon Press, Oxford (1873)

[53] "Acceleration and trapping of particles by radiation pressure". A. Ashkin. Physical review letters, 24 (4), 156-159 (1970)

[54] "Lights, action: optical tweezers".J.E. Molloy, M.J. Padgett. Cont. Phys., 43:241258, (2002)

[55] "Power spectrum analysis for optical tweezers". K. Berg-Sorensen and H. Flyvbjerg. Rev. Sci. Inst., 75:594612 (2004)

[56] "Optical-Trap Force Transducer That Operates by Direct Measurement of Light Momentum". S.B.Smith, Y.Cui, C.Bustamante. Methods in Enzimology, Vol.361 (2003)

[57] "Counter-propagating dual-trap optical tweezers based on linear momentum conservation". M.Ribezzi-Crivellari, J.M.Huguet and F.Ritort. Review of Scientific Instruments 84, 043104 (2013)

[58] "Light-force sensor and method for measuring axial optical-trap forces from changes in light momentum along an optic axis". C.Bustamante, S.B.Smith. Patent number: US patent 7133132 B2

[59] http://tweezerslab.unipr.it

[60] "Optical trapping of metallic Rayleigh particles". K. Svoboda, S.M Block. Optics Letts. 19: 930-932 (1994)

[61] "Power spectrum analysis for optical tweezers". K. Berg-Sorensen, H. Flyvbjerg. Rev. Sci. Inst., 75:594612, (2004)

[62] "Laser induced heating in Optical traps". E.J.G Peterman, F. Gittes, C.F Schmidt. Biophysical Journal, vol.84, pag: 1308-1316 (2003)

[63] "Real time infrared overtone laser control of temperature in picoliter H2O samples: Nanobathtubs for single molecule microscopy" .E.D.Holmstrom, D.J. Nesbitt. The Journal of Physical chemistry letters, vol1, page:2264-2268 (2010)

[64] "Trapping of DNA by Thermophoretic Depletion and Convection". D. Braun, A. Libchaber. Physical review letters, Vol.89, Number 18 (2002)

[65] "Optical properties of water in the near infrared". K. F. Palmer, D. Williams. Journal of the optical society of America, vol 64, number 8, 1107-1110. (1974)

[66] "Optical constants of water in the 200 nm to 200 μ m wavelength region".G.M Hale, M.R.Querry; Appl.Opt, 12, 555 (1973)

[67] "Tension induces a base-paired overstretched DNA conformation".N. Bosaeus, A.H El-Saqheer, T. Brown, S.B Smith , B. Akerman, C. Bustamante, B. Nordn; PNAS, vol. 109, no.38, 15179-15184 (2012)

[68] "Handbook of Chemistry and Physics". CRC 62 edition. J.F. Swindells, National Bureau Standards (1982)

[69] "Unzipping DNA with optical tweezers: high sequence sensitivity and force flips". U.Bockelmann, P.Thomen ,B.Essevaz-Roulet,V. Viasnoff,F. Heslot .Biophys J. 82(3):1537-53 (2002)

[70] "Viscosity of aqueous sodium chloride solutions from 0C-150C". Ozbek H; Lawrence Berkeley National Laboratories. (2010)

[71] Cargille specification sheet AST3421 Typical Characteristics June 2, 2003 Cargille Laboratories Inc., 55 Commerce Rd. Cedar Grove, NJ. 07009 USA

[72] "Biological applications of optical forces". K. Svoboda, S.M Block SM; Annu. Rev. Biophys. Biomol. Struct. 23.247-85 (1994)

[73] "Low Reynolds number hydrodynamics". Happel and Brenner (1991)

[74] "Stretching DNA". J.F. Marko, E.D. Siggia; Macromolecules 28 (26), pp 87598770 (1995)

[75] "The elasticity of a single supercoiled DNA molecule". T.R. Strick, J.-F. Allemand, D. Bensimon, A. Bensimon, and V. Croquette. Science 271 1835-1837, (1996)

[76] "Non-specific binding of Na+ and Mg_{2+} to RNA determined by force spectroscopy methods".C.V. Bizarro, A. Alemany, F. Ritort; Nucleic Acids Research 40 6922-35 (2012)

[77] "Stretching single stranded DNA, a model polyelectrolyte". M.N Dessinges, B. Maier, Y. Zhang, M. Peliti, D. Bensimon, V. Croquette; Phys. Rev. Lett., 89, 248102 (2002)

[78] Force Unfolding Kinetics of RNA using Optical Tweezers, II. Modeling Experiments. M.Manosas, J.Wen, P.Li, S.B. Smith, C.Bustamante, I.Tinoco and F.Ritort. Biophysical Journal. 92, 3010-3021

[79] Advanced Digital Signal Processing and Noise Reduction. John Wiley and Sons, Ltd. Third Edition.

[80] "Understanding DNA". C. Calladine, H. Drew. (Academic 1992)

[81] "The law of relation between the viscosity of liquids and the temperature". H. Vogel. Phys. Z 1921, 22, 645-646.

[82] "Nonequilibrium Equality for Free Energy Differences". C.Jarzynski. Phys.Rev.Letter, 78, 2690 (1997)

[83] "Verification of the Crooks fluctuation theorem and recovery of RNA folding free energies". D.Collin, F.Ritort, C.Jarzynski, S.B.Smith, I.Tinoco and C.Bustamante. Nature, 437 (2005)